

## NICER X-ray Observations of Eta Carinae During its Most Recent Periastron Passage

DAVID ESPINOZA-GALEAS,<sup>1,2</sup> M. F. CORCORAN,<sup>1,3</sup> K. HAMAGUCHI,<sup>3,4</sup> C. M. P. RUSSELL,<sup>1,5</sup> T. R. GULL,<sup>6,7</sup>  
A. F. J. MOFFAT,<sup>8</sup> N. D. RICHARDSON,<sup>9</sup> G. WEIGELT,<sup>10</sup> D. JOHN HILLIER,<sup>11</sup> AUGUSTO DAMINELLI,<sup>12</sup> IAN R. STEVENS,<sup>13</sup>  
THOMAS MADURA,<sup>14</sup> K. GENDREAU,<sup>15</sup> Z. ARZOUMANIAN,<sup>15</sup> AND FELIPE NAVARETE<sup>16</sup>

<sup>1</sup>*Institute for Astrophysics and Computational Sciences, The Catholic University of America, 620 Michigan Ave., N.E. Washington, DC 20064*

<sup>2</sup>*Departamento de Astronomía y Astrofísica, Facultad de Ciencias Espaciales, Universidad Nacional Autónoma de Honduras, Bulevar Suyapa, Tegucigalpa, M.D.C, Honduras, Centroamérica*

<sup>3</sup>*CRESST and X-ray Astrophysics Laboratory, NASA/Goddard Space Flight Center, Greenbelt, MD 20771*

<sup>4</sup>*Department of Physics, University of Maryland, Baltimore County, 1000 Hilltop Circle, Baltimore, MD 21250, USA.*

<sup>5</sup>*Department of Physics and Astronomy, University of Delaware, Newark, DE 19716, USA*

<sup>6</sup>*Exoplanets & Stellar Astrophysics Laboratory, NASA/Goddard Space Flight Center, Greenbelt, MD 20771, USA*

<sup>7</sup>*Space Telescope Science Institute, 3700 San Martin Drive. Baltimore, MD 21218, USA*

<sup>8</sup>*Département de physique and Centre de Recherche en Astrophysique du Québec (CRAQ), Université de Montréal, C.P. 6128, Succ. Centre-Ville, Montréal, Québec, H3C 3J7, Canada*

<sup>9</sup>*Embry Department of Physics and Astronomy, Embry-Riddle Aeronautical University, 3700 Willow Creek Rd, Prescott, AZ, 86301, US*

<sup>10</sup>*Max-Planck-Institut für Radioastronomie, Auf dem Hügel 69, 53121 Bonn, Germany*

<sup>11</sup>*Department of Physics and Astronomy & Pittsburgh Particle Physics, Astrophysics and Cosmology Center (PITT PACC), University of Pittsburgh, 3941 O'Hara Street, Pittsburgh, PA 15260, USA*

<sup>12</sup>*Universidade de São Paulo, IAG, Rua do Matão 1226, Cidade Universitária São Paulo-SP, 05508-090, Brasil*

<sup>13</sup>*School of Physics & Astronomy, University of Birmingham, Birmingham B15 2TT, UK*

<sup>14</sup>*Department of Physics & Astronomy, San Jose State University, One Washington Square, San Jose, CA 95192, USA*

<sup>15</sup>*X-ray Astrophysics Laboratory, NASA/Goddard Space Flight Center, Greenbelt, MD 20771*

<sup>16</sup>*SOAR Telescope/NSF's NOIRLab*

*Ava Juan Cisternas 1500, 1700000, La Serena, Chile*

(Received MONTH DAY, YEAR; Revised MONTH DAY, YEAR9; Accepted July 8, 2022)

Submitted to ApJ

### ABSTRACT

We report high-precision X-ray monitoring observations in the 0.4–10 keV band of the luminous, long-period colliding-wind binary Eta Carinae up to and through its most recent X-ray minimum/periastron passage in February 2020. Eta Carinae reached its observed maximum X-ray flux on 7 January 2020, at a flux level of  $3.30 \times 10^{-10}$  ergs s<sup>-1</sup> cm<sup>-2</sup>, followed by a rapid plunge to its observed minimum flux,  $0.03 \times 10^{-10}$  ergs s<sup>-1</sup> cm<sup>-2</sup> near 17 February 2020. The NICER observations show an X-ray recovery from minimum of only  $\sim 16$  days, the shortest X-ray minimum observed so far. We provide new constraints of the “deep” and “shallow” minimum intervals. Variations in the characteristic X-ray temperature of the hottest observed X-ray emission indicate that the apex of the wind-wind “bow shock” enters the companion’s wind acceleration zone about 81 days before the start of the X-ray minimum. There is a step-like increase in column density just before the X-ray minimum, probably associated with the presence of dense clumps near the shock apex. During recovery and after, the column density shows a smooth decline, which agrees with previous  $N_H$  measurements made by *Swift* at the same orbital phase, indicating that changes in mass-loss rate are only a few percent over the two cycles. Finally, we use the variations in the X-ray flux of the outer ejecta seen by NICER to derive a kinetic X-ray luminosity of the ejecta of  $\sim 10^{41}$  ergs s<sup>-1</sup> near the time of the “Great Eruption”.

*Keywords:* stars: winds, outflows — stars: massive — stars: individual ( $\eta$  Car) — binaries: general — X-rays: stars

## 1. INTRODUCTION

At a distance of  $\sim 2.3$  kpc (Smith 2006), Eta Carinae ( $\eta$  Car, Davidson 1971; Davidson & Humphreys 1997; Humphreys & Martin 2012) is the nearest star system with a mass  $\gtrsim 100 M_{\odot}$  (Hillier et al. 2001; Madura et al. 2012; Corcoran & Ishibashi 2012). The  $\eta$  Car system is a high-mass non-compact binary system containing an extremely unstable “Luminous Blue Variable” (LBV),  $\eta$  Car-A. In the mid-nineteenth century, this star experienced (and survived) the most energetic stellar mass ejection event ever observed to date, where a mass of  $\gtrsim 45 M_{\odot}$  (Morris et al. 2017) was ejected. This material created the bipolar “Homunculus Nebula” (Gaviola 1950), which today surrounds the star and which is expanding outward at a velocity of  $650 \text{ km s}^{-1}$  (Davidson & Humphreys 1997). Observations of the He I  $1.083\mu\text{m}$  emission line over a period of 50 years reported by Damineli (1996) established, for the first time, a strict periodicity associated with the stellar spectrum, suggesting that the star is a massive binary system with an orbital period of 5.52 years (Damineli et al. 1997). The discovery of periodic X-ray variability (Corcoran et al. 1995; Ishibashi et al. 1999; Corcoran 2005) was critical to identifying the system as a highly eccentric ( $e \approx 0.9$ ) “colliding-wind” binary (Corcoran et al. 1998). The X-ray emission observed from the  $\eta$  Car system is dominated by hot shocked gas produced when the dense, slow ( $V_{\infty} \approx 420 \text{ km s}^{-1}$ , Groh et al. 2012) wind of the LBV primary  $\eta$  Car-A collides with the wind of its companion star,  $\eta$  Car-B. Because the companion star has never been directly detected, X-ray observations remain critical to constraining its stellar wind properties and monitoring changes in mass-loss rate from either star. The temperatures inferred from the X-ray spectrum and the X-ray brightness of the gas shocked in the wind collision suggest that the unseen companion star has a fast ( $V_{\infty} \approx 3000 \text{ km s}^{-1}$ , Pittard & Corcoran 2002) lower-density wind, probably some type of hot massive star (Verner et al. 2005; Mehner et al. 2010). Table 1 summarizes the stellar and orbital parameters of the  $\eta$  Car system.

X-ray spectra provide important observational constraints on temperatures and densities in the hot shocked gas in the wind-wind collision “bow shock”, while the absorption suffered by the X-ray emission provides information on the density distribution of the wind of the LBV primary (since the matter along the line-of sight to the X-ray source is dominated by the wind of the LBV). These quantities change with the distance between the stars (Stevens et al. 1992) as the stars revolve in their extremely eccentric orbit.

Figure 1 shows previous observations (Ishibashi et al. 1999; Corcoran et al. 2001; Pittard & Corcoran 2002; Corcoran 2005; Corcoran et al. 2010, 2017) of the time-variable X-ray emission from the  $\eta$  Car system. These observations have helped to establish the temperatures and densities of the shocked gas in the wind-wind collision region, and analyses of these observations using even-more-sophisticated models (Okazaki et al. 2008; Parkin et al. 2011; Madura et al. 2013) determined the geometry of the shocked winds, temperatures at the colliding-wind region (CWR) and mass-loss rate of the winds from the stars. Even though published 3-D models of the X-ray spectral variability provide a good

**Table 1.**  $\eta$  Car Adopted parameters

Parameter	Value	Reference
Distance (pc)	$2300 \pm 200$	Smith (2006)
Period (X-ray, days)	$2023.40 \pm 0.71$ days	Corcoran et al. (2017)
Eccentricity	0.9	Corcoran et al. (2001)
$T_o$ (Periastron Passage, MJD)	56873.90	Teodoro et al. (2016)
$T_x$ (Deep X-ray Minimum Start, MJD)	50799.42	Corcoran et al. (2017)
Total Luminosity ( $10^6 L_{\odot}$ )	5	Hillier et al. (2001)
Mass, $\eta_A$ ( $M_{\odot}$ )	$> 100$	Hillier et al. (2001)
Mass, $\eta_B$ , ZAMS ( $M_{\odot}$ )	40–50	Mehner et al. (2010)
$V_{\infty, A}$ ( $\text{km s}^{-1}$ )	420	Groh et al. (2012)
$V_{\infty, B}$ ( $\text{km s}^{-1}$ )	3000	Pittard & Corcoran (2002)
$\dot{M}_A$ ( $10^{-5} M_{\odot} \text{ yr}^{-1}$ )	$\approx 85$	Madura et al. (2013)
$\dot{M}_B$ ( $10^{-5} M_{\odot} \text{ yr}^{-1}$ )	$\approx 1.4$	Parkin et al. (2009)
$a$ (AU)	15.9	

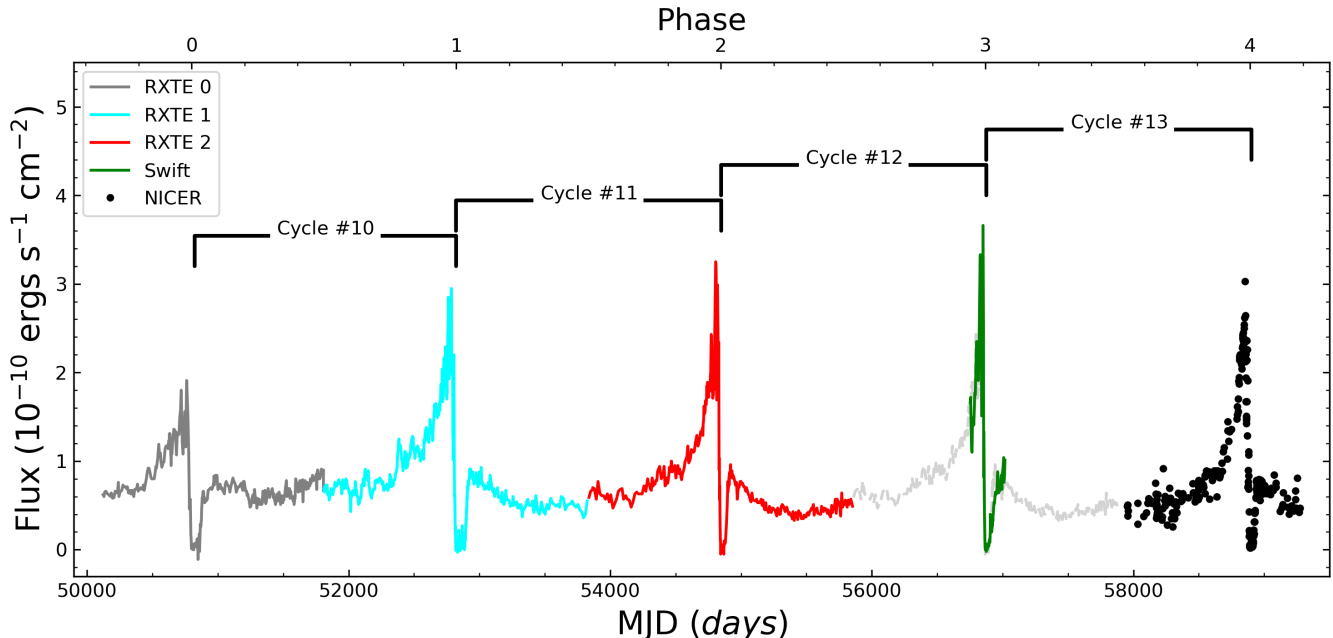


**Figure 1.**  $\eta$  Car’s X-ray lightcurve between 2.0 - 10.0 keV for *RXTE* and *Swift*. For an easy identification the observations are color code and separated in different sets around the X-ray minima. We define  $\phi = 0$  at the X-ray minimum of the first *RXTE* cycle of observations using epoch and period calculated in Corcoran et al. (2017). Corcoran et al. (2017) used the full set of data to find an X-ray periodicity of  $2023.40 \pm 0.71$  days which is very close to the periodicity of 2022.7 days found by Teodoro et al. (2016) for  $\eta$  Car. The brackets show the corresponding cycle numbers using He I and II minima events in Damineli et al. (2008) and Teodoro et al. (2016). The light gray dashed line is a repetition of the last *RXTE* cycle. The plot shows us the variability of the emission in five continuous cycles from 1996 to 2021, including the NICER observations in black.

overall description of the CWR (Parkin et al. 2011; Russell et al. 2016) they do not explain some important details of  $\eta$  Car’s X-ray behavior, such as the “flaring” episodes seen prior to the start of the X-ray minimum (Ishibashi et al. 1999; Moffat & Corcoran 2009), variation in the recovery from the X-ray minimum (Corcoran et al. 2010), or the “Deep”/“Shallow” minimum transition (Hamaguchi et al. 2014).

In this paper we report the first monitoring of the variable X-ray spectrum of  $\eta$  Car with the Neutron Star Interior Composition Explorer (NICER). Here we discuss the observed X-ray spectrum variations from our NICER X-ray observing campaign, and compare them to X-ray variations seen during previous orbital cycles. Throughout the paper, phases are calculated using the X-ray ephemeris (Corcoran et al. 2017) where  $E$  is the cycle count.

$$\text{MJD (X-ray Minimum)} = 50799.4 + 2023.4E \quad (1)$$

The X-ray epoch  $\phi = 0$  in Figure 1 refers to the first *RXTE* deep minimum. Previous works like Damineli et al. (2008) and Teodoro et al. (2016) have used spectral variations of He emission to number the cycles of  $\eta$  Car, starting from the event observed in 1948 by Gaviola (1953). The square brackets in Figure 1 show the corresponding cycle number based on the He minima. The epoch of periastron using He cycles in the Figure is based on variations of the transient He II  $\lambda 4686$  line,  $T_o = 56873.9$  found by Teodoro et al. (2016). This He II epoch corresponds to the starting point of cycle 10, which is 4.3 days later than the X-ray minimum for the 1997 periastron passage.

This paper is organized as follows. We describe the NICER observing program and reduction and analysis of the NICER spectra in Section 2, including a discussion of NICER background estimation. We present the results of the analysis of the net X-ray spectra in Section 4. We discuss the main results of our spectral analysis in Section 5, including a comparison of the NICER spectral properties with similar properties from previous cycles, and in particular compare the flux variations to refine the X-ray period, and examine variations prior to and after the start of the X-ray minimum. We summarize our results in Section 6 and discuss areas of future work.

## 2. OBSERVATIONS

**Table 2.** NICER XTI Characteristics

Property	
Effective area	>2000 cm <sup>2</sup> at 1.5 keV 600 cm <sup>2</sup> at 6 keV
Energy resolution	85 eV at 1 keV 137 eV at 6 keV
Broad Bandpass	0.2 < E < 12.0 keV
Absolute timing precision	< 300 ns
Restricted field of view	30 arcmin <sup>2</sup>
Sensitivity	3 × 10 <sup>-14</sup> ergs s <sup>-1</sup> cm <sup>-2</sup> (0.5-10.0 keV, 5σ in 10 ksec)

**Table 3.**  $\eta$  Car Observation Summary

	# of Obs.	First Obs.	Last Obs.
CHANDRA	31	2000-11-19	2020-01-26
NICER	249	2017-07-21	2021-02-21

### 2.1. Description of the Instrument

The Neutron Star Interior Composition Explorer (NICER, [Gendreau et al. 2012](#); [Arzoumanian et al. 2014](#)) is an X-ray astronomy facility attached to the International Space Station (ISS). NICER is devoted to time-resolved X-ray spectrometry in the 0.2 – 12.0 keV energy band. NICER was launched on 3 June 2017 aboard a Space X Falcon 9 rocket, and deployed at the ISS on 16 June 2017. NICER’s X-ray Timing Instrument (XTI, [Prigozhin et al. 2016](#)) is comprised of a co-aligned array of 52 Focal Plane Modules, each consisting of a matched pair of X-ray “concentrator” (XRC) optics with a silicon drift detector (SDD) to record the energy and time-of-arrival of source X-ray photons. Each XRC optic collects X-rays over a roughly 30 arcmin<sup>2</sup> region of the sky centered on the target of interest in the 0.2 – 12 keV energy band and concentrates them onto an SDD. NICER’s primary mission is to obtain X-ray spectrometry with high time and moderate spectral resolution of cosmic X-ray sources, primarily of X-ray binary pulsars. NICER’s combination of large effective area, restricted field of view and broad bandpass in the thermal X-ray range makes it especially well-suited to observe X-ray variables like long-period colliding-wind binaries (and other sources) in addition to X-ray pulsars. Table 2 lists key technical specifications of NICER’s capabilities.

NICER observed  $\eta$  Car starting on 20 July 2017 (as part of NICER’s “observatory science” program), continuing with guest investigator programs in Cycle 1 (Principle Investigator, M. F. Corcoran) and Cycle 2 (Principal Investigator, D. Espinoza-Galeas). The whole set of NICER observations are listed in the appendix but we present a summary of the observations in Table 3. NICER has provided frequent measure of  $\eta$  Car’s X-ray spectrum, typically twice per month, with appropriately increased sampling near periastron when the variation in the X-ray spectrum occurs on timescales of days. An alternative analysis of some of these spectra was discussed by [Kashi et al. \(2021\)](#).

### 2.2. Data Reduction and Calibration

The NICER spectra for all  $\eta$  Car observations were extracted from the clean, merged photon events file, using data obtained outside of the South Atlantic Anomaly at sun angles > 40° to avoid optical stray-light contamination, using the NICERDAS<sup>1</sup> software package distributed with HEASoft software analysis package (version 6.27.2). We used standard NICER event cleaning criteria<sup>2</sup> to convert the observed event times and pulse-heights to cleaned events with calibrated energies, using data from all 52 active detectors. We used calibration data (effective areas and instrument response functions) from the publicly available NICER calibration data version 20200202.

<sup>1</sup> see <https://heasarc.gsfc.nasa.gov/docs/software/lheasoft/help/nicer.html>

<sup>2</sup> see <https://heasarc.gsfc.nasa.gov/lheasoft/ftools/headas/nimaketime.html> for a description of the standard cleaning criteria

### 2.3. NICER Background Estimation

NICER is subject to a varying charged particle environment in the high-inclination ISS orbit, that traverses regions of trapped charged particles near the South Atlantic Anomaly and the regions near the north and south poles (the “polar horns”). Charged particle background is most noticeable at high energies. At low energies, the NICER background is dominated by optical light contamination at low sun angles and an instrumental “noise peak” of excess events at energies  $< 0.4$  keV. Correction for background is important, especially near X-ray minimum. To minimize background contamination in the NICER spectra, we extracted lightcurves in the  $0.4 - 10$  keV band for all the NICER observations and visually inspected them, defining time regions to exclude short intervals of large rapid increases in count rate produced by the variable charged particle environment. We then extracted X-ray spectra for each observation from the cleaned and screened event files. Residual charged particle background and/or optical light contamination generally affects spectra even after the exclusion of obvious intervals of high background.

Background estimation is still under development, so we used two different background estimator tools provided by the NICER Guest Observer Facility<sup>3</sup>, the `nibackgen3C50` (Remillard et al. 2021) and the `nicer.bkg_estimator` “space-weather” (SW) background estimators. Both estimators use NICER observations of “blank sky” fields (i.e. fields with no obvious sources in the XRC field of view) to estimate background. The `nibackgen3C50` tool compares NICER spectra in various bands in the observed and blank-field observations to construct a background, while the `nicer.bkg_estimator` tool matches sun angle, cut off rigidity and the solar Kp index between the observation and NICER observations of “blank sky” regions to estimate the amount of background due to optical loading and the charged particle environment. Because background estimates continue to be refined, we used both models to gauge the effects of background contamination, but because the SW background estimator showed more dispersion in the  $\chi^2_{red}$  value of the fittings, we adopted the `nibackgen3C50` backgrounds in our analysis.

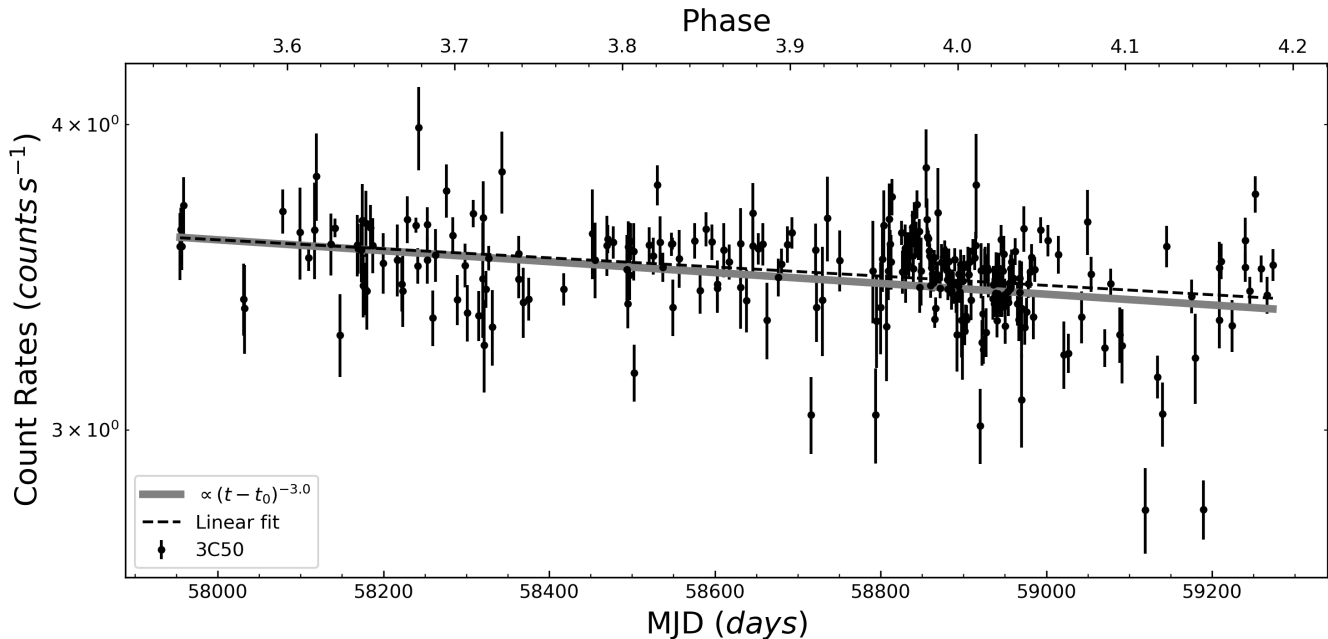


**Figure 2.** Count rates for  $\eta$  Car between  $0.5 - 1.0$  keV observed by NICER after background correction using the `nibackgen3C50` model. Emission in this soft band is produced by the shocked gas in the extended outer debris region around  $\eta$  Car, and is expected to be constant over timescales of months-years. The slight decline of  $\eta$  Car’s soft X-ray emission (dashed black line) shows good agreement with the  $\propto (t - t_0)^{-3}$  power law (gray line), assuming that the ejecta originated near the time of the Great Eruption in 1843 (Kiminki et al. 2016).

<sup>3</sup> See [https://heasarc.gsfc.nasa.gov/docs/nicer/tools/nicer\\_bkg\\_est\\_tools.html](https://heasarc.gsfc.nasa.gov/docs/nicer/tools/nicer_bkg_est_tools.html).

As a check on the background estimation, Figure 2 shows the total count rates for  $\eta$  Car between 0.5 – 1.0 keV, along with the net rates using the backgrounds estimated from the `nibackgen3C50` method. In this range, the X-ray emission is totally dominated by the emission from the “Outer Ejecta” (OE) region surrounding the Homunculus Nebula (Seward et al. 1979; Weis et al. 2004; Hamaguchi et al. 2007a). The emission from the OE region, which extends out to  $\sim 1'$  from  $\eta$  Car, is entirely within the  $1.7'$  radius of the field of view of the NICER SDDs and so present in all NICER observations of  $\eta$  Car. The mean of the total source+background rates in the 0.5 – 1.0 keV is  $\mu_{total} = 3.76 \pm 0.15$  cts  $s^{-1}$ , while the mean of the net count rate using the `nibackgen3C50` method is  $\mu_{net,3c50} = 3.48 \pm 0.14$  cts  $s^{-1}$  and the mean of the net count rate using the space-weather `nicer_bkg_estimator` method is  $\mu_{net,SW} = 3.55 \pm 0.20$  cts  $s^{-1}$ . In this band the 3c50 method appears to have a slightly smaller standard deviation, but similar to that in the total band. Figure 2 shows the net NICER count rates in the 0.5 – 1.0 keV band using the `nibackgen3C50` background estimate. The net NICER count rates in this band seem to show a decline of about 7% over the  $\sim 1000$  days of the NICER monitoring, also visible in the gross rates and the net rates corrected using the “space weather” model. A linear fit to the total (non-background subtracted) count rate data yields a decline of  $\Delta R/\Delta t = 0.150 \pm 0.028$  cts  $ks^{-1} \text{ day}^{-1}$ . We suspected this apparent decline is instrumental, as might be expected from increasing condensations on the FPMs, but examination of NICER observations of the supernova remnant 1E 0102.2-7219, an extended soft source, covering the same timespan as the  $\eta$  Car observations did not find a comparable decline in the soft-band flux. This decrease might be due to expansion of the outer ejecta.  $\eta$  Car’s X-ray emission below 2.0 keV comes from gas heated by the shocked ejecta from the 19th century eruption. The X-ray flux is proportional to the emission measure  $F_X \propto n^2 V$ , where  $n$  is the particle density and  $V$  is the emission volume of hot gas. Assuming a constant mass  $M$  of gas expanding freely at a constant velocity  $v$  then  $F_X \propto (t - t_0)^{-3}$ . Figure 2 shows how the  $(t - t_0)^{-3}$  power-law gives good agreement of the observed  $\eta$  Car’s soft X-ray emission assuming the gas expansion started near the time of the Great Eruption in 1843. The  $(t - t_0)^{-3}$  decline in X-ray flux is observed in the soft X-ray emission (0.3–2.0 keV) of young SN remnants (Immler & Kuntz 2005). Extrapolating this power law to 100 days after the Great Eruption, the initial X-ray luminosity of the shocked ejecta would have been  $L_{x,0} \sim 10^{41}$  ergs  $s^{-1}$ . This would be close to the total luminosity at longer wavelengths derived from the observed brightness of the system at that time ( $L=10^{7.3} L_{\odot}$ , Davidson & Humphreys (1997)). If confirmed, this would be the first estimate of the X-ray luminosity of the Great Eruption.

### 3. MULTI-BAND X-RAY VARIATIONS

#### 3.1. NICER Broad Band X-ray Lightcurves of $\eta$ Car

Measurements of net count rates in the 2.5 – 3.5 keV, 6.5 – 7.5 keV, and 2.0 – 10.0 keV bands are shown in Figure 3. Rates in these three bands are dominated by emission from the hot gas in the colliding-wind shock and background contamination is fairly low. The 2.0 – 10.0 keV band was originally adopted by Ishibashi et al. (1999) in their analysis of the *RXTE* monitoring observations of  $\eta$  Car, and includes nearly all of the observable thermal X-ray emission from the colliding-wind region, while excluding contamination from the OE region which is of lower energy.

The net count rates soon after the start of the NICER observations (on MJD 57954.5, 2017-07-20) show significant artificial scatter from observation to observation because of variations in background which are not accurately accounted for by the background model. To mitigate this variability, we requested that observations obtained after MJD 58306 (2018-07-07) be restricted to avoid times of low geomagnetic rigidity, i.e. when the ISS was not near the South Atlantic Anomaly or the polar horns. This restriction significantly reduced variability from charged particle events, which accounts for the reduced scatter after that time.

The X-ray variability seen by NICER in the 2 – 10 keV band is similar to that seen in other cycles by the *RXTE* Proportional Counter Array and *Swift* X-ray Telescope. As shown in Figure 3, the count rates in all energy bands show a gradual increase from MJD 57954.5 (2017-07-20) to MJD 58610 (2019-05-07). After MJD 58610, the count rate increase accelerates, and short-term brightenings (“flares”, Moffat & Corcoran 2009) occur as the stars approach X-ray minimum near periastron passage. Starting at MJD 58855 (2020-01-06, about  $\phi \sim 0.98$ ) a rapid decline in X-ray count rate began, reaching to the “Deep” X-ray minimum near MJD 58893 (2020-02-14). The emission in this band starts to increase by MJD 58912.5 (2020-03-04), just 19.5 days after the start of the Deep minimum.

The 6.5 – 7.5 keV band is dominated by the high energy thermal emission and includes emission in the Fe K region. This band is not greatly affected by absorption from the wind of the LBV except at phases very close to the X-ray minimum when column densities rise in excess of  $10^{23} \text{ cm}^{-2}$ . The flares in the 6.5 – 7.5 keV band are somewhat smaller in amplitude compared to the 2 – 10 keV band, and there is also evidence that the flares begin sooner in the 6.5 – 7.5 keV than at lower energies. All the flares are present in the 2.5 – 3.5 and 6.5 – 7.5 bands, except for the last flare just

before X-ray minimum. The last flare occurs only in the 6.5 – 7.5 band while the 2.5 – 3.5 count rates stay almost constant. The plunge to the X-ray minimum in the 6.5 – 7.5 keV band seems to occur almost simultaneously with the drop seen in the lower-energy bands, and X-ray minimum flux is reached at MJD 58854 (2020-01-06) in all energy bands. The X-ray count rates in the all bands begin to increase by MJD 58912.5 (2020-03-04), but at different rates. The rate of increase is greatest in the 6.5 – 7.5 keV band, and net rates in this band increase until 58942 (2020-04-03), when it begins to start a slow decline as the stars separate towards apastron. Of the three bands, the rate of increase is slowest in the low energy 2.5 – 3.5 keV band, which shows the importance of extended absorption of the low energy X-rays by the intervening, unshocked wind of  $\eta$  Car-A. This absorption continues for about 200 days after periastron passage.

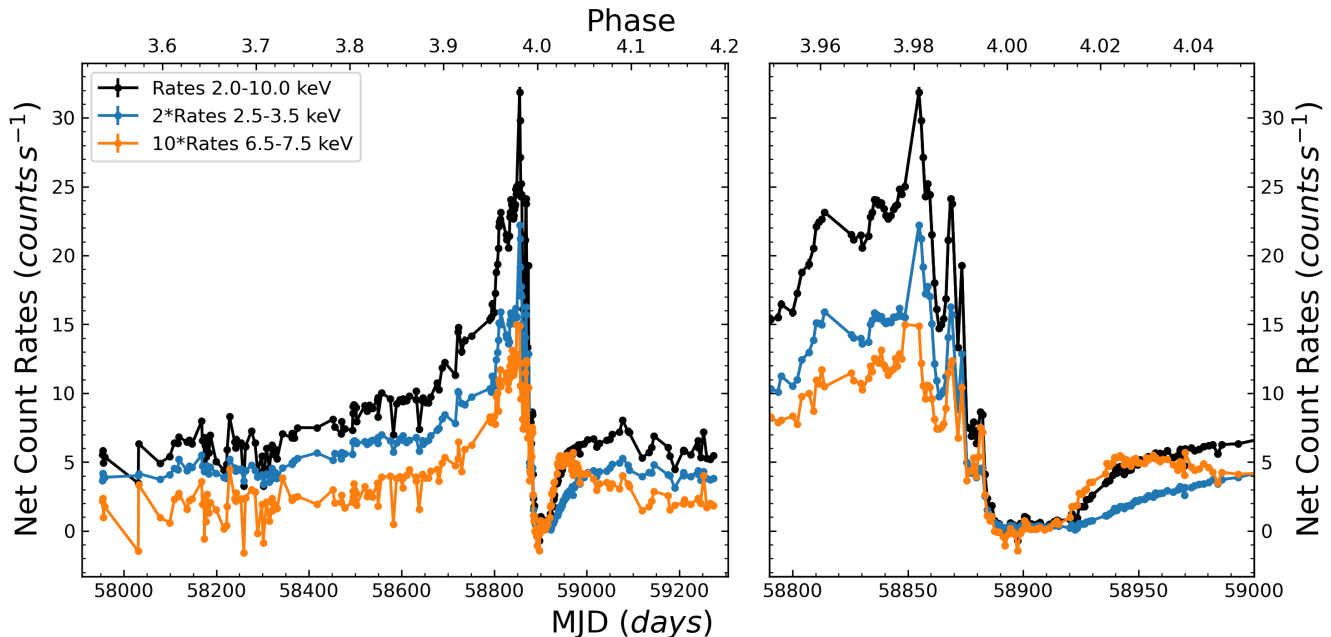


**Figure 3.** NICER net count rates for  $\eta$  Car using the “3c50” background model, in three energy bands. The 2.5 – 3.5 keV and 6.5 – 7.5 keV count rates have been multiplied by 2 $\times$  and 10 $\times$ , respectively, for display purposes.

### 3.2. Hardness Variations

We calculated the hardness ratio  $HR = (H - M)/(H + M)$  where  $H$ , the hard band, is defined as the net count rates between  $6.5 < E < 7.5$  keV, and the medium energy band,  $M$ , the net count rates between  $2.5 < E < 3.5$  keV. We chose these bands because both are dominated by the colliding-wind source with (generally) minimal background contamination, and because the medium band is also sensitive to changes in absorption (as shown in Figure 6) more so than the hard band. This hardness ratio (HR) mainly provides a measure of how the absorption to the X-ray source is changing in time, since changes in shock temperature should be modest, because for most of the orbit the winds collide at terminal velocity.

Figure 4 shows the derived HR from the NICER observations. The HR shows a nearly linear increase with a small positive slope from mid-cycle near apastron to about 20 days before the start of the X-ray minimum, indicating that the hard band flux increases more rapidly compared to the soft band flux, probably due to residual absorption in the soft band. After this, there is a significant increase in the HR occurring in a short phase interval,  $\Delta\phi \approx 0.005$  days, due to a combined increase in emission measure of the shocked wind from the secondary and increased absorption by the wind of  $\eta$  Car-A as the colliding-wind shock starts to move closer to and behind the primary star. This hardness increase happens at the same time the colliding-wind flux is at its observed maximum just before the plunge to minimum. When the plunge to flux minimum starts, the HR also decreases, implying the higher energy emission is decreasing rapidly compared to lower-energy emission. This abrupt decline marks the start of the “deep” X-ray

minimum, when the source spectrum is dominated by soft emission from the “Central Constant Emission” (CCE) component (Hamaguchi et al. 2007b), cosmic background in the NICER field-of-view, and uncertainties in correction of background contamination, and the colliding-wind source emission is depressed.

Shortly thereafter, the HR abruptly increases marking the end of the deep minimum, followed by a short interval during which the HR continues to increase, but at a slower rate. This time corresponds to the “shallow” part of the X-ray minimum. As the colliding-wind source strengthens, the HR abruptly reaches a maximum (which corresponds to the end of the post-minimum flux increase in the 6.5 – 7.5 keV band shown in Figure 3), then declines in a quasi-exponential fashion, as the colliding-wind emission increases but the soft band emission is still heavily absorbed by the wind of  $\eta$  Car-A.

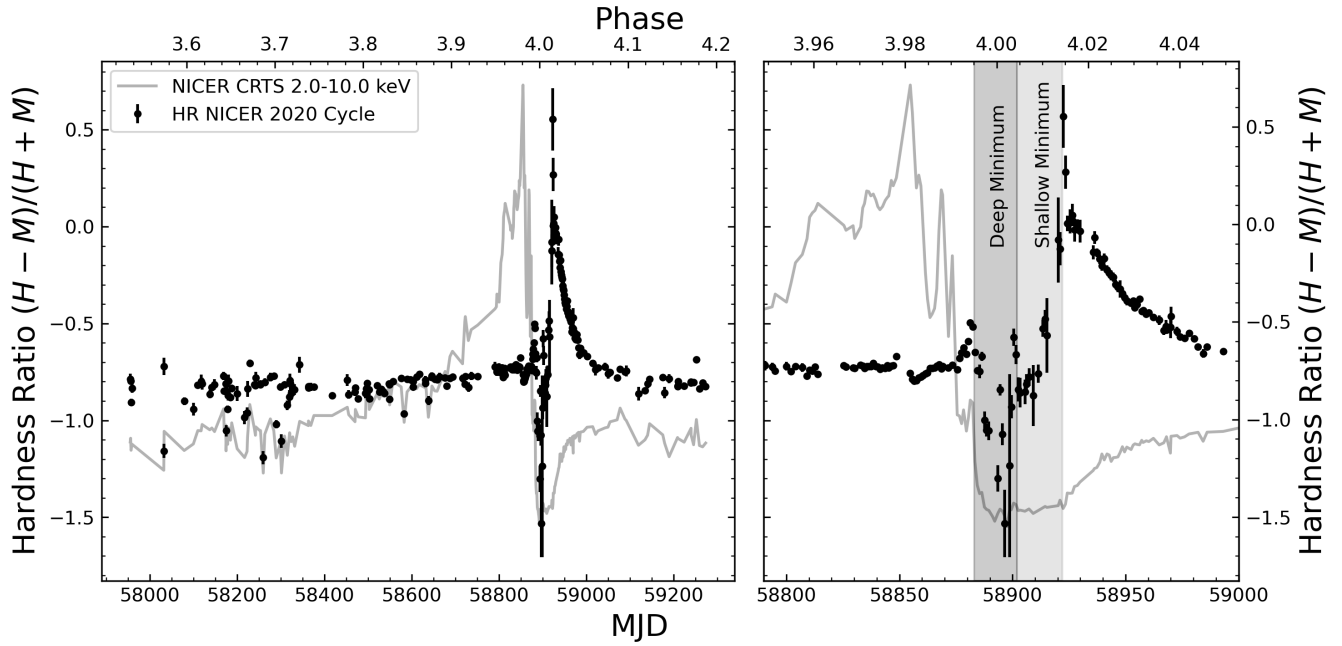


**Figure 4.** Hardness ratio observed by NICER using a medium band between 2.5 - 3.5 keV and a high band between 6.5 - 7.5 keV. The gray regions show the boundaries of the “deep” and “shallow” X-ray minimum. The abrupt decline in hardness ratio marks the start of the deep minimum. The abrupt rise in hardness ratio marks the end of the deep minimum and start of the shallow minimum. The shallow minimum interval ends when the 2-10 keV flux begins to noticeably increase and the observed hardness is a maximum, indicating the re-emergence of highly absorbed emission from the CWR.

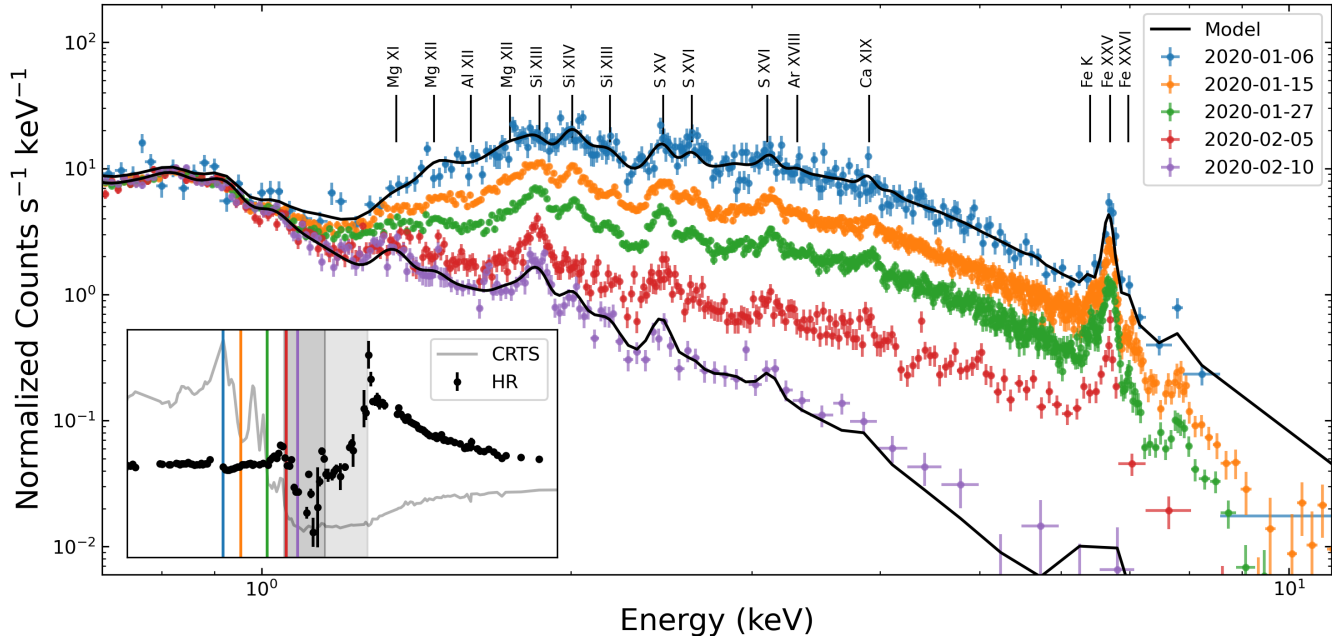
#### 4. THE NICER X-RAY SPECTRUM

Figure 5 shows NICER spectra from the last X-ray maximum (06 January 2020), through the plunge, and until the last X-ray minimum (10 February 2020). Figure 5 is similar to Figure 2 in Kashi et al. (2021) but chosen to avoid flare peaks. Some strong emission lines are marked. The first three spectra show a gradual decline in count rate above 1.5 keV. By 5 February the harder X-ray emission near 1.5 keV is so low that the CCE is clearly observed in the region close to 2.0 keV. The strong Fe XXV feature is still present on 5 February, indicating that hard X-ray emission disappears completely only at minimum.

Figure 6 shows a sample of four NICER spectra of  $\eta$  Car from the X-ray minimum (01 Mar 2020, in blue) up to three months later after the X-ray emission has completely recovered from the X-ray minimum (1 Jun 2020, in blue). Figure 6 can be compared to Figure 4 from Hamaguchi et al. (2007b), which shows a similar montage of the *XMM-Newton* spectra of  $\eta$  Car from 2003. The colliding wind emission cannot be seen below 1.5 keV due to absorption from the Homunculus nebula, which correspond to  $N_H \sim 3 \times 10^{22} \text{ cm}^{-2}$ . The emission below 1.0 keV comes from the OE and does not change significantly. The emission above 4.0 keV recovers faster than the emission between 2.0 - 4.0 keV since it is less affected by absorption, as can be seen by comparing the 19 March and 1 March spectra. By 3 April 2020 ( $\sim 30$  days after the start of the X-ray minimum) the flux above 4 keV has fully recovered, with the colliding wind flux below



4 keV continuing to increase through June 1. Emission above 1.5 keV is mostly thermal emission from the hot shocked wind from the companion star,  $\eta$  Car-B, while below 1.5 keV emission is dominated by the soft thermal emission in the OE. It is worth noting that the Fe XXV line can be detected by NICER even in a short (889 s) observation during the X-ray minimum. In addition to the thermal line emission, NICER clearly shows the Fe-K fluorescence line at 6.4 keV (See Corcoran et al. 1998) blended with the 6.7 keV Fe XXV triplet.



**Figure 5.**  $\eta$  Car spectrum at different phases during the X-ray plunge. The plot has different spectra before the last X-ray minimum showing the decrease of the spectrum. The inset shows HR in black and count rates in gray against time. The color code lines show the time when the spectrum was observed and the gray regions are deep and shallow minimum respectively. We can see the changes above 1.0 keV. The three upper spectra show a evenly distributed decline in count rates at energies  $> 1.0$  keV. By the moment of the fourth observation in red we start to notice a decline in mid range energies between 1.5 - 4.0 keV. The last spectrum it is 7 days before the X-ray minimum, noticed the disappearing of the high energy band above 4.0 keV.

#### 4.1. X-ray Template Model

$\eta$  Car’s spectrum varies over different phases, changing the physical parameters that produce the X-ray emission from the CWR. In order to obtain a better estimation of the temperatures and the column densities from the NICER spectrum we used an  $\eta$  Car spectrum template using all available dispersed spectra from the CHANDRA HETG (Espinoza-Galeas & Corcoran 2020; Espinoza-Galeas 2021, Espinoza-Galeas et al. 2022, in prep, ). We combined the 32 CHANDRA HETG observations in Table 4 to obtain a high-precision dispersed X-ray spectrum with a total exposure of 2 Msec, with a exposure weighted average phase of 0.73. This is the highest precision, highest spectral resolution spectrum of  $\eta$  Car currently available. We fit the combined spectrum with a linear combination of a small number of collisionally-ionized plasma models<sup>4</sup> plus a Gaussian line to model the fluorescence Fe K emission line, plus absorption (Wilms et al. 2000). The NICER spectra are not sensitive to the broadening of the emission lines, but using the CHANDRA combined spectrum it was clear that a velocity-broadened model was necessary. We found that two velocity-broadened non-solar abundance thermal components were sufficient to describe the combined HETG spectrum. We used the CHANDRA combined spectrum as a template model to fit each NICER spectrum to derive X-ray spectral parameters. We fixed the abundances and line broadening to the CHANDRA values when fitting the NICER spectra.

<sup>4</sup> <http://atomdb.org/>

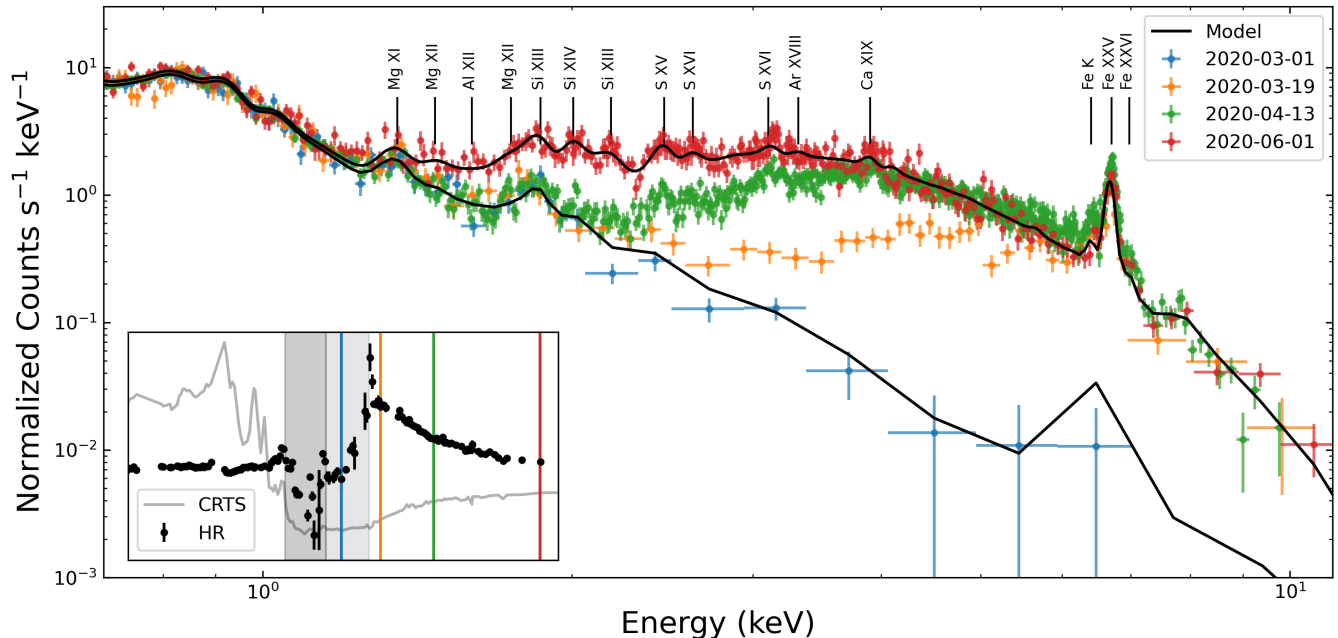


**Figure 6.**  $\eta$  Car spectrum at different phases after the X-ray minimum. The plot has different spectra after the last X-ray minimum showing the recovery of the spectrum. As in Figure 5, here we can follow the changes above 1.0 keV during the recovery, and inset with the same color code as the spectra shows HR and count rates against time. The blue spectrum is in the shallow minimum and does not show emission above 4.0 keV. By the time  $\eta$  Car’s X-ray emission is out of the shallow minimum the high X-ray emission above 4.0 keV is recovered but the mid range energies are highly affected by column density (See 11) which here is reflected in the HR on the inset plot. In the last two spectra (green and red), we can see how the mid range X-ray emission continue recovering slowly after months of the X-ray minimum, but the emission  $> 4.0$  keV was completely recovered since the exit of the shallow minimum.

To model the NICER spectra, we also added to the HETG model a third non-variable thermal component to account for non-variable soft emission below 1.5 keV from the shocked gas in the OE (which is not strongly visible in the HETG spectrum). The initial spectral model parameters are given in Table 5. We then fit all the net NICER spectra, allowing temperatures, column densities and emission measures (normalization) of the two colliding-wind components to vary, with other components and the OE emission component held fixed.

A complete detailed analysis of the combined HETG CHANDRA spectrum is in Espinoza-Galeas (2021). To compare NICER temperatures and column densities we also present preliminary results of temperatures and column densities using the individual HETG CHANDRA spectra (Espinoza-Galeas et al. 2022, in prep).

#### 4.2. Flux Variations

Figure 7 shows the NICER flux between 2.0 – 10.0 keV of all the NICER observations using the `nibackgen3C50` estimator to correct for background, although this model overestimates background for a small number of observations under conditions of high background. The bottom panel shows the reduced  $\chi^2$  value for all the fits, which is generally acceptable except close to X-ray minimum when uncertainties in background subtraction play a significant role in defining the net spectrum. The inset highlights the variations near the X-ray minimum.

Figure 8 shows the flux between 2.0 – 10.0 keV in  $10^{-10}$  ergs  $s^{-1}$   $cm^{-2}$  compared with *RXTE* and *Swift* fluxes in the same band (taken from Corcoran et al. 2017). The three telescopes have instrumental differences and different fields of view that can cause differences in the flux in the same range due to the varying amount of cosmic and instrumental background contamination and other factors. We calibrated the data from NICER with the *RXTE* and *Swift* data by subtracting a small amount of flux from each flux measure to match the flux of the X-ray deep minimum in all the cycles. During the deep minimum the net flux is close to the cosmic X-ray background and flux differences are minimal then.

**Table 4.** HETG CHANDRA observations

obsid	expt	Date	MJD	Phase
632	89545.68	2000-11-19T02:47:43	51867.65	0.527
3749	91280.92	2002-10-16T08:09:53	52563.89	0.871
3745	94533.00	2003-05-02T11:57:20	52762.07	0.969
3748	97249.20	2003-06-16T05:36:31	52806.82	0.991
7445	25393.24	2008-10-15T20:18:41	54755.01	1.954
10787	68904.23	2008-10-21T23:11:26	54761.38	1.957
10831	17589.25	2008-12-08T12:31:41	54808.63	1.980
8930	29646.37	2008-12-10T01:49:02	54810.26	1.981
10827	27365.77	2008-12-12T17:34:07	54812.90	1.983
10895	15257.55	2009-03-16T17:18:12	54906.82	2.029
10894	21986.45	2009-03-17T21:26:40	54908.04	2.030
9945	31275.61	2009-04-21T06:46:35	54942.48	2.047
10905	26298.47	2009-04-26T13:56:49	54947.75	2.049
9946	56628.15	2009-09-06T20:45:21	55081.21	2.116
11992	18428.78	2009-12-21T12:52:08	55186.66	2.167
11017	17454.93	2009-12-22T09:47:25	55187.52	2.168
12064	17703.14	2009-12-23T03:48:06	55188.28	2.168
12065	18625.89	2009-12-23T23:44:42	55189.11	2.168
11993	43826.40	2010-11-14T13:33:42	55514.84	2.329
11994	39364.24	2010-11-21T07:26:40	55521.56	2.333
12358	102189.1	2011-10-20T11:19:40	55855.10	2.497
13670	31173.59	2012-10-19T16:25:08	56219.88	2.678
15569	68162.57	2012-10-20T17:29:41	56221.15	2.678
21177	29027.65	2019-05-16T02:58:19	58619.31	3.863
22218	15446.14	2019-05-17T00:32:15	58620.12	3.864
22219	33862.69	2019-05-18T17:35:26	58621.94	3.864
21178	29024.17	2019-07-01T17:56:35	58665.93	3.886
22272	27089.92	2019-07-02T10:13:04	58666.60	3.887
22273	15489.07	2019-07-04T10:01:32	58668.52	3.887
21179	57150.21	2019-08-27T05:54:31	58721.71	3.914
21180	24249.47	2019-10-08T13:56:11	58764.74	3.937
22310	19570.27	2020-01-06T01:58:12	58854.21	3.981
23117	19570.34	2020-01-06T17:13:59	58854.84	3.981
23119	19567.59	2020-01-11T06:06:16	58859.38	3.983
22311	34169.62	2020-01-13T11:07:07	58861.68	3.984
23126	34168.16	2020-01-14T10:03:59	58862.63	3.985
22846	29302.70	2020-01-16T02:34:15	58864.29	3.986
22847	14703.70	2020-01-26T16:22:24	58874.78	3.991
23131	33195.76	2020-01-27T16:42:56	58875.90	3.991

X-ray flux from a colliding-wind shock in an eccentric binary should vary inversely with the separation  $D$  of the stars (Usov 1992; Stevens et al. 1992) if the shock cools adiabatically. The smooth dashed curve in Figure 8 shows a  $1/D$  variation using the orbital elements in Table 1. For most of the orbit, the NICER 2 – 10 keV X-ray flux agrees with the  $1/D$  curve, but starts to deviate from it 10 days before the X-ray minimum is reached. Prior to X-ray minimum, the *RXTE* fluxes lie on the  $1/D$  curve which fits the NICER data, though the agreement is better about 80 days after X-ray minimum.

Once reaching maximum flux, the NICER lightcurve shows the same plunge into the X-ray minimum as seen in the earlier orbital cycles, as shown in the inset in the upper panel in Figure 8. The X-ray minimum is caused by a combination of eclipse and the disruption of the shock around  $\eta$  Car B by the wind of  $\eta$  Car A, as discussed by Hamaguchi et al. (2014). According to Eq. 1, the deep X-ray minimum should have been reached around 14 February 2020. NICER observed the deep minimum around 13 February 2020 as we reported in Corcoran et al. (2020).

Based on the behavior shown in previous cycles, the end of the X-ray minimum was expected no earlier than the end of March. But the NICER data show a clear increase in flux between 0.5 - 9.0 keV starting approximately on 15 March 2020 (MJD 58923.0, Espinoza-Galeas et al. 2020). This was the earliest recovery of  $\eta$  Car’s X-ray emission yet

**Table 5.** Initial Spectrum Model

Parameter	Cooler Comp	Hotter Comp	Outer Ejecta Comp
NH ( $10^{22}$ cm $^{-2}$ )	3.00	10.00	0.60
kT (keV)	1.26	4.43	0.25
Redshift	0.00	0.00	0.00
Broadening (km s $^{-1}$ )	598.00	888.88	900.00
He	1.00	fixed	fixed
C	1.00	fixed	fixed
N	20.00	fixed	fixed
O	1.00	fixed	fixed
Ne	1.00	fixed	fixed
Mg	0.59	fixed	fixed
Al	0.47	fixed	fixed
Si	0.41	fixed	fixed
S	0.46	fixed	fixed
Ar	0.66	fixed	fixed
Ca	0.88	fixed	fixed
Fe	0.51	fixed	fixed
Ni	1.00	fixed	fixed

NOTE—Elemental abundances are relative to solar values, using [Anders & Grevesse \(1989\)](#). The model also includes a variable gaussian iron K line near 6.4 keV.

observed. The flux increase from minimum in the 2 – 10 keV band ended by MJD 58950 (2020-04-11). The analogous analysis in [Kashi et al. \(2021\)](#) shows similar results, confirming our announcement in [Espinoza-Galeas et al. \(2020\)](#).

#### 4.3. The X-ray Period

We re-determined the X-ray period including the NICER data using a simple implementation of a phase-dispersion minimization technique ([Stellingwerf 1978](#)). We phase-folded the four X-ray flux curves from *RXTE*, *Swift* ([Corcoran et al. 2017](#)), and NICER using trial periods in the range 2015 – 2025 days. For each trial period, we interpolated each flux curve to a common phase scale assuming a common epoch, then calculated the sum of the residuals between the three flux curves relative to the NICER fluxes. Figure 9 plots the summed residuals versus test phase. We found that a period of  $2023.03 \pm 1.12$  days yielded the smallest summed residuals. This period is 0.36 days shorter than the X-ray period derived by [Corcoran et al. \(2017\)](#), and 0.33 days longer than the period derived from analysis of the He II  $\lambda 4686$  emission line by [Teodoro et al. \(2016\)](#).

[Corcoran et al. \(2017\)](#) calculated an error of 0.71 which is smaller than our calculation. This is probably due to the high variability of the first observations made with high background conditions. But, the calculation of the period in this work is still in very good agreement with [Teodoro et al. \(2016\)](#) and [Corcoran et al. \(2017\)](#). We decided to keep the period of  $2023.40 \pm 0.71$  days to try to avoid the uncertainty added by the first NICER observations.

#### 4.4. X-ray Flaring

Just prior to minimum, the X-ray emission from  $\eta$  Car brightens and undergoes a period of rapid variability (“flares”) which have been observed by *RXTE*, *Swift*, and now NICER. X-ray “flaring” seen by NICER was first observed on MJD 58802 (15 November 2019, [Corcoran et al. 2019](#)), about 90 days prior to the X-ray minimum, similar to the start of the flare interval seen by *RXTE* and *Swift*. During the flare interval, the X-ray flux in the 2 – 10 keV band changes dramatically on timescales of days. This rapid X-ray variability has been seen by all three instruments. However, the *RXTE* cycle 0 observations were not obtained as frequently as observations in latter cycles, which meant some of the short-timescale variations were not sampled as completely as they were in subsequent cycles. Except for the undersampled *RXTE* cycle 0 observations, the maximum fluxes in the flares are similar.

To quantify the flaring observed by NICER we adopted a process similar to that used by [Moffat & Corcoran \(2009\)](#), namely we estimate an underlying smooth flux baseline by eye, and then subtracted this baseline from the net NICER fluxes. One difference with [Moffat & Corcoran \(2009\)](#) analysis is that we use for the baseline flux observations that follow closely the  $1/D$  line in Figure 8. Also we use the same NICER baseline flux to calculate the *RXTE* and *Swift*

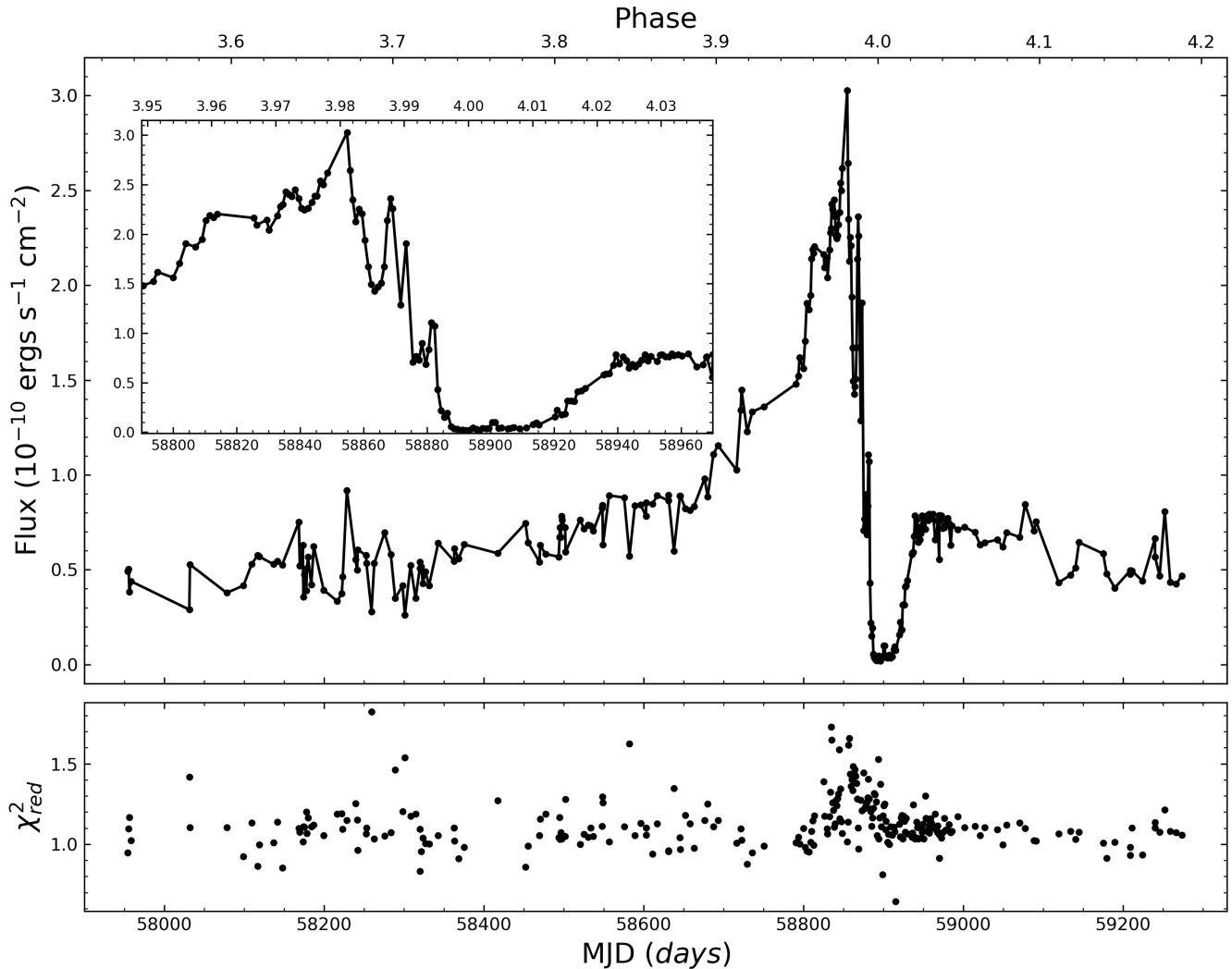


**Figure 7.** Flux between 2.0 - 10.0 keV observed by NICER. Fluxes are measured in XSPEC command Flux fitting a three collisional ionized plasma model with a Gaussian for the Fe K line. The bottom panel shows the reduced  $\chi^2$  from the fittings. At this point in our analysis, the background subtraction becomes more important since the goodness of the fit is highly affected if the background is not properly subtracted. Both background estimators improve the goodness of the fit but the 3C50 estimator shows a more stable behavior over the whole data set of observations.

residuals. The NICER fluxes, the baseline, and the residuals are shown in Figure 10. In Figure 10, the NICER measures are shown versus time using the epoch of periastron  $T_o$  given by Corcoran et al. (2017). Figure 10 also compares the residuals for the *RXTE* and *Swift* data (we do not include the first set of *RXTE* observations since the sampling frequency was not as high as in the later two cycles).

We do note that Moffat & Corcoran (2009) argued that long-duration, low-intensity X-ray flares could be seen near the apastron in *RXTE* observations. But NICER observations near apastron were obtained at the start of the mission and were affected by variations in local charged particle background and scattered solar radiation, so we can not claim that variations before MJD=58308 d ( $\sim \phi = 3.71$ ) are signs of intrinsic source X-ray variability. After  $\phi = 3.71$   $\eta$  Car’s NICER observations started to be taken at low background conditions.

After MJD=58400 ( $\sim \phi = 3.75$ ), Figure 10 shows small excess seen by NICER during the rise to X-ray maximum. Similarly, the excess in the residuals for the *RXTE* and *Swift* observations increases after  $\phi = 3.75$ . At phases  $\sim \phi > 3.93$ , *RXTE* and *Swift* residuals show a decrease in the width of flares. The shortening between flares can be seen by NICER just until  $\phi = 3.95$  since we do not have observations between  $3.92 > \phi > 3.95$ . The plot shows a

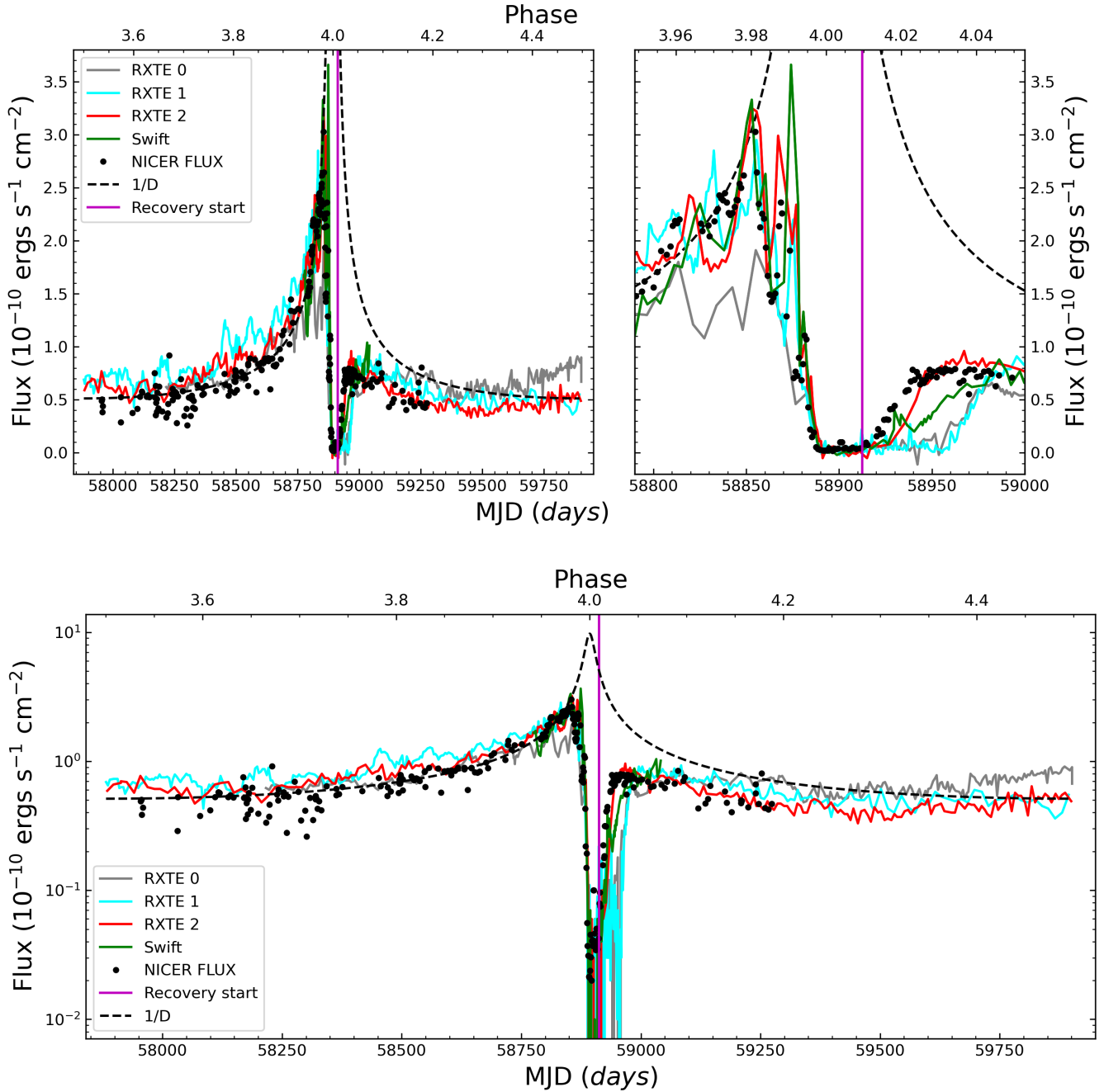


**Figure 8.** *Top:* Comparison of the 2 – 10 keV band fluxes from NICER, and earlier *RXTE* and *Swift* observations from Corcoran et al. (2017). The earlier measures have been advanced by 4, 3, 2, and 1 periods for the *RXTE* cycle 0, 1, 2 and *Swift* data, respectively, for comparison to the NICER measures. A  $1/D$  curve is shown by the dashed line. *Bottom:* Flux in log scale, to emphasize the depth of the X-ray minimum and the maximum height of the  $1/D$  curve.

break up at  $\phi \approx 3.97$  when the X-ray flux is approaching its maximum. The flares are not clearly seen at the same time in each orbital cycle, though some coincidences between cycles do occur. After X-ray maximum flux, during the plunge, the flares peaks show more coincidences between different cycles but this can be just a bias due to the fast orbital motion close to the periastron passage.

#### 4.5. Variations in X-ray Absorption

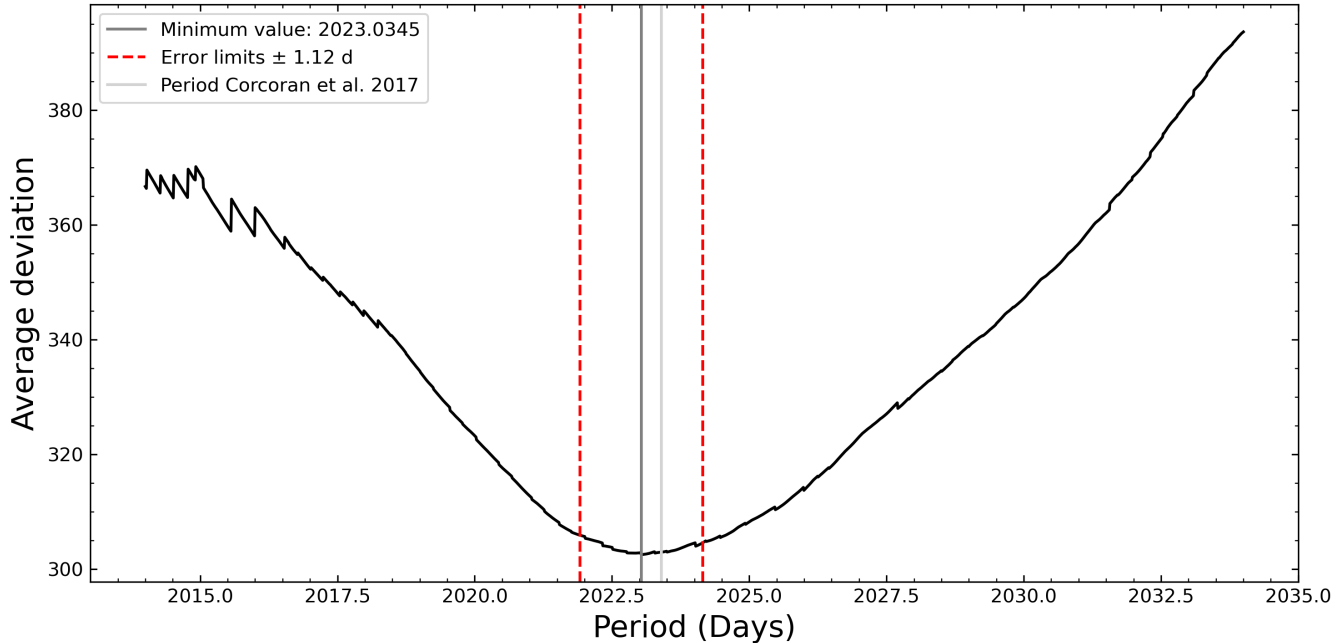


**Figure 9.** Sum of the square of the residuals for the *RXTE*, *Swift*, and NICER X-ray flux curves phased for periods in the range 2015 – 2035 days. Including the NICER data, the best X-ray period is 2023.035 days (dark gray line). The light gray line is the period calculated in Corcoran et al. (2017). The red lines are the limits of the error calculated in this work.

Figure 11 shows the derived variation in column density from the analysis of the NICER spectra compared to the column densities derived from the analysis of the *Swift* spectra in 2014 (Corcoran et al. 2017). The NICER column densities show substantial scatter between  $2 \times 10^{22} \text{ cm}^{-2}$  to  $2 \times 10^{23} \text{ cm}^{-2}$  before phase 3.97. Derived column densities may be influenced by uncertainties in our estimate of the background and contamination by the soft OE emission below 2 keV. As flux increases, column-densities measures become more precise and show a quasi-exponential increase reaching a maximum value of  $N_H \approx 10^{24} \text{ cm}^{-2}$  the end of the deep X-ray minimum. Note that near the X-ray minimum determining the column density precisely is difficult because the flux level is so low and the spectrum not well defined in the individual NICER observations. After reaching maximum, the measured column densities show a quasi-exponential decline through the shallow minimum, which appears to be fairly symmetric to the quasi-exponential increase seen up through the deep minimum. This is somewhat surprising since the distortion of  $\eta$  Car-A’s wind is very different before the X-ray minimum and afterward, as shown by hydrodynamical modeling (see, for example, Madura et al. 2013).

Figure 11 also shows previous column density measures from the literature and column densities determined from a new analysis of available CHANDRA High Energy Transmission Grating spectra (Espinoza-Galeas et al., 2022, in prep.). In general there is good agreement between the NICER column densities and the *Swift* column densities obtained during the previous periastron passage in 2014. There are significant discrepancies between the NICER column densities and others measured from “snapshot” spectra obtained by *Suzaku*, *XMM-Newton*, and CHANDRA at some phases. In particular the maximum column measured by Hamaguchi et al. (2014) is near  $10^{25} \text{ cm}^{-2}$ , about an order of magnitude larger than the maximum NICER column. It may be that the maximum NICER column is underestimated due to residual soft circumstellar emission in the NICER field of view and due to uncertainties in background estimation. There are also large differences, up to an order of magnitude, during the high-absorption interval following X-ray minimum between the Hamaguchi et al. (2007b) measures, the CHANDRA measure and the *Swift* and NICER column densities. The column densities and temperatures we derive from our analysis of the NICER spectra differ from those derived by Kashi et al. (2021). These differences are mostly due to the different methods used in the spectral analysis. Kashi et al., following Hamaguchi et al. (2007b), apparently derived column densities and temperatures by fitting the hard-band portion of the spectrum with a simple absorbed 1-temperature model (see their table 2). Their analysis tends to underestimate the X-ray temperature but overestimate the emission measure

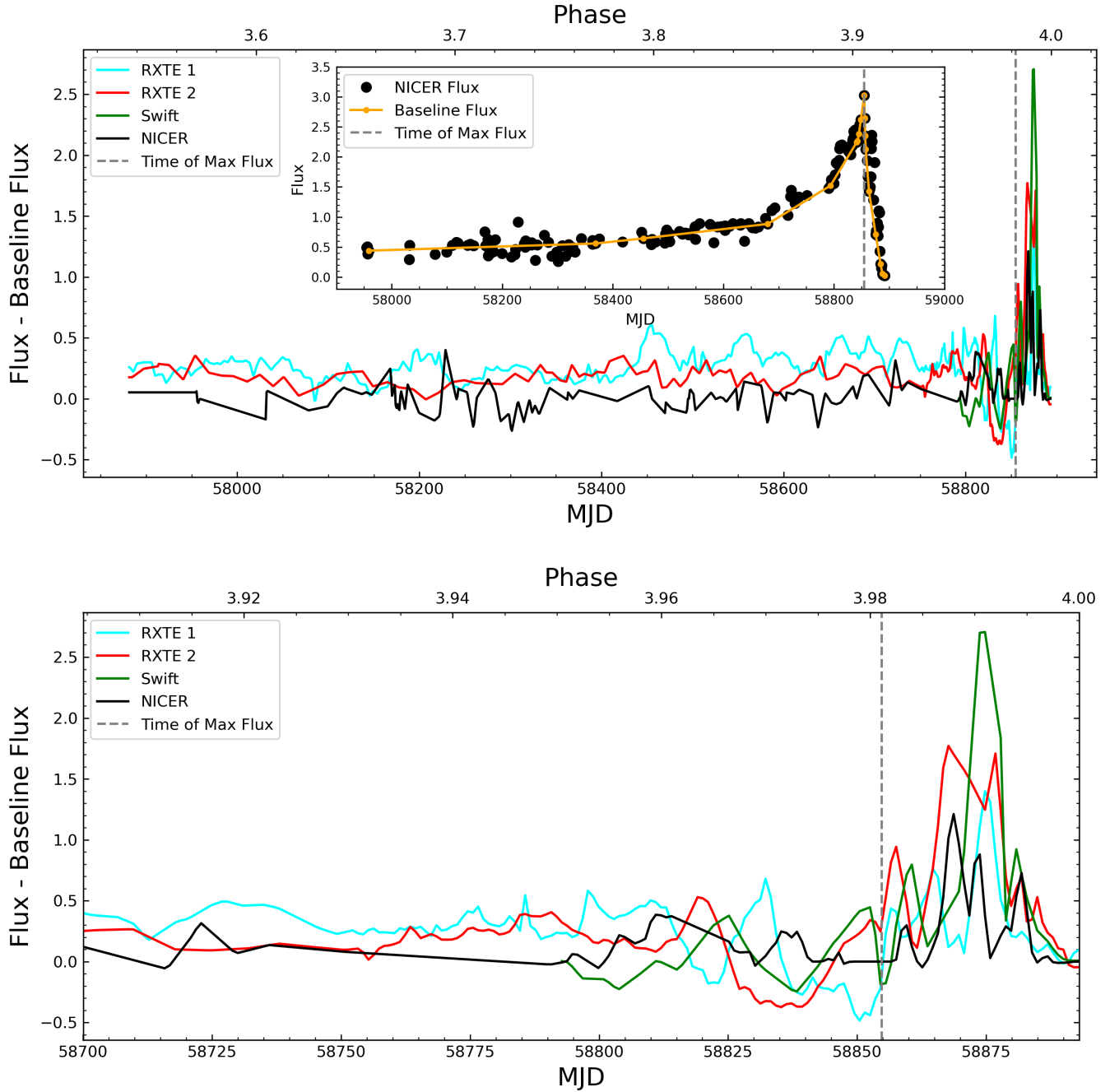


**Figure 10.** *Top:* Residuals of NICER (black solid line), *RXTE* (cyan and red), and *Swift* (green). The dashed vertical line shows the observed maximum of the X-ray count rate as seen by NICER. The NICER X-ray 2 – 10 keV flux curve vs. MJD. The orange line shows the baseline flux used to calculate the residuals, which approximately follows a  $1/D$  variation before maximum, then it is followed by the lowest values during plunge. *Bottom:* Same as top zooming the times close to maximum X-ray emission and before minimum X-ray emission.

and column densities. We use a more realistic model which describes the complex emission seen in the high resolution CHANDRA spectra (as discussed above) and which also includes analysis of lower-energy emission which is most sensitive to column density changes. These temperatures are also consistent with the observed Fe XXVI/Fe XXV ratio  $\sim 0.1 - 0.3$ , seen in CHANDRA spectra near apastron (Espinoza-Galeas 2021).



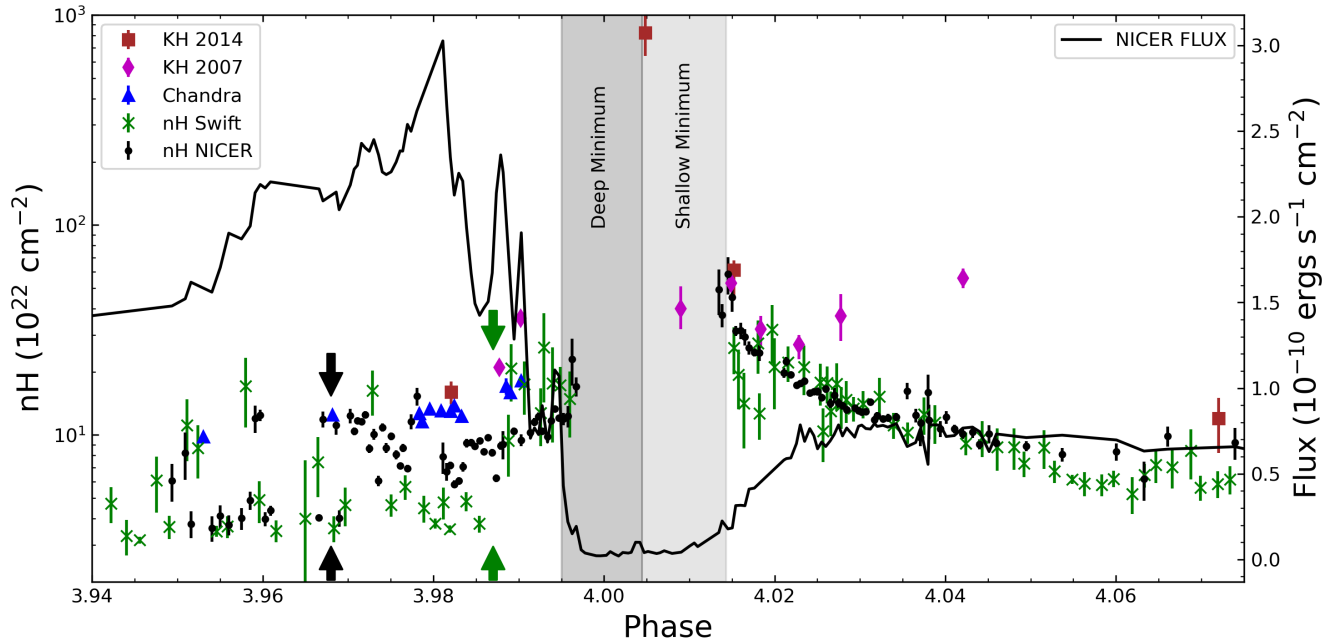


**Figure 11.** Column densities observed by NICER compared to *Swift* column densities from the last orbital cycle (Corcoran et al. 2017). The magenta diamonds are previous measurements from Hamaguchi et al. (2007b, KH 2007b), while the red squares are from CHANDRA, *XMM-Newton*, and *Suzaku* spectra Hamaguchi et al. (2014, KH 2014). Blue triangles are column densities derived from analysis of CHANDRA grating spectra (D. Espinoza-Galeas et al., 2022, in preparation). The gray regions mark the “deep” and “shallow” minimum. Notice the good agreement in *Swift* and NICER observations after the shallow minimum. The arrows mark the abrupt, step-like increases in column density (near  $\phi=3.99$  for *Swift* and  $\phi = 3.97$  for NICER).

#### 4.6. X-ray Temperatures

The maximum X-ray temperature of the shocked gas in a colliding-wind binary should be approximately constant with orbital phase if the pre-shock velocities of the winds are near terminal velocity at every point in the orbit. Figure ?? The temperature of this high-temperature component shows significant scatter for most of the orbit, as can be seen in the upper panel, but overall there is not much evidence for significant change in temperature when the stars are well separated. In the interval  $3.5 < \phi < 3.9$  the weighted average temperature for this component  $kT = 3.84 \pm 1.05$  keV. For comparison, Hamaguchi et al. (2007b) derived a temperature of  $kT = 4.6^{+0.2}_{-0.1}$  keV near  $\phi = 1.47$ . Over the entire orbit, the weighted average temperature is similar,  $kT = 3.74 \pm 1.06$  keV.

The bottom panel in the Figure 12 shows the temperature variation near the X-ray maximum/minimum, in the phase range  $3.85 < \phi < 4.05$ . Temperature measures are more precise near the X-ray maximum, when the hard emission component is bright. The temperatures at X-ray minimum are not shown because it is not possible to get reliable measurements from the NICER spectra between 2.0 - 10.0 keV since the source is too faint. Starting after  $\phi > 4.10$ , the temperature is nearly constant at  $kT = 3.6 \pm 0.8$  keV, and again shows more scatter starting at  $\phi = 4.06$ , with an average temperature near 4.0 keV. As can be seen from Fig. 12, there is a significant, apparently monotonic decline in the temperature of this component starting at  $\phi = 3.96$ . This decline in temperature happens before the plunge of  $\eta$  Car’s X-ray emission to minimum, when the stars are moving towards each other as they approach the point of periastron. The temperature shows a mostly linear decline from about  $4.5 \pm 0.4$  keV ( $T = 52.2 \times 10^6$  K) to approximately  $3.0 \pm 0.5$  keV ( $T = 34.8 \times 10^6$  K) in only 60 days, cooling at a rate of about  $3 \times 10^5$  K day $^{-1}$ . However, Hamaguchi et al. (2007b) measured higher temperatures in the phase range  $1.988 < \phi < 1.99$  from 2 *XMM-Newton* spectra obtained just before the 2003 X-ray minimum, reporting temperatures of  $kT = 4.5$  keV at 1.988 and 5.4 keV at 1.99, neither of which was consistent with cooling during this interval in 2003. As a check on the phase dependence of the hot component temperature, we also measured temperatures from CHANDRA HETGS spectra obtained contemporaneously with the NICER observations, using the same spectral model (Espinoza-Galeas 2021, Espinoza Galeas et al., 2021, in prep.) We found good agreement between the temperatures derived from the fits to

the CHANDRA HETGS spectra and the NICER spectra, and in particular that the CHANDRA temperatures showed a similar monotonic decline in the phase interval 3.98 – 3.99

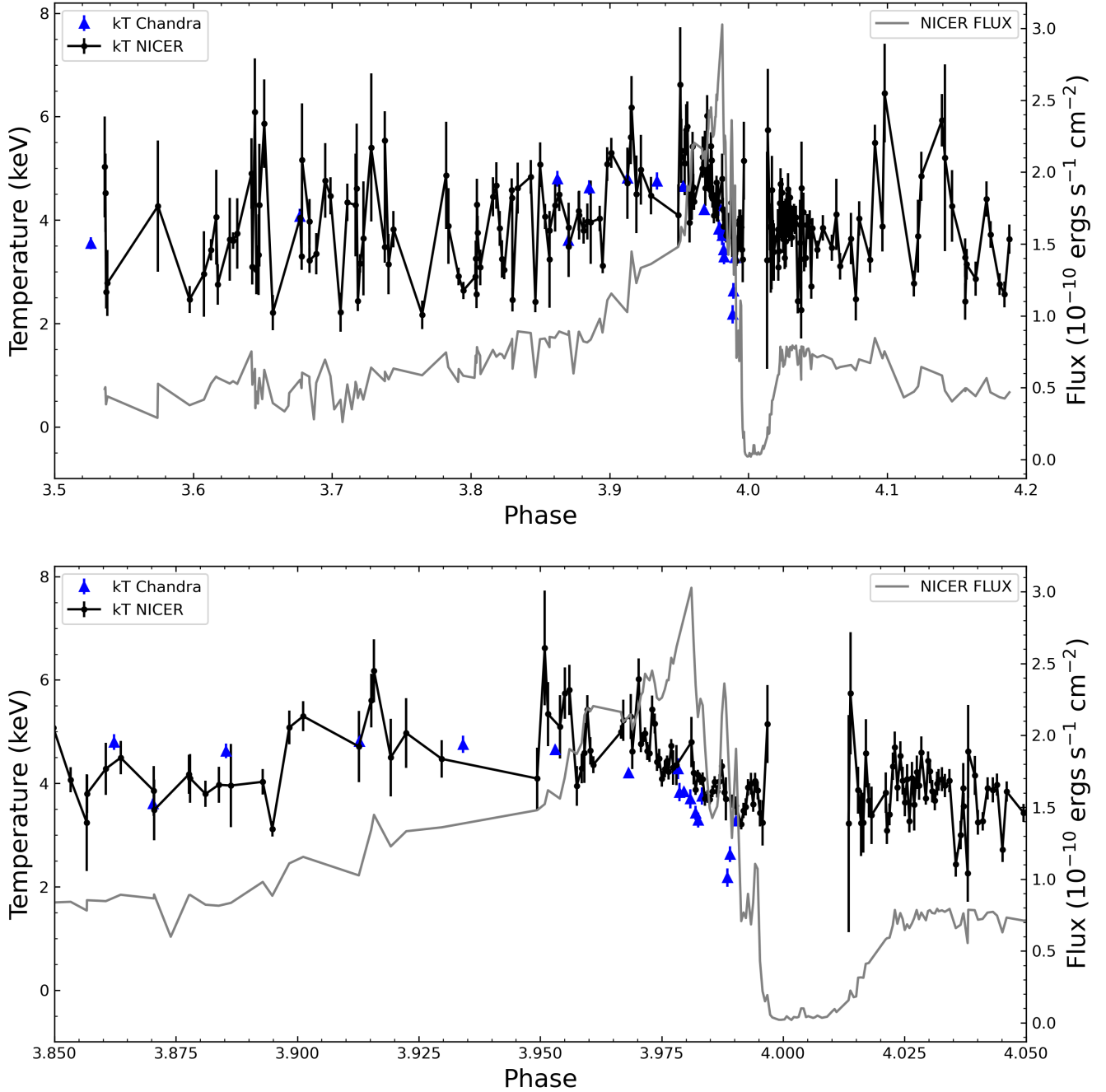


**Figure 12.** *Top:* Temperatures vs phase of the hot component for  $\eta$  Car’s NICER observations on this work. *Bottom:* Same as the top panel near the X-ray minimum ( $3.85 < \phi < 4.05$ ). A clear decline in temperature can be seen starting at  $\phi \approx 3.97$ , a phase when the 2 – 10 keV X-ray flux is still increasing. By  $\phi \approx 4.02$ , the temperature has stabilized around 4.0 keV, with increased variability after  $\phi \approx 4.06$ . Note that the spectrum is too faint during the X-ray minimum ( $3.995 < \phi < 4.015$ ) for a reliable measure of the X-ray temperatures.

We also measured the temperature of the cooler component. The cooler emission originates from gas farther downstream from the shock apex, and is a combination of hotter gas that has cooled as it flows away from the shock apex and

lower-temperature shocked gas produced where the wind flows collide indirectly. The cool component temperatures are often difficult to constrain because of the soft emission from the constant outer debris X-ray emission below 2 keV. Several of the fits reach our assumed 1 keV lower constraint. Temperatures for this cooler component are easier to constrain near the X-ray maximum when the source is bright, but also depend on accurate assessment of the increasing absorption column. In the flare region close to X-ray maximum, the temperatures of the cool component show interesting behavior, as can be seen in Figure 13. At phases between 3.97 and 4.00, the cool component temperatures are somewhat higher than at earlier phases, and show a possible correlation with the flares, where higher flux seems to correspond to higher values of the cool component temperature.

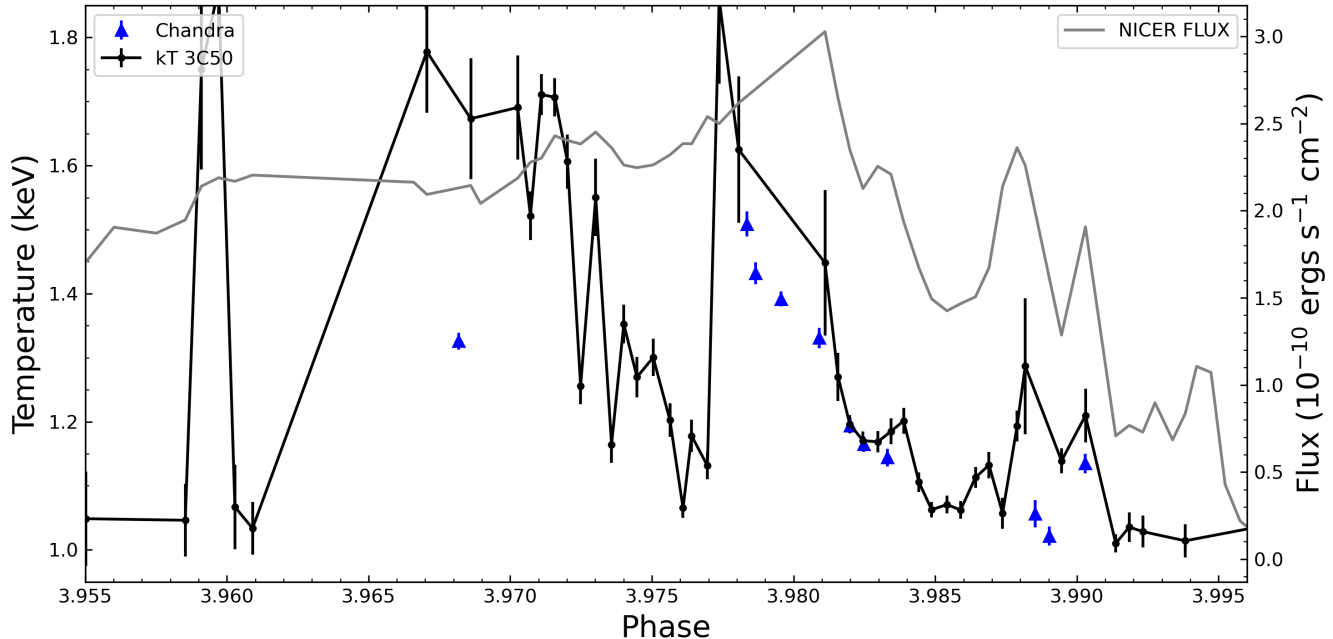


**Figure 13.** NICER temperatures vs phase for the cool component between phases 3.95 to 4.00. The flare region shows an apparent correlation between temperatures and flux, where the peak of the cool component temperature appears to coincide with the flare peaks.

## 5. DISCUSSION

### 5.1. Changes in Mass-Loss Rates

The X-ray emission measure and column density provide arguably the most robust measure of the variation in mass loss from the winds of  $\eta$  Car-A and  $\eta$  Car-B. This is because the 2 – 10 keV thermal emission is dependent on the density of the shocked wind of  $\eta$  Car-B along the shock front, while the absorption of this emission suffered by this emission depends on the density profile of the wind of  $\eta$  Car-A as the X-ray emission travels from the shock front through the wind of  $\eta$  Car-A to the observer. The excellent agreement in derived column densities between the NICER and *Swift* observations shows that there has been no significant change in the mass-loss rate from  $\eta$  Car-A in the 2014-2020 time interval. There is also, generally, good agreement between the NICER column densities and most of the column densities from earlier cycles measured by Hamaguchi et al. (2007b) and Hamaguchi et al. (2014) which suggests, for the most part, a fairly constant density profile through the wind of  $\eta$  Car-A. As shown in Figure 11, however, there are some disagreements between the NICER and *Swift* column densities and the earlier measures, in particular in the interval  $0.02 < \phi < 0.05$ , in which the *Swift* and NICER column densities are significantly lower than the two measures reported in Hamaguchi et al. (2007b) in this phase range. This discrepancy may indicate that a significant change in the wind density profile from  $\eta$  Car-A occurred sometime between 2003 and 2014. Conclusively deciding the nature of this discrepancy is difficult because of the poor time sampling of the 2003 observations, and stochastic variations in the density profile caused by local clumping in the wind of  $\eta$  Car-A cannot be entirely ruled out

(though the discrepancy, about a factor of 5 in derived column at  $\phi \approx 0.04$  seems large for a local perturbation which might be produced, for example by a wind clump or other local density enhancement). At this phase, simulations show that the X-ray emission from the colliding-wind bow shock passes through the distorted wind from  $\eta$  Car-A as the wind is wrapped around the leading wall of the bow shock, and it is plausible that small stochastic changes in this region of the wind could have large effects on the absorbing column.

Overall, the measured X-ray column densities from the 2003-2020 interval agree to better than 40-50% with previous observations. Since column density is directly proportional to  $\dot{M}$ , and since the NICER and *Swift* column densities tend to be lower than the earlier measurements, this agreement constrains the decline in the mass-loss rate from  $\eta$  Car-A,  $\dot{M}_A$ , to  $\dot{M}_A/\dot{M}_A < 2.5$  percent per year.

The X-ray flux in the 2 – 10 keV band depends on the emission measure of the shocked wind of  $\eta$  Car-B, which is proportional to the mass-loss rate from the companion,  $\dot{M}_B$ . Thus comparing fluxes in the 2 – 10 keV band from different orbital cycles provides a measure of the changes in mass-loss rate from the companion,  $\dot{M}_B$ , over time. It is best to compare fluxes when the stars are close to apastron, since the shock is stable and cooling is adiabatic. As shown in Figure 8, there is good agreement between the *RXTE* Cycle 1 (2003) and Cycle 2 (2009) observations near  $\phi \approx 3.8$ , while the *RXTE* Cycle 0 and NICER fluxes are about 25% lower. This could indicate non-monotonic variability in the mass-loss rate from the companion; also this can indicate some systematic error in calibration between the *RXTE* Cycle 0 and NICER fluxes and the *RXTE* fluxes from the other two cycles. Kashi et al. (2021) suggest that  $\eta$  Car’s different X-ray emission recoveries are the result of a decrease in  $\eta$  Car-A’s wind. If this were the case we should expect significant differences in column densities for different recoveries. But as shown in Figure 11, the column densities in the recoveries observed by *Swift* and NICER are very similar, showing no significant changes in the mass-loss despite the different recovery durations.

### 5.2. Shock Temperatures, Wind Velocities, and the Radius of $\eta$ Car-B

As seen in Figure 12, the hotter component shows a fairly constant X-ray temperature of  $kT = 3.84 \pm 1.05$  keV up to  $\phi \approx 3.96$ , after which there is a rather linear decline up to  $\phi = 3.99$  (at which point the spectra become too faint for analysis). The hottest plasma in the colliding-wind shock originates near the apex of the shock cone, where the winds collide nearly head on, and as the stars approach periastron passage, the apex of the colliding-wind shock moves closer to the companion star. If the apex enters the region of the companion’s wind where the wind is still accelerating and has not yet reached terminal velocity, this would cause a drop in the temperature of the hot shocked gas near the apex. The drop in temperature of  $\approx 2/3$  by  $\phi = 3.99$  compared to the temperature at  $\phi = 3.96$  when the decline apparently starts, suggests a drop in the pre-shock velocity of the fast wind of  $\eta$  Car-B. Since  $T \propto V^2$ , this corresponds to a decrease in the pre-shock velocity of the wind of  $\eta$  Car-B of  $(V_1 - V_2)/V_1 \approx 2.5\%$  where  $V_1$  is the wind velocity at  $\phi = 3.96$  and  $V_2$  is the wind velocity  $\phi = 3.99$ .

Figure 14 shows the expected variation in separation of the two stars and the distance from  $\eta$  Car-B to the stagnation point of the shock, derived by balancing the pressure of the wind from  $\eta$  Car-A and  $\eta$  Car-B between the two stars. Figure 14 also shows the derived change in wind velocity assuming a standard wind velocity law  $V(r) = V_{\infty,B}(1 - R_B/r)^\beta$ , where  $V(r)$  is the velocity of  $\eta$  Car-B’s wind at a distance  $r$  from the star,  $V_{\infty,B}$  is the terminal velocity of  $\eta$  Car-B’s wind, and  $\beta$  the wind acceleration constant (usually close to 1 for most radiatively-driven winds). Note that very near periastron, the apex moves very close to the companion and the velocity calculation breaks down. The dashed vertical gray lines indicate the phase interval of the observed cooling of the hotter component, while the red line shows the change in wind velocity implied by the temperature decreases, assuming  $T \propto V^2$ . The intersection of the dashed vertical gray and red line show the derived velocities at the start and end of the observed cooling interval. We find that the derived change in wind velocity is fairly well matched by the calculated variation in  $\eta$  Car-B’s pre-shock wind velocity at the distance of the shock cone apex over this range of orbital phase, if the radius of  $\eta$  Car-B is  $\approx 30 R_\odot$ . Ionization modeling by Verner et al. (2005) yielded values of  $T_{eff,B} = 37,200$  K and  $\log L_B/L_\odot \approx 5.97$ , implying an effective radii of  $23.6 R_\odot$ , slightly smaller than the radius which reasonably describes the X-ray cooling if  $\beta = 1$  shown in Figure 14; but, given the uncertainties and assumptions, these numbers are in good agreement. On the other hand, photoionization modeling by Mehner et al. (2010) suggests a somewhat hotter but fainter companion star,  $T_{eff,B} = 39,000$  K and  $\log L_B/L_\odot \approx 5.60$ , yielding an effective radius of only  $14.0 R_\odot$ . We can reasonably describe the observed X-ray cooling curve with these radii, but both require higher values of  $\beta$  (indicating a more slowly accelerating wind),  $\beta \approx 1.5$  and  $\beta \approx 3.0$  for the Verner et al. and Mehner et al. radii, respectively.

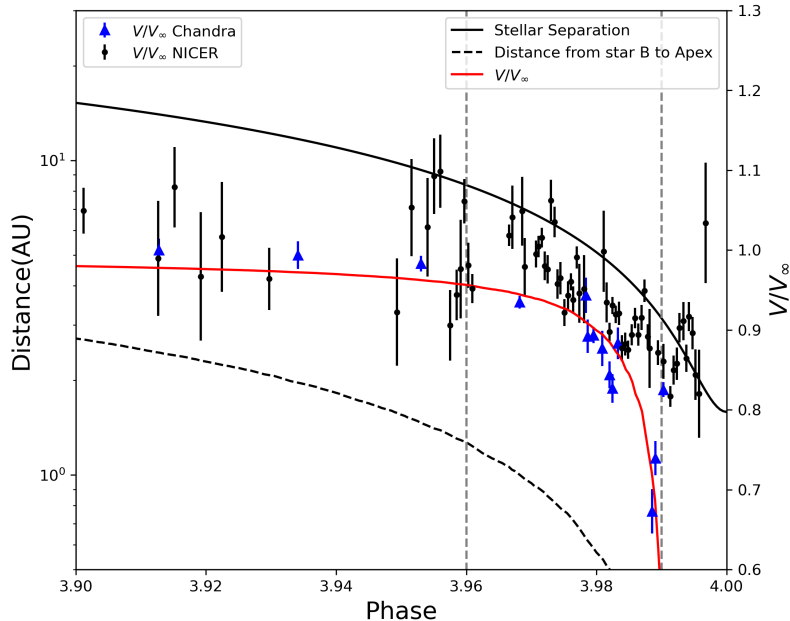


**Figure 14.** The Figure shows the expected variation in stellar separation (solid black line) with the  $v/v_\infty$  of  $\eta$  Car B’s wind at the location of the apex (red line), derived using the system and stellar parameters given in Table 1, and a radius of  $\eta$  Car-B =  $30 R_\odot$ . The gray vertical dashed lines indicate the observed phase interval of the decline in the X-ray temperature of the hot component.

### 5.3. The Deep/Shallow Minimum Transition

The NICER campaign has provided the best measure obtained so far of the variations in X-ray flux and X-ray spectral properties around the X-ray minimum. The NICER HR in Figure 4 shows the transition between the “deep” and “shallow” states of the X-ray minimum first identified by Hamaguchi et al. (2014) from a set of only five CHANDRA ACIS spectra. Figure 4 also show that the deep minimum interval lasts for an interval of 18 days, starting at  $\phi = 3.995$  and ending at  $\phi = 4.004$ , with the transition to the shallow minimum. The shallow interval ends at  $\phi = 4.013$ , a duration of 18 days while the shock gradually strengthens and the absorption dissipates as the companion moves around and away from  $\eta$  Car-A. This is consistent with the interpretation offered in Hamaguchi et al. (2014), who suggested that the deep minimum is produced by occultation of the X-ray emitting gas by the optically-thick inner wind of  $\eta$  Car-A, which completely hides the X-ray emission from the colliding-wind shock, plus a decline in X-ray emissivity near periastron passage, followed by a gradual strengthening of the shock and a re-heating to X-ray emitting temperatures.

### 5.4. The Column Density Variation Through $\eta$ Car’s Orbital Motion

The column density from the hot component of  $\eta$  Car X-ray emission shows variability through all the NICER monitoring program. Those changes go up to one order of magnitude in column density (Figure 11), with intervals no longer than  $\sim 0.1$  in phase. The variations indicate changes in the amount of material in front of the apex of the CWR in our line of sight. The occurrence and duration of the  $N_H$  variations before  $\phi = 3.95$  do not show a particular correlation with flux or phase. Stochastic changes in  $\eta$  Car A’s wind by clumps could explain the variability observed. The lack of more frequent observations before  $\phi = 3.95$  makes difficult a deeper analysis of those variations in column density.

After  $\phi = 3.94$  more frequent NICER observations were allocated. Between phases 3.96 and 3.97 the  $N_H$  shows a particular stability in the measurements. The stability of so many subsequent measurements was not observed before. The measurements of  $N_H$  between  $3.97 < \phi < 3.98$  makes clear the increase of one order of magnitude in column density after phase 3.98. After  $\phi = 3.98$  the column density keeps almost constant for the next  $\Delta\phi \approx 0.1$ . The step of one order of magnitude at  $\phi = 3.97$  can be also due a clump in  $\eta$  Car A wind. Another interesting explanation for the

step change in column density is a transition between the wind from  $\eta$  Car B and  $\eta$  Car A separated by the walls of the cone formed by the CWR.

### 5.5. Variation in the Duration of the X-ray Minimum

As first noted by Espinoza-Galeas et al. (2020), NICER showed that the duration of the X-ray minimum in 2020 was the shortest seen in any of the four orbital cycles monitored so far. The first two minima seen by *RXTE* in 1997 and 2003 had nearly identical X-ray minimum durations, while the *RXTE* monitoring of the 2009 minimum had a significantly shorter duration. Any hypothesis needs to explain the apparently stochastic behavior observed in the starting time of the X-ray recovery observed in Figure 8. Corcoran et al. (2010) suggested that the different recoveries are due to a decline in  $\eta$  Car’s wind momentum. The decline can be caused by a drop in mass-loss or wind terminal velocity, or some combination. If so, we might expect to see differences in column densities when comparing X-ray spectra obtained during recovery in different orbital cycles. Figure 11 compares the column densities from cycle 3 (from *Swift*) and cycle 4 (NICER). Although the duration of the cycle 3 minimum was substantially longer than the cycle 4 recovery (See Figure 8), after  $\phi \approx 4.020$  the column densities from *Swift* and NICER are very similar. This suggests that the differences in the duration of the cycle 3 and cycle 4 minima was not produced by a significant change in the wind momentum of the primary. Kashi et al. (2021) and Kashi & Soker (2009) propose that accretion at periastron weakens the mass-loss rate of  $\eta$  Car-A every cycle, implying that any new X-ray emission recovery should be shorter than the previous one. But as discussed above it is not likely that  $\eta$  Car-A’s wind has weakened significantly from 2015 to 2020 based in the column densities. Also, the 2009 minima was shorter than the 2015 minima as shown in Figure 8, indicating that there is no systematic weakening of  $\eta$  Car-A’s wind with time.

The comparison of the NICER and *Swift* observations around X-ray minimum suggests that another mechanism produces the variation in duration of the X-ray recoveries. Winds from luminous hot stars are prone to line-deshadowing instabilities (LDIs) that can randomly create localized variations in wind density (Owocki et al. 1988). Figure 4 in Owocki et al. (1988) shows how those instabilities can increase the velocity of the wind from  $\sim 500$  km/s to  $\sim 1250$  km/s, especially in the dense inner parts of the wind. Such local density enhancements (clumps) interacting with the colliding-wind bow shock can move the stagnation point of the CWR closer to  $\eta$  Car B, reducing the pre-shock wind speed and reducing the hot X-ray flux from the bow shock. In this scenario, we can still have regions where the shock of the winds can generate high energy X-rays but distributed over a broader region, that together with a high column density, produces the shallow minimum. The shallow minimum duration will be dependent on the size of the clump and the time when the clump forms. Once the clump passes the shock,  $\eta$  Car B’s wind can accelerate enough to re-form the hot shocked gas in the CWR between the stars, starting the recovery of the hard X-ray flux.

We suggest that the sudden, step-like increase in column density before the X-ray minimum (See Figure 11) indicates the formation of a dense clump produced by the LDIs in the inner wind of  $\eta$  Car A. This step is observed at a later phase in cycle 3 than in cycle 4, suggesting a connection between the clump formation time and the time of recovery. Clumps that form later produce a longer X-ray minimum, while clumps which form earlier in orbital phase pass beyond the bow shock earlier, producing an earlier X-ray recovery and shorter X-ray minimum.

### 5.6. The Nature of Rapid X-ray Variability

As discussed in Section 4.4, NICER observed similar rapid X-ray variability, or “flares”, which become evident near X-ray maximum and are even seen during the decline to minimum. The comparison of the NICER 2 – 10 keV X-ray fluxes with those from *RXTE* Cycle 1 and Cycle 2 as a function of time shows no strong correlation. Moffat & Corcoran (2009) concluded that this flaring activity was produced by large, homologously-expanding localized overdensity regions, or clumps, in the wind of  $\eta$  Car-A.

The apparent coincidence of peaks in the temperature of the cool component with the peaks of some X-ray flares seen in Figure 13 can be interpreted in terms of the “clump” model of Moffat & Corcoran (2009). In this model, the pressure of a clump on the wall of the bow shock downstream from the apex could in principle decrease the opening angle of the bow shock, causing the winds to collide more directly, increasing the temperature of the downstream shocked wind while increasing the density of that portion of the shock producing an increase in X-ray flux from the shocked wind of the companion star.

## 6. CONCLUSIONS AND FUTURE WORK

NICER provides time-resolved measures of the 0.4-10 keV  $\eta$  Car’s X-ray spectrum from  $\phi \sim 3.5$  and ongoing. Flux measured by NICER follows the  $1/D$  behavior for most of the orbit, similar to *RXTE* and *Swift* lightcurves. NICER

observed that the plunge of the X-ray maximum started at  $\phi \sim 3.98$ , similar to the previous cycles indicating that it is strongly correlated with orbital phase. Inspection of  $\eta$  Car's NICER spectrum does not show evidence of a decrease in X-rays due to absorption, suggesting that the decrease in flux is due to a decrease in temperatures at the CWR. This is the first time we have evidence of temperature decrease in the CWR of  $\eta$  Car. The temperature of the hot component declines on approach to periastron passage, indicating that the shock apex is moving into the acceleration zone of the wind of  $\eta$  Car B.

Measurements of the HRs with NICER constrain the Deep minimum to  $3.995 < \phi < 4.004$  (18 days) and Shallow minimum from  $4.004 < \phi < 4.013$ . We have observed the shortest X-ray recovery: the flux starts to increase at  $\phi = 4.009$  which is  $\sim 7$  days earlier than the low limit estimated by Corcoran et al. (2010) in the 2009 periastron passage. The apastron fluxes do not change  $> 5\%$ , indicating a change no more than  $0.25\%$  in  $\dot{M}$  from  $\eta$  Car A or B. The absorption measured by NICER shows an agreement up to 90% after  $\phi = 4.01$ , giving us another indicator that  $\dot{M}$  from  $\eta$  Car A or  $\eta$  Car B has not changed significantly in the last two cycles.

The changes in the soft-band emission from the OE seen for the first time by NICER may be caused by the expansion of the ejecta. If so, simple analysis indicates that the X-ray luminosity near the time of the Great Eruption was about  $\sim 10^{41}$  ergs s $^{-1}$ . This is the first estimate of the X-ray luminosity of the Great Eruption and suggests that the X-ray luminosity at that time was comparable to the total luminosity at longer wavelengths.

#### ACKNOWLEDGMENTS

D. Espinoza Galeas gratefully acknowledges support from NASA grants #80NSSC19K1451 and #80NSSC21K0092, and SAO grant #GO9-20015A thru NASA. This work was conducted as part of doctoral research conducted at The Catholic University of America. M. F. Corcoran and K. Hamaguchi are supported under the CRESST-II cooperative agreement #80GSFC17M0002 with the NASA/Goddard Space Flight Center. C. M. P. Russell was supported by SAO grant #GO0-21006A through NASA; this support is gratefully acknowledged. This research has made use of data and software provided by the High Energy Astrophysics Science Archive Research Center (HEASARC), which is a service of the Astrophysics Science Division at NASA/GSFC. This research has made use of NASA's Astrophysics Data System. This research made use of Astropy,<sup>5</sup> a community-developed core Python package for Astronomy (Astropy Collaboration et al. 2013, 2018).

*Software:* XSPEC (Arnaud 1996), astropy (The Astropy Collaboration 2013, 2018)

#### REFERENCES

- Anders, E., & Grevesse, N. 1989, *GeoCoA*, 53, 197, doi: [10.1016/0016-7037\(89\)90286-X](https://doi.org/10.1016/0016-7037(89)90286-X)
- Arzoumanian, Z., Gendreau, K. C., Baker, C. L., et al. 2014, in *Society of Photo-Optical Instrumentation Engineers (SPIE) Conference Series*, Vol. 9144, *Space Telescopes and Instrumentation 2014: Ultraviolet to Gamma Ray*, 914420, doi: [10.1117/12.2056811](https://doi.org/10.1117/12.2056811)
- Astropy Collaboration, Robitaille, T. P., Tollerud, E. J., et al. 2013, *A&A*, 558, A33, doi: [10.1051/0004-6361/201322068](https://doi.org/10.1051/0004-6361/201322068)
- Astropy Collaboration, Price-Whelan, A. M., SipHocz, B. M., et al. 2018, *aj*, 156, 123, doi: [10.3847/1538-3881/aabc4f](https://doi.org/10.3847/1538-3881/aabc4f)
- Corcoran, M. F. 2005, *AJ*, 129, 2018, doi: [10.1086/428756](https://doi.org/10.1086/428756)
- Corcoran, M. F., Hamaguchi, K., Gendreau, K., et al. 2019, *The Astronomer's Telegram*, 13327, 1
- Corcoran, M. F., Hamaguchi, K., Pittard, J. M., et al. 2010, *ApJ*, 725, 1528, doi: [10.1088/0004-637X/725/2/1528](https://doi.org/10.1088/0004-637X/725/2/1528)
- Corcoran, M. F., & Ishibashi, K. 2012, in *Astrophysics and Space Science Library*, Vol. 384, *Astrophysics and Space Science Library*, ed. K. Davidson & R. M. Humphreys, 195, doi: [10.1007/978-1-4614-2275-4\\_9](https://doi.org/10.1007/978-1-4614-2275-4_9)
- Corcoran, M. F., Ishibashi, K., Swank, J. H., & Petre, R. 2001, *ApJ*, 547, 1034, doi: [10.1086/318416](https://doi.org/10.1086/318416)
- Corcoran, M. F., Rawley, G. L., Swank, J. H., & Petre, R. 1995, *ApJL*, 445, L121, doi: [10.1086/187904](https://doi.org/10.1086/187904)
- Corcoran, M. F., Petre, R., Swank, J. H., et al. 1998, *ApJ*, 494, 381, doi: [10.1086/305190](https://doi.org/10.1086/305190)
- Corcoran, M. F., Liburd, J., Morris, D., et al. 2017, *ApJ*, 838, 45, doi: [10.3847/1538-4357/aa6347](https://doi.org/10.3847/1538-4357/aa6347)
- Corcoran, M. F., Hamaguchi, K., Espinoza, D., et al. 2020, *The Astronomer's Telegram*, 13516, 1
- Damineli, A. 1996, *ApJL*, 460, L49+, doi: [10.1086/309961](https://doi.org/10.1086/309961)
- Damineli, A., Conti, P. S., & Lopes, D. F. 1997, *New Astronomy*, 2, 107, doi: [10.1016/S1384-1076\(97\)00008-0](https://doi.org/10.1016/S1384-1076(97)00008-0)

- Damineli, A., Hillier, D. J., Corcoran, M. F., et al. 2008, *MNRAS*, 384, 1649, doi: [10.1111/j.1365-2966.2007.12815.x](https://doi.org/10.1111/j.1365-2966.2007.12815.x)
- Davidson, K. 1971, *MNRAS*, 154, 415
- Davidson, K., & Humphreys, R. M. 1997, *ARA&A*, 35, 1, doi: [10.1146/annurev.astro.35.1.1](https://doi.org/10.1146/annurev.astro.35.1.1)
- Espinoza-Galeas, D. A. 2021, PhD thesis, The Catholic University of America
- Espinoza-Galeas, D. A., & Corcoran, M. F. 2020, in *American Astronomical Society Meeting Abstracts*, American Astronomical Society Meeting Abstracts, 377.04
- Espinoza-Galeas, D. A., Corcoran, M. F., Hamaguchi, K., et al. 2020, *The Astronomer's Telegram*, 13636, 1
- Gaviola, E. 1950, *ApJ*, 111, 408. [http://adsabs.harvard.edu/cgi-bin/nph-bib\\_query?bibcode=1950ApJ...111..408G&db\\_key=AST](http://adsabs.harvard.edu/cgi-bin/nph-bib_query?bibcode=1950ApJ...111..408G&db_key=AST)
- . 1953, *ApJ*, 118, 234. [http://adsabs.harvard.edu/cgi-bin/nph-bib\\_query?bibcode=1953ApJ...118..234G&db\\_key=AST](http://adsabs.harvard.edu/cgi-bin/nph-bib_query?bibcode=1953ApJ...118..234G&db_key=AST)
- Gendreau, K. C., Arzoumanian, Z., & Okajima, T. 2012, in *Proc. SPIE, Vol. 8443, Space Telescopes and Instrumentation 2012: Ultraviolet to Gamma Ray*, 844313, doi: [10.1117/12.926396](https://doi.org/10.1117/12.926396)
- Groh, J. H., Hillier, D. J., Madura, T. I., & Weigelt, G. 2012, *MNRAS*, 423, 1623, doi: [10.1111/j.1365-2966.2012.20984.x](https://doi.org/10.1111/j.1365-2966.2012.20984.x)
- Hamaguchi, K., Corcoran, M. F., Gull, T., et al. 2007a, in *Astronomical Society of the Pacific Conference Series, Vol. 367, Massive Stars in Interactive Binaries*, ed. N. St.-Louis & A. F. J. Moffat, 257–+
- Hamaguchi, K., Corcoran, M. F., Gull, T., et al. 2007b, *ApJ*, 663, 522, doi: [10.1086/518101](https://doi.org/10.1086/518101)
- Hamaguchi, K., Corcoran, M. F., Russell, C. M. P., et al. 2014, *ApJ*, 784, 125, doi: [10.1088/0004-637X/784/2/125](https://doi.org/10.1088/0004-637X/784/2/125)
- Hillier, D. J., Davidson, K., Ishibashi, K., & Gull, T. 2001, *ApJ*, 553, 837, doi: [10.1086/320948](https://doi.org/10.1086/320948)
- Humphreys, R. M., & Martin, J. C. 2012, in *Astrophysics and Space Science Library, Vol. 384, Eta Carinae and the Supernova Impostors*, ed. K. Davidson & R. M. Humphreys, 1, doi: [10.1007/978-1-4614-2275-4\\_1](https://doi.org/10.1007/978-1-4614-2275-4_1)
- Immler, S., & Kuntz, K. D. 2005, *ApJL*, 632, L99, doi: [10.1086/497910](https://doi.org/10.1086/497910)
- Ishibashi, K., Corcoran, M. F., Davidson, K., et al. 1999, *ApJ*, 524, 983, doi: [10.1086/307859](https://doi.org/10.1086/307859)
- Kashi, A., Principe, D. A., Soker, N., & Kastner, J. H. 2021, *ApJ*, 914, 47, doi: [10.3847/1538-4357/abfa9c](https://doi.org/10.3847/1538-4357/abfa9c)
- Kashi, A., & Soker, N. 2009, *ApJL*, 701, L59, doi: [10.1088/0004-637X/701/1/L59](https://doi.org/10.1088/0004-637X/701/1/L59)
- Kiminki, M. M., Reiter, M., & Smith, N. 2016, *MNRAS*, 463, 845, doi: [10.1093/mnras/stw2019](https://doi.org/10.1093/mnras/stw2019)
- Madura, T. I., Gull, T. R., Owocki, S. P., et al. 2012, *MNRAS*, 420, 2064, doi: [10.1111/j.1365-2966.2011.20165.x](https://doi.org/10.1111/j.1365-2966.2011.20165.x)
- Madura, T. I., Gull, T. R., Okazaki, A. T., et al. 2013, *MNRAS*, 436, 3820, doi: [10.1093/mnras/stt1871](https://doi.org/10.1093/mnras/stt1871)
- Mehner, A., Davidson, K., Ferland, G. J., & Humphreys, R. M. 2010, *ApJ*, 710, 729, doi: [10.1088/0004-637X/710/1/729](https://doi.org/10.1088/0004-637X/710/1/729)
- Moffat, A. F. J., & Corcoran, M. F. 2009, *ApJ*, 707, 693, doi: [10.1088/0004-637X/707/1/693](https://doi.org/10.1088/0004-637X/707/1/693)
- Morris, P. W., Gull, T. R., Hillier, D. J., et al. 2017, *ApJ*, 842, 79, doi: [10.3847/1538-4357/aa71b3](https://doi.org/10.3847/1538-4357/aa71b3)
- Okazaki, A. T., Owocki, S. P., Russell, C. M. P., & Corcoran, M. F. 2008, *MNRAS*, 388, L39, doi: [10.1111/j.1745-3933.2008.00496.x](https://doi.org/10.1111/j.1745-3933.2008.00496.x)
- Owocki, S. P., Castor, J. I., & Rybicki, G. B. 1988, *ApJ*, 335, 914, doi: [10.1086/166977](https://doi.org/10.1086/166977)
- Parkin, E. R., Pittard, J. M., Corcoran, M. F., & Hamaguchi, K. 2011, *ApJ*, 726, 105, doi: [10.1088/0004-637X/726/2/105](https://doi.org/10.1088/0004-637X/726/2/105)
- Parkin, E. R., Pittard, J. M., Corcoran, M. F., Hamaguchi, K., & Stevens, I. R. 2009, *MNRAS*, 394, 1758, doi: [10.1111/j.1365-2966.2009.14475.x](https://doi.org/10.1111/j.1365-2966.2009.14475.x)
- Pittard, J. M., & Corcoran, M. F. 2002, *A&A*, 383, 636, doi: [10.1051/0004-6361:20020025](https://doi.org/10.1051/0004-6361:20020025)
- Prigozhin, G., Gendreau, K., Doty, J. P., et al. 2016, in *Proc. SPIE, Vol. 9905, Space Telescopes and Instrumentation 2016: Ultraviolet to Gamma Ray*, 99051I, doi: [10.1117/12.2231718](https://doi.org/10.1117/12.2231718)
- Remillard, R. A., Loewenstein, M., Steiner, J. F., et al. 2021, *arXiv e-prints*, arXiv:2105.09901. <https://arxiv.org/abs/2105.09901>
- Russell, C. M. P., Corcoran, M. F., Hamaguchi, K., et al. 2016, *MNRAS*, 458, 2275, doi: [10.1093/mnras/stw339](https://doi.org/10.1093/mnras/stw339)
- Seward, F. D., Forman, W. R., Giacconi, R., et al. 1979, *ApJL*, 234, L55, doi: [10.1086/183108](https://doi.org/10.1086/183108)
- Smith, N. 2006, *ApJ*, 644, 1151, doi: [10.1086/503766](https://doi.org/10.1086/503766)
- Stellingwerf, R. F. 1978, *ApJ*, 224, 953, doi: [10.1086/156444](https://doi.org/10.1086/156444)
- Stevens, I. R., Blondin, J. M., & Pollock, A. M. T. 1992, *ApJ*, 386, 265, doi: [10.1086/171013](https://doi.org/10.1086/171013)
- Teodoro, M., Damineli, A., Heathcote, B., et al. 2016, *ApJ*, 819, 131, doi: [10.3847/0004-637X/819/2/131](https://doi.org/10.3847/0004-637X/819/2/131)
- Usov, V. V. 1992, *ApJ*, 389, 635, doi: [10.1086/171236](https://doi.org/10.1086/171236)
- Verner, E., Bruhweiler, F., & Gull, T. 2005, *ApJ*, 624, 973, doi: [10.1086/429400](https://doi.org/10.1086/429400)
- Weis, K., Corcoran, M. F., Bomans, D. J., & Davidson, K. 2004, *A&A*, 415, 595, doi: [10.1051/0004-6361:20034306](https://doi.org/10.1051/0004-6361:20034306)



Wilms, J., Allen, A., & McCray, R. 2000, ApJ, 542, 914,  
doi: [10.1086/317016](https://doi.org/10.1086/317016)

## APPENDIX

Table 6. Log of *NICER* Observations and Rates

OBSID	MJD Start	MJD End	Phase	EXPOSURE	2.0 – 10.0 keV		2.0 – 3.0 keV		5.0 – 7.0 keV	
					Total	Net	Total	Net	Total	Net
					s	cts/s	cts/s	cts/s	cts/s	cts/s
1110010101	57954.1245	57954.9641	3.5343	299.7	6.09	5.55 ± 0.14	2.66	2.54 ± 0.09	0.71	0.60 ± 0.05
1110010102	57955.0252	57955.9950	3.5347	677.0	6.69	5.83 ± 0.10	2.83	2.67 ± 0.06	0.83	0.64 ± 0.04
1110010103	57956.1829	57956.8311	3.5352	636.5	6.59	4.94 ± 0.10	2.82	2.54 ± 0.07	0.82	0.44 ± 0.04
1110010105	57958.4340	57958.6970	3.5362	392.9	6.51	5.39 ± 0.13	2.70	2.48 ± 0.08	0.81	0.55 ± 0.05
1110010106	58031.0912	58031.8693	3.5723	297.1	7.07	3.47 ± 0.15	3.15	2.63 ± 0.10	0.85	< 0.05
1110010107	58032.2539	58032.2613	3.5727	199.5	9.73	6.33 ± 0.22	3.45	2.93 ± 0.13	1.44	0.62 ± 0.09
1110010108	58078.2795	58078.3071	3.5954	694.8	6.79	4.92 ± 0.10	2.87	2.56 ± 0.06	0.85	0.42 ± 0.04
1110010109	58099.2565	58099.3248	3.6058	163.3	6.74	5.40 ± 0.20	2.99	2.73 ± 0.14	0.80	0.49 ± 0.07
1110010110	58109.0289	58109.8907	3.6108	1946.4	6.77	6.39 ± 0.06	3.05	2.97 ± 0.04	0.73	0.65 ± 0.02
1110010111	58117.0138	58117.0233	3.6146	141.7	6.87	6.37 ± 0.22	2.86	2.75 ± 0.14	0.87	0.77 ± 0.08
1110010112	58119.2025	58119.3339	3.6157	169.5	7.74	6.84 ± 0.21	3.38	3.19 ± 0.14	0.86	0.66 ± 0.07
1110010114	58136.8688	58136.8737	3.6244	352.3	7.04	6.45 ± 0.14	3.11	2.98 ± 0.09	0.67	0.54 ± 0.04
1110010115	58137.1882	58137.3885	3.6246	349.6	7.21	5.57 ± 0.14	3.25	2.98 ± 0.10	0.88	0.50 ± 0.05
1110010116	58141.4193	58141.8340	3.6267	3724.3	6.92	6.58 ± 0.04	3.22	3.14 ± 0.03	0.74	0.66 ± 0.01
1110010117	58147.7198	58147.7935	3.6298	208.4	6.62	6.32 ± 0.18	3.01	2.94 ± 0.12	0.69	0.62 ± 0.06
1110010119	58168.5028	58168.5082	3.6400	365.9	8.87	7.99 ± 0.16	3.59	3.40 ± 0.10	1.21	1.01 ± 0.06
1110010120	58169.6597	58169.9231	3.6407	567.3	7.57	6.56 ± 0.12	3.44	3.23 ± 0.08	0.82	0.60 ± 0.04
1110010121	58173.2584	58173.9097	3.6425	331.6	7.61	6.80 ± 0.15	3.26	3.09 ± 0.10	0.93	0.75 ± 0.05
1110010122	58174.0347	58174.3576	3.6429	242.8	7.28	4.90 ± 0.17	3.27	2.92 ± 0.12	0.75	0.19 ± 0.06
1110010123	58175.1285	58175.9722	3.6435	365.7	7.61	6.18 ± 0.14	3.31	3.04 ± 0.10	0.82	0.49 ± 0.05
1110010125	58177.8463	58177.9621	3.6447	522.9	7.11	5.38 ± 0.12	3.25	2.98 ± 0.08	0.74	0.33 ± 0.04
1110010126	58178.4093	58178.9913	3.6451	314.5	8.37	6.59 ± 0.16	3.68	3.35 ± 0.11	1.03	0.62 ± 0.06
1110010127	58179.9521	58179.9563	3.6457	249.8	9.06	6.60 ± 0.19	3.65	3.28 ± 0.12	1.32	0.74 ± 0.07
1110010128	58184.0039	58184.3500	3.6478	643.5	6.93	5.68 ± 0.10	3.12	2.88 ± 0.07	0.80	0.52 ± 0.04
1110010129	58187.1653	58187.2347	3.6493	458.8	7.93	6.96 ± 0.13	3.40	3.20 ± 0.09	0.96	0.75 ± 0.05
1110010131	58199.5606	58199.7051	3.6554	413.9	10.92	5.05 ± 0.16	3.66	2.90 ± 0.09	1.76	0.35 ± 0.07
1110010132	58216.6053	58216.6153	3.6638	276.6	7.12	4.40 ± 0.16	3.00	2.58 ± 0.10	0.86	0.22 ± 0.06
1110010133	58222.1339	58222.4620	3.6666	511.7	7.75	4.85 ± 0.12	3.06	2.62 ± 0.08	0.99	0.31 ± 0.04
1110010134	58223.2259	58223.8129	3.6672	297.0	9.91	5.91 ± 0.18	3.31	2.77 ± 0.11	1.59	0.62 ± 0.07
1110010136	58228.3578	58228.9481	3.6698	616.0	9.83	8.31 ± 0.13	3.40	3.12 ± 0.07	1.50	1.14 ± 0.05
1110010141	58239.0352	58239.8833	3.6751	5795.4	6.86	6.47 ± 0.03	3.07	2.98 ± 0.02	0.78	0.70 ± 0.01
1110010142	58241.3518	58241.6838	3.6761	1102.0	6.75	6.04 ± 0.08	2.99	2.84 ± 0.05	0.79	0.64 ± 0.03
1110010143	58242.3166	58242.3278	3.6765	170.6	7.02	6.66 ± 0.20	3.02	2.93 ± 0.13	0.80	0.73 ± 0.07
1110010146	58252.7644	58252.9610	3.6817	616.3	6.72	6.35 ± 0.10	2.96	2.88 ± 0.07	0.84	0.76 ± 0.04
1110010147	58253.0192	58253.2182	3.6819	1051.8	6.78	6.39 ± 0.08	3.03	2.94 ± 0.05	0.75	0.67 ± 0.03
1110010148	58259.4911	58259.5076	3.6850	516.0	7.25	3.26 ± 0.12	3.02	2.46 ± 0.08	0.92	< 0.04
1110010149	58262.9049	58262.9273	3.6867	500.7	6.90	6.12 ± 0.12	2.92	2.75 ± 0.08	0.83	0.67 ± 0.04
1110010150	58263.0956	58263.6347	3.6869	1773.3	6.78	4.92 ± 0.06	2.94	2.68 ± 0.04	0.81	0.37 ± 0.02
1110010151	58275.6873	58275.8257	3.6931	469.0	8.83	7.25 ± 0.14	3.34	3.07 ± 0.08	1.30	0.94 ± 0.05
1110010152	58283.5262	58283.7279	3.6970	939.0	6.64	6.38 ± 0.08	2.82	2.76 ± 0.05	0.79	0.73 ± 0.03
1110010153	58289.1243	58289.1412	3.6997	581.6	6.53	4.37 ± 0.11	2.76	2.46 ± 0.07	0.78	0.26 ± 0.04
1110010155	58298.3313	58298.3481	3.7042	752.8	6.96	5.44 ± 0.10	2.87	2.59 ± 0.06	0.88	0.52 ± 0.03
1110010156	58301.1650	58301.2340	3.7056	480.1	6.78	3.26 ± 0.12	2.73	2.24 ± 0.08	0.88	0.04 ± 0.04
1110010157	58308.2235	58308.3012	3.7091	1733.4	6.37	5.98 ± 0.06	2.78	2.69 ± 0.04	0.75	0.67 ± 0.02

Table 6 continued on next page

Table 6 (continued)

OBSID	MJD Start	MJD End	Phase	EXPOSURE	2.0 – 10.0 keV		2.0 – 3.0 keV		5.0 – 7.0 keV	
					Total	Net	Total	Net	Total	Net
					s	cts/s	cts/s	cts/s	cts/s	cts/s
1110010158	58314.6586	58314.7329	3.7123	594.7	6.79	4.57 ± 0.11	2.78	2.43 ± 0.07	0.89	0.36 ± 0.04
1110010159	58319.8752	58319.8772	3.7149	109.3	6.98	6.23 ± 0.25	2.77	2.60 ± 0.16	0.74	0.58 ± 0.08
1110010160	58320.0683	58320.2634	3.7150	247.1	8.26	6.15 ± 0.18	3.01	2.68 ± 0.11	1.16	0.67 ± 0.07
1110010161	58321.7405	58321.7432	3.7158	175.2	6.19	5.61 ± 0.19	2.53	2.41 ± 0.12	0.78	0.66 ± 0.07
1110010163	58323.5979	58323.6764	3.7167	1048.4	6.92	5.58 ± 0.08	2.92	2.69 ± 0.05	0.84	0.53 ± 0.03
1110010164	58327.0116	58327.1006	3.7184	2275.8	6.46	5.93 ± 0.05	2.84	2.72 ± 0.04	0.75	0.63 ± 0.02
1110010165	58331.0049	58331.9109	3.7206	268.2	6.27	5.23 ± 0.15	2.80	2.59 ± 0.10	0.68	0.45 ± 0.05
1110010169	58342.8951	58342.9643	3.7263	196.0	10.32	7.07 ± 0.23	3.60	3.13 ± 0.14	1.61	0.84 ± 0.09
1110010171	58351.8975	58351.9743	3.7307	359.8	13.76	1.67 ± 0.20	4.06	2.63 ± 0.11	2.36	< 0.08
1110010173	58362.9475	58362.9634	3.7362	974.1	7.35	6.75 ± 0.09	3.38	3.26 ± 0.06	0.79	0.65 ± 0.03
1110010174	58363.0118	58363.0294	3.7362	1052.0	7.44	7.10 ± 0.08	3.39	3.31 ± 0.06	0.77	0.70 ± 0.03
1110010175	58368.4795	58368.5051	3.7389	292.7	7.27	6.77 ± 0.16	3.27	3.15 ± 0.11	0.82	0.72 ± 0.05
1110010176	58375.4289	58375.6970	3.7424	782.3	8.19	7.50 ± 0.10	3.62	3.46 ± 0.07	0.91	0.76 ± 0.03
1110010179	58417.2524	58417.3912	3.7631	1387.3	10.37	7.49 ± 0.09	4.15	3.72 ± 0.05	1.40	0.72 ± 0.03
1110010185	58452.0986	58452.1674	3.7803	162.9	8.57	8.11 ± 0.23	3.81	3.71 ± 0.15	1.08	0.98 ± 0.08
1110010186	58455.3905	58455.4660	3.7819	244.1	8.42	7.55 ± 0.19	3.72	3.54 ± 0.12	1.00	0.80 ± 0.06
1110010187	58458.5218	58458.5368	3.7834	431.0	0.25	< 0.02	0.05	< 0.01	0.05	< 0.01
1110010188	58469.7851	58469.8005	3.7890	385.4	8.64	7.04 ± 0.15	3.81	3.56 ± 0.10	1.01	0.64 ± 0.05
1110010189	58470.4912	58470.6377	3.7894	1667.6	8.96	7.95 ± 0.07	3.97	3.79 ± 0.05	1.00	0.78 ± 0.02
1110010190	58477.1783	58477.2631	3.7927	1316.8	9.34	7.40 ± 0.08	3.93	3.62 ± 0.05	1.18	0.73 ± 0.03
1110010193	58493.5105	58493.8428	3.8008	294.9	9.40	7.33 ± 0.18	4.10	3.78 ± 0.12	1.09	0.60 ± 0.06
1110010194	58494.9213	58494.9373	3.8014	608.1	10.05	8.56 ± 0.13	4.45	4.19 ± 0.09	1.12	0.78 ± 0.04
1110010195	58495.3067	58495.3236	3.8016	518.8	10.41	9.04 ± 0.14	4.61	4.35 ± 0.09	1.20	0.89 ± 0.05
1110010196	58496.3350	58496.3537	3.8021	505.6	12.65	8.54 ± 0.16	4.77	4.19 ± 0.10	1.75	0.77 ± 0.06
1110010197	58497.2387	58497.2565	3.8026	581.5	10.46	9.15 ± 0.13	4.62	4.36 ± 0.09	1.30	1.00 ± 0.05
1110010198	58498.0725	58498.1515	3.8030	1015.7	10.44	9.13 ± 0.10	4.55	4.30 ± 0.07	1.22	0.93 ± 0.03
1110010199	58499.5523	58499.6398	3.8037	116.1	10.63	4.88 ± 0.30	4.49	3.74 ± 0.20	1.30	< 0.11
1110010201	58500.5252	58500.6690	3.8042	168.7	10.74	3.67 ± 0.25	4.68	3.81 ± 0.17	1.34	< 0.09
1110010202	58501.8114	58501.8176	3.8048	420.6	10.30	8.96 ± 0.16	4.52	4.28 ± 0.10	1.14	0.84 ± 0.05
1110010203	58502.2592	58502.5343	3.8051	507.0	10.64	7.94 ± 0.15	4.56	4.15 ± 0.09	1.29	0.65 ± 0.05
1110010204	58520.2005	58520.7284	3.8140	1007.0	9.51	9.10 ± 0.10	4.46	4.37 ± 0.07	1.02	0.93 ± 0.03
1110010205	58525.4805	58525.4935	3.8165	980.7	9.12	8.72 ± 0.10	4.34	4.25 ± 0.07	0.93	0.84 ± 0.03
1110010206	58530.3733	58530.4488	3.8190	773.0	9.48	9.15 ± 0.11	4.46	4.38 ± 0.08	0.92	0.85 ± 0.03
1110010207	58533.7206	58533.7326	3.8206	516.8	10.20	8.94 ± 0.14	4.65	4.39 ± 0.09	1.16	0.88 ± 0.05
1110010208	58537.0664	58537.1440	3.8223	1657.9	10.45	8.91 ± 0.08	4.65	4.39 ± 0.05	1.20	0.84 ± 0.03
2110010201	58547.5717	58547.9738	3.8275	2430.5	9.98	9.55 ± 0.06	4.51	4.42 ± 0.04	1.14	1.05 ± 0.02
2110010202	58548.0231	58548.9396	3.8279	9945.4	10.29	9.69 ± 0.03	4.61	4.48 ± 0.02	1.18	1.05 ± 0.01
2110010203	58549.1162	58549.1329	3.8282	460.5	10.16	8.28 ± 0.15	4.56	4.26 ± 0.10	1.16	0.72 ± 0.05
2612010101	58556.7181	58556.7289	3.8320	400.0	10.30	10.02 ± 0.16	4.63	4.56 ± 0.11	1.16	1.10 ± 0.05
2612010401	58575.6100	58575.6262	3.8413	1058.5	10.01	9.61 ± 0.10	4.29	4.20 ± 0.06	1.26	1.17 ± 0.03
2612010501	58582.3762	58582.3956	3.8447	704.6	10.64	7.00 ± 0.12	4.37	3.88 ± 0.08	1.41	0.54 ± 0.05
2612010601	58589.0624	58589.0924	3.8480	1145.5	10.36	9.24 ± 0.10	4.32	4.11 ± 0.06	1.34	1.09 ± 0.03
2612010701	58596.2097	58596.2852	3.8515	1037.5	9.85	9.53 ± 0.10	4.32	4.24 ± 0.06	1.17	1.10 ± 0.03
2612010801	58602.9717	58602.9838	3.8548	627.0	10.55	9.40 ± 0.13	4.56	4.33 ± 0.09	1.31	1.05 ± 0.05
2612010802	58603.0360	58603.0481	3.8549	599.4	10.26	9.59 ± 0.13	4.34	4.20 ± 0.09	1.29	1.14 ± 0.05
2612010901	58610.9071	58610.9231	3.8588	459.1	9.90	9.48 ± 0.15	4.33	4.24 ± 0.10	1.24	1.15 ± 0.05
2612011001	58617.0283	58617.1039	3.8618	1128.1	10.34	9.78 ± 0.10	4.38	4.25 ± 0.06	1.32	1.20 ± 0.03
2612011101	58624.2824	58624.3093	3.8654	872.3	10.06	7.41 ± 0.11	4.32	3.90 ± 0.07	1.27	0.65 ± 0.04
2612011201	58630.9266	58630.9417	3.8687	255.5	10.28	9.54 ± 0.20	4.26	4.12 ± 0.13	1.31	1.15 ± 0.07
2612011202	58630.9909	58631.0060	3.8687	210.6	10.55	10.15 ± 0.22	4.36	4.27 ± 0.14	1.26	1.17 ± 0.08
2612011301	58637.9304	58637.9417	3.8721	383.4	10.33	7.37 ± 0.16	4.39	3.97 ± 0.11	1.37	0.67 ± 0.06

Table 6 continued on next page

Table 6 (continued)

OBSID	MJD Start	MJD End	Phase	EXPOSURE	2.0 – 10.0 keV		2.0 – 3.0 keV		5.0 – 7.0 keV	
					Total	Net	Total	Net	Total	Net
					s	cts/s	cts/s	cts/s	cts/s	cts/s
2612011401	58645.5280	58645.5381	3.8759	436.7	9.93	9.45 ± 0.15	4.12	4.02 ± 0.10	1.29	1.19 ± 0.05
2612011402	58646.0417	58646.0544	3.8761	335.8	10.00	9.68 ± 0.17	4.21	4.14 ± 0.11	1.30	1.23 ± 0.06
2612011501	58652.4240	58652.4424	3.8793	1351.5	10.04	9.32 ± 0.09	4.18	4.04 ± 0.06	1.28	1.12 ± 0.03
2612011601	58657.9089	58657.9252	3.8820	797.1	11.05	9.29 ± 0.12	4.58	4.25 ± 0.08	1.44	1.04 ± 0.04
2612011701	58663.0030	58663.0188	3.8845	256.9	11.25	9.73 ± 0.21	4.72	4.46 ± 0.14	1.42	1.07 ± 0.07
2612011801	58676.2015	58676.3370	3.8911	997.1	11.53	10.75 ± 0.11	4.82	4.66 ± 0.07	1.49	1.31 ± 0.04
2612011901	58680.1998	58680.2863	3.8930	1423.1	11.46	10.27 ± 0.09	4.83	4.61 ± 0.06	1.43	1.16 ± 0.03
2612012001	58687.2852	58687.3171	3.8965	1007.7	12.34	11.84 ± 0.11	5.14	5.03 ± 0.07	1.58	1.47 ± 0.04
2612012101	58693.0936	58693.1169	3.8994	1355.3	12.60	12.24 ± 0.10	5.21	5.13 ± 0.06	1.61	1.53 ± 0.03
2612012401	58716.2225	58716.2961	3.9108	277.6	12.89	11.32 ± 0.22	5.38	5.11 ± 0.14	1.75	1.39 ± 0.08
2612012501	58721.3835	58721.4593	3.9134	484.2	15.69	14.44 ± 0.18	6.52	6.28 ± 0.12	2.01	1.73 ± 0.06
2612012502	58722.5889	58722.6042	3.9140	307.1	15.34	14.79 ± 0.22	6.40	6.28 ± 0.14	2.06	1.94 ± 0.08
2612012601	58729.5560	58729.5725	3.9174	125.0	14.06	13.03 ± 0.34	5.83	5.61 ± 0.22	1.93	1.70 ± 0.12
2612012701	58736.0142	58736.0752	3.9206	187.8	14.50	13.83 ± 0.28	5.85	5.69 ± 0.18	1.93	1.79 ± 0.10
2612012901	58750.8275	58750.8435	3.9279	375.8	14.81	14.16 ± 0.20	6.12	5.97 ± 0.13	2.07	1.93 ± 0.07
2612020301	58790.5337	58790.5581	3.9476	137.9	16.45	15.36 ± 0.35	6.28	6.05 ± 0.21	2.39	2.15 ± 0.13
2612020401	58793.6933	58793.7199	3.9491	184.5	16.21	15.51 ± 0.30	6.37	6.22 ± 0.19	2.28	2.13 ± 0.11
2612020501	58795.0450	58795.0728	3.9498	172.4	16.90	16.45 ± 0.31	6.71	6.61 ± 0.20	2.28	2.18 ± 0.12
2612020701	58800.0102	58800.0294	3.9523	172.6	16.37	15.86 ± 0.31	6.62	6.51 ± 0.20	2.23	2.12 ± 0.11
2612020801	58802.0076	58802.0271	3.9532	323.5	17.68	17.24 ± 0.23	7.10	7.00 ± 0.15	2.44	2.34 ± 0.09
2612020901	58804.0078	58804.0278	3.9542	261.0	19.16	18.77 ± 0.27	7.49	7.40 ± 0.17	2.79	2.70 ± 0.10
2612021001	58807.0372	58807.0530	3.9557	131.0	19.94	19.37 ± 0.39	7.67	7.54 ± 0.24	2.66	2.55 ± 0.14
2612021101	58809.1014	58809.1162	3.9567	426.8	21.18	20.53 ± 0.22	8.53	8.38 ± 0.14	2.91	2.77 ± 0.08
2612021102	58810.2620	58810.2770	3.9573	254.8	22.67	22.13 ± 0.30	8.83	8.70 ± 0.19	3.21	3.09 ± 0.11
2612021201	58811.4230	58811.5668	3.9579	1708.2	22.81	22.45 ± 0.12	9.07	8.99 ± 0.07	3.15	3.07 ± 0.04
2612021202	58812.6484	58812.6634	3.9585	445.1	22.96	22.63 ± 0.23	9.20	9.13 ± 0.14	3.15	3.08 ± 0.08
2612021301	58813.8748	58813.9532	3.9591	956.7	23.53	23.14 ± 0.16	9.48	9.39 ± 0.10	3.23	3.15 ± 0.06
2612021801	58825.3557	58825.4965	3.9648	2220.5	21.98	21.52 ± 0.10	8.45	8.35 ± 0.06	3.27	3.17 ± 0.04
2612021901	58826.3288	58826.3949	3.9653	751.8	21.91	21.16 ± 0.17	8.44	8.29 ± 0.11	3.30	3.13 ± 0.07
2612022003	58829.0544	58829.9404	3.9668	594.8	22.23	21.49 ± 0.19	8.64	8.48 ± 0.12	3.28	3.12 ± 0.07
2612022102	58830.1914	58830.1999	3.9672	295.0	21.52	20.56 ± 0.27	8.12	7.94 ± 0.17	3.37	3.15 ± 0.11
2612022103	58832.7098	58832.9795	3.9685	779.0	22.91	21.41 ± 0.17	8.54	8.26 ± 0.10	3.38	3.04 ± 0.07
2612022104	58833.5626	58833.9589	3.9689	2506.0	23.19	22.81 ± 0.10	8.89	8.80 ± 0.06	3.46	3.38 ± 0.04
2612022105	58834.0846	58834.9938	3.9693	5058.4	23.70	23.13 ± 0.07	9.19	9.08 ± 0.04	3.46	3.33 ± 0.03
2612022201	58835.0368	58835.9627	3.9698	5613.2	24.78	24.06 ± 0.07	9.45	9.31 ± 0.04	3.70	3.54 ± 0.03
2612022202	58836.0743	58836.7366	3.9702	2207.3	24.66	24.01 ± 0.11	9.40	9.27 ± 0.07	3.68	3.54 ± 0.04
2612022301	58837.1103	58837.5748	3.9707	1618.0	24.07	23.69 ± 0.12	9.20	9.12 ± 0.08	3.58	3.50 ± 0.05
2612022302	58837.9976	58838.8468	3.9712	1212.4	25.06	23.83 ± 0.14	9.31	9.07 ± 0.09	3.73	3.46 ± 0.06
2612022401	58839.2858	58839.8193	3.9718	1514.2	24.55	23.39 ± 0.13	9.38	9.14 ± 0.08	3.71	3.46 ± 0.05
2612022402	58840.1899	58840.6639	3.9722	1843.7	23.77	22.90 ± 0.11	9.16	8.99 ± 0.07	3.49	3.29 ± 0.04
2612022403	58841.1019	58841.6312	3.9727	1363.0	23.13	22.68 ± 0.13	8.99	8.89 ± 0.08	3.30	3.20 ± 0.05
2612022501	58842.0653	58842.9859	3.9733	2007.0	23.41	22.91 ± 0.11	9.00	8.89 ± 0.07	3.45	3.35 ± 0.04
2612022502	58843.4863	58843.9532	3.9739	1577.2	23.81	23.36 ± 0.12	9.03	8.94 ± 0.08	3.50	3.41 ± 0.05
2612022601	58844.3926	58844.9211	3.9743	3449.9	24.10	23.58 ± 0.08	8.99	8.88 ± 0.05	3.65	3.54 ± 0.03
2612022602	58845.0414	58845.5019	3.9746	1664.8	24.27	23.70 ± 0.12	9.06	8.94 ± 0.07	3.68	3.55 ± 0.05
2612022701	58846.0058	58846.7921	3.9752	2097.4	25.20	24.83 ± 0.11	9.42	9.34 ± 0.07	3.79	3.71 ± 0.04
2612022702	58847.2324	58847.2438	3.9756	558.7	25.44	24.44 ± 0.21	9.20	9.03 ± 0.13	3.99	3.76 ± 0.08
2612022703	58848.5930	58848.6634	3.9763	294.1	25.28	25.02 ± 0.29	9.33	9.27 ± 0.18	4.22	4.16 ± 0.12
2612023002	58854.7581	58854.8317	3.9793	206.8	32.42	31.87 ± 0.40	12.95	12.83 ± 0.25	4.24	4.12 ± 0.14
2612023003	58855.5311	58855.9255	3.9798	757.6	30.33	29.79 ± 0.20	13.07	12.96 ± 0.13	3.71	3.60 ± 0.07
2612023101	58856.1770	58856.9623	3.9802	3933.6	27.89	27.12 ± 0.08	12.15	12.01 ± 0.06	3.27	3.10 ± 0.03

Table 6 continued on next page

Table 6 (continued)

OBSID	MJD Start	MJD End	Phase	EXPOSURE	2.0 – 10.0 keV		2.0 – 3.0 keV		5.0 – 7.0 keV	
					Total	Net	Total	Net	Total	Net
					s	cts/s	cts/s	cts/s	cts/s	cts/s
2612023102	58857.0787	58857.9306	3.9807	4910.0	25.08	24.28 ± 0.07	10.96	10.80 ± 0.05	2.95	2.77 ± 0.02
2612023201	58858.1715	58858.9540	3.9812	3883.0	26.05	25.22 ± 0.08	11.11	10.94 ± 0.05	3.18	2.99 ± 0.03
2612023202	58859.0121	58859.9965	3.9817	2394.8	25.01	24.41 ± 0.10	10.48	10.35 ± 0.07	3.20	3.07 ± 0.04
2612023301	58860.0445	58860.7725	3.9821	2505.0	22.53	21.51 ± 0.09	9.29	9.09 ± 0.06	2.98	2.75 ± 0.03
2612023302	58861.0099	58862.0000	3.9826	3590.7	18.80	18.01 ± 0.07	7.73	7.58 ± 0.05	2.51	2.34 ± 0.03
2612023303	58861.9798	58862.8391	3.9831	6087.6	17.04	16.09 ± 0.05	6.89	6.70 ± 0.03	2.36	2.14 ± 0.02
2612023401	58863.0136	58864.0000	3.9836	5149.8	15.75	14.72 ± 0.06	6.06	5.86 ± 0.03	2.34	2.11 ± 0.02
2612023402	58863.9819	58864.9674	3.9841	5609.8	16.01	14.98 ± 0.05	6.11	5.91 ± 0.03	2.43	2.20 ± 0.02
2612023501	58865.0796	58865.9991	3.9846	4638.6	16.64	15.40 ± 0.06	6.28	6.05 ± 0.04	2.55	2.27 ± 0.02
2612023502	58866.1114	58866.9021	3.9851	3088.1	17.96	16.86 ± 0.08	6.64	6.43 ± 0.05	2.77	2.52 ± 0.03
2612023601	58867.0169	58867.9340	3.9856	2160.0	22.21	21.13 ± 0.10	8.09	7.87 ± 0.06	3.44	3.20 ± 0.04
2612023602	58868.0532	58868.9662	3.9861	2136.0	25.44	24.14 ± 0.11	9.40	9.15 ± 0.07	3.76	3.47 ± 0.04
2612023701	58869.0926	58869.0951	3.9864	155.7	24.14	23.76 ± 0.39	9.29	9.20 ± 0.24	3.33	3.25 ± 0.15
2612023702	58871.5791	58871.7873	3.9877	3453.0	13.71	13.33 ± 0.06	5.38	5.29 ± 0.04	1.99	1.91 ± 0.02
2612023801	58873.3860	58873.3998	3.9885	1024.6	19.96	19.28 ± 0.14	7.32	7.17 ± 0.08	3.14	2.99 ± 0.06
2612023902	58875.1947	58875.9146	3.9896	7996.2	7.92	7.55 ± 0.03	3.19	3.11 ± 0.02	1.15	1.07 ± 0.01
2612023903	58876.1678	58876.8768	3.9901	3430.3	7.82	7.48 ± 0.05	2.85	2.78 ± 0.03	1.32	1.24 ± 0.02
2612024001	58877.1942	58877.7828	3.9906	3294.1	7.31	6.90 ± 0.05	2.61	2.51 ± 0.03	1.31	1.23 ± 0.02
2612024002	58878.0315	58878.6894	3.9910	3273.5	8.37	7.91 ± 0.05	2.65	2.55 ± 0.03	1.61	1.52 ± 0.02
2612024101	58879.3874	58879.8468	3.9916	2977.0	6.80	6.36 ± 0.05	2.38	2.28 ± 0.03	1.20	1.11 ± 0.02
2612024102	58880.3555	58880.6928	3.9921	3923.6	7.94	7.35 ± 0.04	2.45	2.33 ± 0.02	1.59	1.46 ± 0.02
2612024201	58881.0009	58881.6606	3.9925	2965.1	9.15	8.64 ± 0.06	2.46	2.35 ± 0.03	2.13	2.02 ± 0.03
2612024202	58882.0326	58882.6844	3.9930	2005.6	8.79	8.45 ± 0.07	2.34	2.26 ± 0.03	1.98	1.91 ± 0.03
2612024203	58883.0014	58883.7255	3.9935	2799.5	4.71	4.11 ± 0.04	1.64	1.51 ± 0.02	0.85	0.72 ± 0.02
2612024301	58884.0341	58884.8225	3.9940	2396.9	2.77	2.35 ± 0.03	1.13	1.03 ± 0.02	0.44	0.35 ± 0.01
2612024302	58885.1958	58885.7257	3.9945	1019.0	2.40	1.74 ± 0.05	1.02	0.88 ± 0.03	0.39	0.25 ± 0.02
2612024401	58886.1641	58886.6937	3.9950	2063.9	2.36	1.83 ± 0.03	0.95	0.84 ± 0.02	0.42	0.30 ± 0.01
2612024402	58887.2009	58887.9845	3.9955	2232.9	1.74	0.75 ± 0.03	0.71	0.53 ± 0.02	0.28	0.05 ± 0.01
2612024501	58888.1667	58888.8880	3.9960	5279.9	1.28	0.57 ± 0.02	0.58	0.44 ± 0.01	0.18	0.02 ± 0.01
2612024502	58889.2662	58889.7914	3.9965	2560.0	1.19	0.51 ± 0.02	0.53	0.40 ± 0.01	0.17	0.02 ± 0.01
2612024601	58891.0744	58891.2757	3.9973	1283.8	1.18	0.06 ± 0.03	0.47	0.27 ± 0.02	0.19	< 0.01
2612024602	58892.0451	58892.2438	3.9978	283.9	1.29	< 0.07	0.59	0.32 ± 0.05	0.21	< 0.03
2612024701	58893.1359	58893.9863	3.9985	3916.0	1.07	0.30 ± 0.02	0.47	0.32 ± 0.01	0.15	< 0.01
2612024702	58894.0379	58894.9544	3.9990	7101.6	1.34	0.60 ± 0.01	0.51	0.36 ± 0.01	0.23	0.06 ± 0.01
2612024801	58895.2003	58895.9225	3.9995	3254.0	1.25	0.44 ± 0.02	0.50	0.33 ± 0.01	0.19	0.01 ± 0.01
2612024802	58896.0400	58896.8905	3.9999	1525.8	0.99	0.12 ± 0.03	0.41	0.23 ± 0.02	0.15	< 0.01
2612024803	58897.1371	58897.7942	4.0004	282.3	1.04	< 0.06	0.52	0.22 ± 0.04	0.11	< 0.02
2612024901	58898.5569	58898.9558	4.0011	112.4	1.93	0.55 ± 0.13	0.60	0.34 ± 0.07	0.34	0.03 ± 0.05
2612024902	58899.0053	58899.9241	4.0014	2883.9	1.53	0.55 ± 0.02	0.55	0.36 ± 0.01	0.28	0.06 ± 0.01
2612025001	58900.1019	58900.8921	4.0019	2283.0	2.11	1.04 ± 0.03	0.63	0.41 ± 0.02	0.41	0.17 ± 0.01
2612025002	58901.1381	58901.9248	4.0024	1959.0	1.91	0.93 ± 0.03	0.63	0.42 ± 0.02	0.35	0.13 ± 0.01
2612025101	58902.1053	58902.9576	4.0029	2788.0	1.34	0.49 ± 0.02	0.45	0.28 ± 0.01	0.24	0.05 ± 0.01
2612025102	58903.1390	58903.7326	4.0034	1766.2	1.36	0.52 ± 0.03	0.47	0.29 ± 0.02	0.22	0.03 ± 0.01
2612025103	58904.0440	58904.9725	4.0039	1441.3	0.87	< 0.03	0.39	0.17 ± 0.02	0.12	< 0.01
2612025201	58905.4724	58905.4887	4.0044	1185.1	0.76	0.44 ± 0.03	0.36	0.28 ± 0.02	0.11	0.04 ± 0.01
2612025202	58905.9894	58906.5208	4.0048	1677.3	0.85	0.51 ± 0.02	0.40	0.33 ± 0.02	0.12	0.05 ± 0.01
2612025301	58907.0194	58907.5532	4.0053	1632.6	0.87	0.61 ± 0.02	0.39	0.33 ± 0.02	0.12	0.06 ± 0.01
3651010101	58909.1446	58909.1664	4.0062	889.1	1.18	0.28 ± 0.04	0.39	0.22 ± 0.02	0.22	0.02 ± 0.02
3651010301	58911.2796	58911.3602	4.0073	2290.9	0.85	0.49 ± 0.02	0.37	0.29 ± 0.01	0.15	0.07 ± 0.01
3651010501	58913.3458	58913.4252	4.0083	2133.6	0.92	0.69 ± 0.02	0.37	0.32 ± 0.01	0.18	0.13 ± 0.01
3651010601	58914.3821	58914.4576	4.0088	1768.9	1.16	0.79 ± 0.03	0.43	0.35 ± 0.02	0.27	0.19 ± 0.01

Table 6 continued on next page

Table 6 (continued)

OBSID	MJD Start	MJD End	Phase	EXPOSURE	2.0 – 10.0 keV		2.0 – 3.0 keV		5.0 – 7.0 keV	
					Total	Net	Total	Net	Total	Net
					s	cts/s	cts/s	cts/s	cts/s	cts/s
3651010701	58915.2266	58915.2317	4.0092	111.7	0.96	0.73 ± 0.09	0.38	0.32 ± 0.06	0.14	0.09 ± 0.04
3651011201	58920.0419	58920.4350	4.0117	306.0	2.50	0.85 ± 0.09	0.50	0.19 ± 0.04	0.72	0.35 ± 0.05
3651011301	58921.0092	58921.0174	4.0121	464.0	1.84	1.26 ± 0.06	0.48	0.35 ± 0.03	0.57	0.44 ± 0.04
3651011401	58922.3619	58922.4398	4.0128	771.7	2.91	0.64 ± 0.06	0.55	0.16 ± 0.03	0.87	0.34 ± 0.03
3651011501	58923.3950	58923.4743	4.0133	1209.3	2.47	0.96 ± 0.05	0.51	0.20 ± 0.02	0.79	0.45 ± 0.03
3651011601	58924.0403	58924.4435	4.0137	1986.8	3.16	1.78 ± 0.04	0.63	0.37 ± 0.02	0.95	0.64 ± 0.02
3651011701	58925.3936	58925.4125	4.0142	902.0	3.24	1.76 ± 0.06	0.60	0.31 ± 0.03	0.99	0.66 ± 0.03
3651011801	58926.4269	58926.4463	4.0148	793.0	2.71	1.78 ± 0.06	0.52	0.32 ± 0.03	0.87	0.67 ± 0.03
3651011901	58927.3329	58927.4787	4.0152	646.9	3.28	2.26 ± 0.07	0.62	0.42 ± 0.03	1.04	0.81 ± 0.04
3651012001	58928.3694	58928.9609	4.0159	1889.9	3.33	2.34 ± 0.04	0.53	0.34 ± 0.02	1.10	0.88 ± 0.02
3651012101	58929.7262	58929.9278	4.0164	467.4	2.98	2.59 ± 0.08	0.42	0.33 ± 0.03	1.03	0.94 ± 0.05
3651012701	58935.5725	58935.7766	4.0193	810.1	3.73	3.44 ± 0.07	0.52	0.46 ± 0.03	1.21	1.15 ± 0.04
3651012801	58936.2185	58936.2949	4.0196	925.5	3.81	3.59 ± 0.06	0.48	0.43 ± 0.02	1.33	1.28 ± 0.04
3651012901	58937.2523	58937.3938	4.0201	2118.2	4.00	3.67 ± 0.04	0.56	0.48 ± 0.02	1.28	1.21 ± 0.02
3651013001	58938.6072	58938.6859	4.0208	1538.0	4.37	4.06 ± 0.05	0.60	0.53 ± 0.02	1.36	1.29 ± 0.03
3651013101	58939.5112	58939.5868	4.0212	1256.3	5.21	4.66 ± 0.06	0.77	0.64 ± 0.02	1.60	1.48 ± 0.04
3651013201	58940.5455	58940.6201	4.0217	1255.2	4.49	4.23 ± 0.06	0.61	0.55 ± 0.02	1.42	1.36 ± 0.03
3651013301	58941.7729	58941.8472	4.0224	1382.3	5.14	4.67 ± 0.06	0.74	0.63 ± 0.02	1.55	1.45 ± 0.03
3651013401	58942.7402	58942.8160	4.0228	1454.0	5.11	4.59 ± 0.06	0.79	0.67 ± 0.02	1.50	1.39 ± 0.03
3651013501	58943.6447	58943.6648	4.0233	1244.0	4.75	4.12 ± 0.06	0.66	0.53 ± 0.02	1.37	1.24 ± 0.03
3651013601	58944.6164	58944.6366	4.0237	1450.1	5.14	4.39 ± 0.06	0.78	0.63 ± 0.02	1.53	1.36 ± 0.03
3651013701	58945.5833	58945.6046	4.0242	1513.1	5.05	4.41 ± 0.06	0.81	0.68 ± 0.02	1.45	1.31 ± 0.03
3651013801	58946.6181	58946.6377	4.0247	1152.5	5.14	4.45 ± 0.07	0.82	0.68 ± 0.03	1.45	1.29 ± 0.04
3651013901	58947.5933	58947.6058	4.0252	368.5	6.04	4.77 ± 0.13	0.94	0.69 ± 0.05	1.73	1.44 ± 0.07
3651014001	58948.6098	58948.6285	4.0257	981.8	5.66	5.20 ± 0.08	0.96	0.85 ± 0.03	1.56	1.47 ± 0.04
3651014101	58949.5296	58949.6067	4.0262	1439.1	5.67	4.82 ± 0.06	0.92	0.74 ± 0.03	1.53	1.34 ± 0.03
3651014201	58950.5447	58950.5750	4.0267	1224.3	5.99	5.17 ± 0.07	1.06	0.89 ± 0.03	1.55	1.37 ± 0.04
3651014401	58952.1164	58952.8088	4.0276	5773.1	5.76	4.99 ± 0.03	0.99	0.84 ± 0.01	1.54	1.37 ± 0.02
3651014501	58953.0829	58953.6523	4.0281	3055.3	5.96	5.32 ± 0.04	1.07	0.94 ± 0.02	1.53	1.38 ± 0.02
3651014601	58954.0950	58954.1731	4.0284	1960.4	5.98	5.41 ± 0.06	1.06	0.93 ± 0.02	1.58	1.46 ± 0.03
3651014701	58955.0616	58955.1397	4.0289	1688.9	5.81	5.37 ± 0.06	1.03	0.93 ± 0.02	1.51	1.41 ± 0.03
3651014801	58956.1606	58956.2384	4.0295	1914.5	5.75	5.34 ± 0.05	1.02	0.93 ± 0.02	1.54	1.45 ± 0.03
3651014901	58957.1315	58957.2067	4.0299	1678.3	6.12	5.67 ± 0.06	1.15	1.05 ± 0.03	1.54	1.44 ± 0.03
3651015001	58957.7099	58957.8713	4.0303	2274.8	6.13	5.51 ± 0.05	1.16	1.02 ± 0.02	1.55	1.42 ± 0.03
3651015101	58959.1297	58959.2074	4.0309	1725.5	6.10	5.64 ± 0.06	1.17	1.06 ± 0.03	1.47	1.37 ± 0.03
3651020101	58960.2915	58960.3690	4.0315	1838.8	6.21	5.58 ± 0.06	1.21	1.07 ± 0.03	1.53	1.40 ± 0.03
3651020201	58962.2925	58962.3694	4.0325	1887.8	6.26	5.82 ± 0.06	1.27	1.17 ± 0.03	1.50	1.41 ± 0.03
3651020301	58964.8742	58964.9507	4.0338	752.0	6.33	5.33 ± 0.09	1.31	1.12 ± 0.04	1.47	1.24 ± 0.04
3651020401	58966.8713	58966.9512	4.0348	795.6	6.37	5.49 ± 0.09	1.34	1.17 ± 0.04	1.49	1.29 ± 0.04
3651020501	58967.9761	58967.9836	4.0353	392.4	6.71	5.87 ± 0.13	1.48	1.31 ± 0.06	1.54	1.35 ± 0.06
3651020502	58968.0411	58968.1771	4.0354	1151.2	6.78	5.93 ± 0.08	1.49	1.31 ± 0.04	1.56	1.38 ± 0.04
3651020601	58969.7219	58969.9840	4.0362	192.0	6.65	4.73 ± 0.19	1.40	1.03 ± 0.09	1.56	1.12 ± 0.09
3651020602	58970.0447	58970.1778	4.0363	155.7	6.51	5.97 ± 0.20	1.48	1.37 ± 0.10	1.40	1.28 ± 0.09
3651020701	58972.6956	58972.8975	4.0377	633.2	6.38	6.02 ± 0.10	1.47	1.39 ± 0.05	1.39	1.32 ± 0.05
3651020801	58974.1151	58974.1965	4.0383	1282.4	6.81	5.83 ± 0.07	1.58	1.40 ± 0.04	1.54	1.32 ± 0.03
3651020901	58976.0506	58976.1319	4.0393	1707.4	6.45	5.93 ± 0.06	1.51	1.40 ± 0.03	1.42	1.31 ± 0.03
3651021001	58978.0533	58978.1322	4.0403	1755.5	6.56	6.14 ± 0.06	1.62	1.53 ± 0.03	1.38	1.29 ± 0.03
3651021101	58980.3171	58980.4553	4.0414	1372.7	6.53	6.21 ± 0.07	1.62	1.55 ± 0.03	1.37	1.30 ± 0.03
3651021201	58981.9933	58982.1968	4.0423	1856.3	6.61	6.26 ± 0.06	1.74	1.67 ± 0.03	1.33	1.25 ± 0.03
3651021301	58984.2954	58984.3755	4.0434	773.1	6.77	5.60 ± 0.09	1.80	1.56 ± 0.05	1.28	1.02 ± 0.04
3651030101	58986.0354	58986.1236	4.0442	2253.9	6.68	6.27 ± 0.05	1.82	1.73 ± 0.03	1.29	1.21 ± 0.02

Table 6 continued on next page

**Table 6** (*continued*)

OBSID	MJD Start	MJD End	Phase	EXPOSURE	2.0 – 10.0 keV		2.0 – 3.0 keV		5.0 – 7.0 keV	
					Total	Net	Total	Net	Total	Net
					s	cts/s	cts/s	cts/s	cts/s	cts/s
3651030201	58993.1429	58993.2231	4.0477	1974.9	6.77	$6.33 \pm 0.06$	1.91	$1.82 \pm 0.03$	1.26	$1.17 \pm 0.03$
3651030301	59001.6386	59001.7127	4.0519	1364.0	7.18	$6.64 \pm 0.07$	2.17	$2.05 \pm 0.04$	1.27	$1.16 \pm 0.03$
3651030501	59014.5339	59014.5519	4.0583	960.0	7.12	$6.68 \pm 0.09$	2.31	$2.21 \pm 0.05$	1.15	$1.05 \pm 0.03$
3651030601	59021.0581	59021.0757	4.0615	344.0	8.12	$6.10 \pm 0.15$	2.45	$2.11 \pm 0.08$	1.42	$0.94 \pm 0.06$
3651030701	59026.5948	59026.6718	4.0643	963.6	6.80	$6.37 \pm 0.08$	2.24	$2.15 \pm 0.05$	1.10	$1.01 \pm 0.03$
3651030901	59042.5980	59042.6750	4.0722	545.1	7.48	$6.59 \pm 0.12$	2.58	$2.41 \pm 0.07$	1.14	$0.93 \pm 0.05$
3651031001	59049.5060	59049.5801	4.0756	327.1	7.90	$6.64 \pm 0.16$	2.70	$2.44 \pm 0.09$	1.19	$0.91 \pm 0.06$
3651031101	59054.2120	59054.2336	4.0779	1136.5	7.59	$7.04 \pm 0.08$	2.78	$2.66 \pm 0.05$	1.11	$0.99 \pm 0.03$
3651031301	59070.3993	59070.5398	4.0860	1047.9	7.97	$7.18 \pm 0.09$	2.98	$2.82 \pm 0.05$	1.10	$0.92 \pm 0.03$
3651031401	59077.3005	59077.4419	4.0894	1524.5	8.90	$8.05 \pm 0.08$	3.14	$2.96 \pm 0.05$	1.36	$1.17 \pm 0.03$
3651031501	59088.3202	59088.3984	4.0948	468.8	7.65	$7.24 \pm 0.13$	2.90	$2.82 \pm 0.08$	1.10	$1.01 \pm 0.05$
3651031601	59091.2896	59091.3718	4.0963	264.2	7.58	$7.14 \pm 0.17$	2.89	$2.80 \pm 0.10$	1.06	$0.96 \pm 0.06$
3651032001	59119.3602	59119.4403	4.1101	245.0	7.29	$5.31 \pm 0.17$	2.78	$2.45 \pm 0.11$	1.00	$0.53 \pm 0.06$
3651032201	59134.2673	59134.3447	4.1175	848.5	6.49	$5.71 \pm 0.09$	2.71	$2.56 \pm 0.06$	0.77	$0.60 \pm 0.03$
3651032301	59140.2679	59140.4062	4.1205	391.3	6.69	$6.05 \pm 0.13$	2.87	$2.73 \pm 0.09$	0.75	$0.61 \pm 0.04$
3651032401	59144.8590	59144.9954	4.1228	775.2	7.31	$6.90 \pm 0.10$	3.00	$2.91 \pm 0.06$	0.88	$0.79 \pm 0.03$
3651032801	59175.0871	59175.1664	4.1377	1218.4	6.42	$6.07 \pm 0.07$	2.63	$2.56 \pm 0.05$	0.82	$0.75 \pm 0.03$

**Table 7.** *NICER* Spectral Modeling Parameters

OBSID	Phase	Flux	NH <sub>3</sub>	kT <sub>4</sub>	EM <sub>4</sub>	NH <sub>5</sub>	kT <sub>6</sub>	EM <sub>6</sub>	Flux <sub>FeK</sub>
		$10^{-11}$ ergs cm <sup>-2</sup> s <sup>-1</sup>	$10^{22}$ cm <sup>-2</sup>	keV	$10^{58}$ cm <sup>-3</sup>	$10^{22}$ cm <sup>-2</sup>	keV	$10^{58}$ cm <sup>-3</sup>	$10^{-5}$ photons cm <sup>-2</sup> s <sup>-1</sup>
1110010101	3.53	4.96	3.24 ± 0.25	1.01 ± 0.11	0.74 ± 0.18	3.43 ± 0.89	5.91 ± 1.18	0.30 ± 0.04	6.46 ± 4.40
1110010102	3.53	5.03	3.25 ± 0.14	1.32 ± 0.09	0.97 ± 0.10	10.77 ± 2.45	4.40 ± 0.83	0.40 ± 0.08	5.83 ± 3.08
1110010103	3.54	3.84	3.37 ± 0.44	< 1	0.50 ± 0.18	3.43 ± 0.46	2.64 ± 0.42	0.50 ± 0.14	1.58 ± 2.87
1110010105	3.54	4.35	3.59 ± 0.17	1.14 ± 0.09	1.21 ± 0.15	14.52 ± 4.55	2.43 ± 0.71	0.89 ± 0.53	6.38 ± 3.94
1110010106	3.57	2.65	3.73 ± 0.37	1.29 ± 0.15	1.31 ± 0.43				
1110010107	3.57	5.15	3.00 ± 1.37	1.00 ± 0.46	0.29 ± 0.19	3.00 ± 1.24	3.52 ± 0.90	0.49 ± 0.13	9.54 ± 8.21
1110010108	3.60	3.57	3.00 ± 4.25	1.30 ± 0.59	0.12 ± 0.12	3.00 ± 0.71	2.13 ± 0.15	0.66 ± 0.10	2.09 ± 2.98
1110010109	3.61	3.93	3.00 ± 2.36	1.51 ± 0.39	0.90 ± 0.60	3.44 ± 1.23	2.47 ± 0.51	0.54 ± 0.18	4.98 ± 5.77
1110010110	3.61	5.24	3.53 ± 0.07	1.15 ± 0.04	1.36 ± 0.07	11.43 ± 1.41	3.03 ± 0.30	0.68 ± 0.11	6.32 ± 1.74
1110010111	3.61	5.56	3.59 ± 0.29	1.25 ± 0.15	1.30 ± 0.25	15.15 ± 6.17	2.54 ± 0.97	1.14 ± 0.88	
1110010112	3.62	5.32				3.07 ± 0.97	2.63 ± 0.36	0.80 ± 0.17	10.41 ± 6.85
1110010114	3.62	5.45	3.18 ± 0.20	1.16 ± 0.12	0.87 ± 0.19	3.78 ± 1.13	5.35 ± 1.22	0.32 ± 0.06	
1110010115	3.62	4.16	3.00 ± 0.76	1.00 ± 0.32	0.57 ± 0.22	3.41 ± 0.53	2.57 ± 0.45	0.55 ± 0.16	2.79 ± 3.97
1110010116	3.63	5.44	3.26 ± 0.07	1.00 ± 0.07	0.85 ± 0.06	3.62 ± 0.21	3.97 ± 0.22	0.44 ± 0.03	6.01 ± 1.22
1110010117	3.63	5.24	3.00 ± 2.79	1.01 ± 0.75	1.05 ± 1.85	3.00 ± 1.11	3.21 ± 0.44	0.59 ± 0.10	6.12 ± 5.41
1110010119	3.64	7.64	3.02 ± 0.23	1.05 ± 0.07	1.13 ± 0.18	7.11 ± 1.47	5.18 ± 0.80	0.61 ± 0.08	4.01 ± 4.70
1110010120	3.64	5.27	3.37 ± 0.30	1.03 ± 0.10	0.83 ± 0.15	3.13 ± 0.56	4.05 ± 0.76	0.40 ± 0.08	5.23 ± 3.38
1110010121	3.64	5.69	3.00 ± 3.17	< 1	0.02 ± 0.02	3.00 ± 0.71	3.33 ± 0.41	0.60 ± 0.10	8.30 ± 4.79
1110010122	3.64	3.53	3.42 ± 0.36	1.18 ± 0.13	1.19 ± 0.40	7.63 ± 6.03	< 2	0.49 ± 0.38	
1110010123	3.64	4.60	3.01 ± 0.23	1.25 ± 0.09	1.11 ± 0.13	13.40 ± 4.34	2.17 ± 0.61	0.96 ± 0.60	
1110010125	3.64	3.90	3.02 ± 0.26	1.26 ± 0.09	0.98 ± 0.20	7.72 ± 2.75	< 2	0.66 ± 0.25	
1110010126	3.65	5.00	3.34 ± 0.22	1.14 ± 0.10	1.35 ± 0.31	6.92 ± 2.86	3.53 ± 1.24	0.40 ± 0.12	4.16 ± 4.83
1110010127	3.65	4.93	3.63 ± 0.75	1.05 ± 0.18	0.16 ± 0.12	3.00 ± 0.82	2.55 ± 0.40	0.66 ± 0.19	5.97 ± 6.32
1110010128	3.65	4.14	3.00 ± 3.68	1.39 ± 0.21	0.03 ± 0.02	3.00 ± 0.54	2.26 ± 0.13	0.65 ± 0.09	1.86 ± 2.71
1110010129	3.65	6.14	3.08 ± 0.26	1.09 ± 0.11	0.70 ± 0.13	3.00 ± 0.59	6.00 ± 1.91	0.36 ± 0.04	9.83 ± 4.35
1110010131	3.66	3.93	3.00 ± 0.74	1.12 ± 0.17	0.63 ± 0.27	3.34 ± 0.69	2.46 ± 0.65	0.47 ± 0.23	12.53 ± 6.63
1110010132	3.66	3.20	3.42 ± 0.21	1.59 ± 0.12	1.04 ± 0.13				
1110010133	3.67	3.77	3.46 ± 0.15	1.08 ± 0.07	1.27 ± 0.14	13.34 ± 4.47	< 2	0.96 ± 0.66	
1110010134	3.67	4.63	3.43 ± 0.17	1.17 ± 0.09	1.32 ± 0.16	19.46 ± 8.10	< 2	1.55 ± 1.85	10.79 ± 7.23
1110010136	3.67	8.86	3.38 ± 0.11	1.04 ± 0.05	1.42 ± 0.12	11.26 ± 1.24	6.00 ± 1.30	0.76 ± 0.07	5.74 ± 4.37
1110010141	3.68	5.56	3.35 ± 0.04	1.23 ± 0.03	1.20 ± 0.04	10.65 ± 0.77	3.98 ± 0.24	0.50 ± 0.04	4.76 ± 0.98
1110010142	3.68	5.02	3.00 ± 0.29	1.01 ± 0.09	0.63 ± 0.11	3.70 ± 0.38	3.58 ± 0.36	0.47 ± 0.06	7.43 ± 2.46
1110010143	3.68	6.15	3.44 ± 0.26	1.38 ± 0.19	1.19 ± 0.20	15.56 ± 5.34	5.33 ± 1.60	0.48 ± 0.15	
1110010146	3.68	5.61	3.02 ± 0.20	1.00 ± 0.15	0.74 ± 0.16	4.41 ± 0.74	4.16 ± 0.50	0.47 ± 0.06	8.13 ± 3.29
1110010147	3.68	5.35	3.47 ± 0.12	1.14 ± 0.05	1.22 ± 0.11	9.09 ± 1.60	3.35 ± 0.40	0.59 ± 0.10	5.81 ± 2.28
1110010148	3.69	2.76	3.65 ± 0.18	1.50 ± 0.11	1.04 ± 0.11				
1110010149	3.69	5.32	3.37 ± 0.22	< 1	1.05 ± 0.22	6.67 ± 1.64	3.68 ± 0.57	0.54 ± 0.10	
1110010150	3.69	3.77	3.56 ± 0.12	1.17 ± 0.05	1.14 ± 0.10	9.90 ± 2.01	< 2	0.74 ± 0.21	1.75 ± 1.80
1110010151	3.69	6.95	3.29 ± 0.21	1.18 ± 0.09	1.05 ± 0.18	7.77 ± 1.90	4.94 ± 0.88	0.55 ± 0.09	6.43 ± 4.54
1110010152	3.70	5.87	3.06 ± 0.14	1.05 ± 0.07	0.68 ± 0.13	4.46 ± 0.63	4.88 ± 0.48	0.44 ± 0.04	3.75 ± 2.38
1110010153	3.70	3.47	3.04 ± 0.40	< 1	0.47 ± 0.23	4.46 ± 0.55	< 2	0.74 ± 0.18	
1110010155	3.70	4.18	3.22 ± 0.13	1.25 ± 0.08	1.00 ± 0.09	13.10 ± 3.06	< 2	1.05 ± 0.49	4.45 ± 3.02
1110010156	3.71	2.84	3.01 ± 4.43	1.54 ± 1.12		3.09 ± 0.74	< 2	0.59 ± 0.11	
1110010157	3.71	5.25	3.21 ± 0.10	1.08 ± 0.05	0.73 ± 0.09	4.16 ± 0.45	4.72 ± 0.40	0.38 ± 0.03	4.04 ± 1.71
1110010158	3.71	3.54	3.21 ± 0.25	1.02 ± 0.11	0.69 ± 0.20	4.26 ± 0.72	2.57 ± 0.47	0.47 ± 0.14	
1110010159	3.71	5.01	3.07 ± 4.17			3.75 ± 1.24	2.57 ± 0.47	0.77 ± 0.22	
1110010160	3.72	5.22	3.04 ± 0.74	1.23 ± 0.18	0.71 ± 0.28	5.67 ± 2.41	4.36 ± 1.28	0.42 ± 0.12	
1110010161	3.72	5.15	3.72 ± 0.33	1.10 ± 0.14	1.22 ± 0.29	8.90 ± 4.36	5.40 ± 1.78	0.38 ± 0.11	
1110010163	3.72	4.32	3.58 ± 0.15	1.13 ± 0.06	1.13 ± 0.14	8.90 ± 1.98	2.56 ± 0.36	0.64 ± 0.16	2.49 ± 2.29
1110010164	3.72	4.91	3.46 ± 0.08	1.13 ± 0.04	1.12 ± 0.07	9.69 ± 1.16	2.98 ± 0.26	0.64 ± 0.09	5.72 ± 1.58

Table 7 continued on next page



Table 7 (continued)

OBSID	Phase	Flux	NH <sub>3</sub>	kT <sub>4</sub>	EM <sub>4</sub>	NH <sub>5</sub>	kT <sub>6</sub>	EM <sub>6</sub>	Flux <sub>FeK</sub>
		10 <sup>-11</sup> ergs cm <sup>-2</sup> s <sup>-1</sup>	10 <sup>22</sup> cm <sup>-2</sup>	keV	10 <sup>58</sup> cm <sup>-3</sup>	10 <sup>22</sup> cm <sup>-2</sup>	keV	10 <sup>58</sup> cm <sup>-3</sup>	10 <sup>-5</sup> photons cm <sup>-2</sup> s <sup>-1</sup>
1110010165	3.72	4.00	3.15 ± 0.21	2.00 ± 0.41	0.61 ± 0.07	137.56 ± 109.36			
1110010169	3.73	6.63	3.51 ± 0.22	1.27 ± 0.13	1.34 ± 0.21	19.72 ± 5.22	4.33 ± 1.65	0.76 ± 0.33	
1110010171	3.73	2.36	3.56 ± 0.19	1.22 ± 0.09	1.31 ± 0.17				
1110010173	3.74	5.48	3.19 ± 0.23	< 1	0.67 ± 0.11	3.06 ± 0.31	3.61 ± 0.40	0.49 ± 0.07	5.46 ± 2.45
1110010174	3.74	6.13	3.15 ± 0.17	1.18 ± 0.08	0.72 ± 0.09	3.19 ± 0.43	5.36 ± 0.57	0.37 ± 0.04	6.29 ± 2.44
1110010175	3.74	5.58	3.00 ± 0.37	1.19 ± 0.09	1.09 ± 0.16	9.46 ± 2.63	2.99 ± 0.65	0.73 ± 0.25	
1110010176	3.74	6.46	3.04 ± 0.14	1.10 ± 0.08	0.75 ± 0.13	3.63 ± 0.47	4.45 ± 0.51	0.48 ± 0.06	3.04 ± 2.77
1110010179	3.76	5.90	3.64 ± 0.08	1.25 ± 0.05	1.66 ± 0.09	16.77 ± 2.98	< 2	1.60 ± 0.67	2.03 ± 2.67
1110010185	3.78	7.20	3.20 ± 0.47	< 1	0.76 ± 0.25	3.00 ± 1.39	4.99 ± 1.12	0.50 ± 0.09	10.05 ± 7.03
1110010186	3.78	6.45	3.74 ± 0.62	< 1	1.03 ± 0.27	3.25 ± 0.73	4.22 ± 0.93	0.50 ± 0.12	9.19 ± 5.89
1110010187	3.78	0.01							
1110010188	3.79	5.32	3.00 ± 0.66	1.00 ± 0.29	2.29 ± 0.95	5.06 ± 0.89	2.13 ± 0.18	1.10 ± 0.17	3.63 ± 4.14
1110010189	3.79	6.31	3.48 ± 0.07	1.21 ± 0.04	1.58 ± 0.08	13.35 ± 1.74	2.43 ± 0.28	1.14 ± 0.26	10.15 ± 2.29
1110010190	3.79	5.82	3.01 ± 0.24	1.00 ± 0.08	0.94 ± 0.15	4.85 ± 0.48	2.72 ± 0.20	0.78 ± 0.08	1.27 ± 2.36
1110010193	3.80	5.59	3.04 ± 0.68	1.01 ± 0.16	0.74 ± 0.32	3.85 ± 0.55	2.46 ± 0.38	0.83 ± 0.23	
1110010194	3.80	6.83	3.00 ± 0.58	1.09 ± 0.14	0.64 ± 0.18	3.08 ± 0.32	3.19 ± 0.40	0.70 ± 0.13	3.55 ± 3.59
1110010195	3.80	7.29	3.50 ± 0.12	1.16 ± 0.06	1.90 ± 0.17	10.82 ± 2.45	3.18 ± 0.63	0.84 ± 0.25	7.56 ± 4.24
1110010196	3.80	6.34		1.02 ± 0.18	0.01 ± 0.02	3.29 ± 0.25	2.23 ± 0.14	1.15 ± 0.14	11.08 ± 5.49
1110010197	3.80	7.79	3.22 ± 0.14	1.00 ± 0.12	1.15 ± 0.18	3.67 ± 0.47	4.43 ± 0.55	0.59 ± 0.07	
1110010198	3.80	7.65	3.31 ± 0.16	1.02 ± 0.07	0.96 ± 0.14	3.50 ± 0.30	3.77 ± 0.37	0.67 ± 0.08	9.02 ± 3.05
1110010199	3.80	3.96	3.82 ± 1.71	1.31 ± 0.68	1.73 ± 3.37				
1110010201	3.80	4.26	3.03 ± 3.55	1.20 ± 0.23	0.03 ± 0.04	3.11 ± 0.52	< 2	0.82 ± 0.23	
1110010202	3.80	7.20	3.07 ± 0.20	1.03 ± 0.11	0.92 ± 0.25	3.92 ± 0.53	3.15 ± 0.42	0.78 ± 0.14	9.21 ± 4.84
1110010203	3.81	5.98	3.46 ± 0.13	1.22 ± 0.07	1.79 ± 0.16	12.63 ± 3.76	< 2	1.28 ± 0.71	2.68 ± 4.20
1110010204	3.81	7.65	3.32 ± 0.17	1.08 ± 0.07	1.06 ± 0.11	3.12 ± 0.35	4.71 ± 0.46	0.52 ± 0.05	6.55 ± 2.64
1110010205	3.82	7.18	3.07 ± 0.08	1.05 ± 0.05	1.19 ± 0.13	3.73 ± 0.47	4.61 ± 0.46	0.48 ± 0.04	7.75 ± 2.66
1110010206	3.82	7.46	3.19 ± 0.18	1.04 ± 0.07	0.98 ± 0.13	3.15 ± 0.34	4.06 ± 0.43	0.58 ± 0.07	6.33 ± 2.93
1110010207	3.82	7.16	3.11 ± 0.22	1.00 ± 0.16	0.91 ± 0.18	3.14 ± 0.37	3.49 ± 0.45	0.65 ± 0.11	10.72 ± 4.24
1110010208	3.82	7.08	3.24 ± 0.11	1.01 ± 0.05	1.05 ± 0.11	3.48 ± 0.24	3.43 ± 0.27	0.65 ± 0.07	9.90 ± 2.43
2110010201	3.83	8.30	3.00 ± 0.12	1.04 ± 0.03	1.04 ± 0.08	3.52 ± 0.23	4.77 ± 0.26	0.59 ± 0.03	10.83 ± 1.96
2110010202	3.83	8.43	3.17 ± 0.04	1.04 ± 0.02	1.05 ± 0.04	3.41 ± 0.10	4.74 ± 0.13	0.60 ± 0.02	9.52 ± 0.97
2110010203	3.83	6.36	3.00 ± 0.65	1.07 ± 0.14	0.67 ± 0.24	3.23 ± 0.36	2.63 ± 0.36	0.81 ± 0.19	6.57 ± 4.28
2612010101	3.83	8.91	3.00 ± 0.30	< 1	1.06 ± 0.20	3.55 ± 0.51	4.86 ± 0.60	0.63 ± 0.07	19.48 ± 5.33
2612010401	3.84	8.87	3.00 ± 0.21	1.04 ± 0.05	1.09 ± 0.15	4.52 ± 0.53	5.04 ± 0.39	0.64 ± 0.04	14.33 ± 3.15
2612010501	3.84	5.69	3.00 ± 1.16	1.00 ± 0.36	0.38 ± 0.18	3.02 ± 0.31	2.42 ± 0.23	0.87 ± 0.15	3.66 ± 4.01
2612010601	3.85	8.41	3.16 ± 0.08	1.22 ± 0.05	1.49 ± 0.10	9.11 ± 1.09	4.90 ± 0.47	0.65 ± 0.06	5.81 ± 2.94
2612010701	3.85	8.51	3.00 ± 0.31	< 1	0.69 ± 0.11	3.16 ± 0.23	4.56 ± 0.34	0.66 ± 0.04	7.31 ± 2.77
2612010801	3.85	8.00	3.02 ± 0.29	< 1	0.63 ± 0.16	3.25 ± 0.29	3.69 ± 0.39	0.76 ± 0.09	3.03 ± 3.56
2612010802	3.85	8.52	3.27 ± 0.13	1.13 ± 0.05	1.59 ± 0.17	8.48 ± 1.38	3.65 ± 0.43	0.90 ± 0.14	10.39 ± 4.09
2612010901	3.86	8.53	3.69 ± 0.13	1.26 ± 0.08	1.88 ± 0.17	14.96 ± 2.52	3.76 ± 0.59	0.96 ± 0.22	9.15 ± 4.50
2612011001	3.86	9.02	3.34 ± 0.08	1.35 ± 0.06	1.56 ± 0.09	13.15 ± 1.37	4.14 ± 0.40	0.88 ± 0.11	7.57 ± 2.89
2612011101	3.87	5.80	3.22 ± 0.09	2.00 ± 0.16	1.22 ± 0.06				6.42 ± 3.51
2612011201	3.87	8.61	3.00 ± 0.58	1.27 ± 0.13	1.04 ± 0.32	5.94 ± 1.67	4.01 ± 0.69	0.77 ± 0.14	6.25 ± 5.84
2612011202	3.87	9.06	3.12 ± 0.18	1.30 ± 0.13	1.49 ± 0.20	11.61 ± 2.66	3.40 ± 0.69	1.11 ± 0.34	
2612011301	3.87	5.76	3.05 ± 2.73	1.96 ± 2.08		3.75 ± 0.60	2.02 ± 0.16	1.27 ± 0.20	
2612011401	3.88	8.71	3.00 ± 0.44	1.00 ± 0.23	0.63 ± 0.18	3.57 ± 0.39	4.42 ± 0.45	0.73 ± 0.07	
2612011402	3.88	8.82	3.00 ± 0.42	< 1	0.84 ± 0.24	3.96 ± 0.56	4.21 ± 0.53	0.75 ± 0.09	19.99 ± 6.11
2612011501	3.88	8.17	3.43 ± 0.08	1.26 ± 0.05	1.60 ± 0.09	12.91 ± 1.39	3.03 ± 0.30	1.18 ± 0.20	4.74 ± 2.43
2612011601	3.88	8.19	3.12 ± 0.14	1.05 ± 0.08	0.84 ± 0.15	3.64 ± 0.37	4.37 ± 0.44	0.65 ± 0.06	5.22 ± 3.56
2612011701	3.88	8.51	3.01 ± 0.45	1.36 ± 0.16	1.06 ± 0.34	5.46 ± 1.98	4.36 ± 0.85	0.62 ± 0.13	10.09 ± 6.63
2612011801	3.89	9.79	3.01 ± 0.19	1.00 ± 0.13	0.82 ± 0.13	3.72 ± 0.26	4.27 ± 0.30	0.83 ± 0.06	16.45 ± 3.52
2612011901	3.89	8.81	3.00 ± 0.25	< 1	0.80 ± 0.13	3.90 ± 0.22	3.35 ± 0.19	0.94 ± 0.07	10.44 ± 2.72
2612012001	3.90	11.16	3.01 ± 0.37	1.16 ± 0.12	0.58 ± 0.11	3.09 ± 0.23	5.19 ± 0.37	0.79 ± 0.05	14.76 ± 3.53

Table 7 continued on next page

Table 7 (continued)

OBSID	Phase	Flux	NH <sub>3</sub>	kT <sub>4</sub>	EM <sub>4</sub>	NH <sub>5</sub>	kT <sub>6</sub>	EM <sub>6</sub>	Flux <sub>F<sub>e</sub>K</sub>
		10 <sup>-11</sup> ergs cm <sup>-2</sup> s <sup>-1</sup>	10 <sup>22</sup> cm <sup>-2</sup>	keV	10 <sup>58</sup> cm <sup>-3</sup>	10 <sup>22</sup> cm <sup>-2</sup>	keV	10 <sup>58</sup> cm <sup>-3</sup>	10 <sup>-5</sup> photons cm <sup>-2</sup> s <sup>-1</sup>
2612012101	3.90	11.65	3.14 ± 0.09	1.06 ± 0.05	1.04 ± 0.12	3.93 ± 0.26	5.30 ± 0.29	0.83 ± 0.04	9.58 ± 2.86
2612012401	3.91	10.23	3.22 ± 0.17	1.00 ± 0.18	1.37 ± 0.31	4.14 ± 0.72	4.84 ± 0.75	0.75 ± 0.09	17.12 ± 7.43
2612012501	3.91	13.50	3.23 ± 0.18	1.15 ± 0.09	1.19 ± 0.20	3.41 ± 0.40	6.00 ± 1.12	0.85 ± 0.06	9.96 ± 5.68
2612012502	3.91	14.29	3.02 ± 0.21	1.14 ± 0.08	1.42 ± 0.32	4.64 ± 0.83	6.00 ± 1.27	0.94 ± 0.07	17.53 ± 7.37
2612012601	3.92	12.23	3.00 ± 0.88	1.12 ± 0.24	0.77 ± 0.36	3.24 ± 0.63	5.00 ± 1.08	0.90 ± 0.17	12.35 ± 10.06
2612012701	3.92	13.33	3.18 ± 0.24	< 1	1.13 ± 0.35	3.87 ± 0.60	5.38 ± 0.78	0.98 ± 0.11	
2612012901	3.93	13.43	3.00 ± 0.34	< 1	1.14 ± 0.27	4.10 ± 0.47	4.64 ± 0.43	1.08 ± 0.08	23.64 ± 6.90
2612020301	3.95	15.02	3.54 ± 0.22	1.07 ± 0.09	2.48 ± 0.42	9.54 ± 2.17	3.94 ± 0.70	1.66 ± 0.38	17.96 ± 11.62
2612020401	3.95	15.39	3.16 ± 0.17	1.77 ± 0.21	1.80 ± 0.20	13.91 ± 2.96	6.00 ± 2.13	1.03 ± 0.18	12.75 ± 9.46
2612020501	3.95	16.13	3.21 ± 0.21	1.31 ± 0.12	2.06 ± 0.36	7.90 ± 1.87	5.28 ± 0.81	1.21 ± 0.17	17.85 ± 10.25
2612020701	3.95	15.47	3.00 ± 0.57	1.00 ± 0.31	0.94 ± 0.34	3.38 ± 0.44	5.12 ± 0.66	1.14 ± 0.11	32.77 ± 11.54
2612020801	3.95	17.09	3.00 ± 0.29	1.12 ± 0.07	1.62 ± 0.35	4.90 ± 0.78	5.71 ± 0.53	1.19 ± 0.08	26.17 ± 8.03
2612020901	3.95	19.09	3.29 ± 0.13	1.73 ± 0.15	2.45 ± 0.20	15.60 ± 2.35	5.68 ± 0.72	1.44 ± 0.19	15.41 ± 9.23
2612021001	3.96	18.69	3.00 ± 0.46	1.22 ± 0.11	2.03 ± 0.42	7.66 ± 1.48	3.73 ± 0.51	2.04 ± 0.35	47.12 ± 14.80
2612021101	3.96	19.54	3.01 ± 0.30	1.06 ± 0.06	1.81 ± 0.33	5.11 ± 0.55	4.27 ± 0.30	1.75 ± 0.12	32.43 ± 7.47
2612021102	3.96	21.27	3.47 ± 0.12	1.74 ± 0.14	3.01 ± 0.24	17.25 ± 2.62	3.75 ± 0.55	2.33 ± 0.51	20.34 ± 9.68
2612021201	3.96	22.13	3.30 ± 0.05	1.85 ± 0.07	2.75 ± 0.08	15.70 ± 0.98	5.26 ± 0.29	1.58 ± 0.10	27.17 ± 3.84
2612021202	3.96	21.83	3.01 ± 0.27	1.07 ± 0.05	1.81 ± 0.32	4.82 ± 0.47	4.63 ± 0.29	1.81 ± 0.10	32.67 ± 7.65
2612021301	3.96	22.18	3.00 ± 0.20	1.00 ± 0.10	1.41 ± 0.20	3.95 ± 0.18	4.47 ± 0.18	1.89 ± 0.07	32.53 ± 5.13
2612021801	3.96	21.59	3.00 ± 0.13	1.04 ± 0.03	1.51 ± 0.14	4.54 ± 0.18	4.99 ± 0.15	1.72 ± 0.04	35.68 ± 3.51
2612021901	3.97	21.16	3.00 ± 0.26	< 1	1.05 ± 0.19	3.68 ± 0.19	5.16 ± 0.27	1.61 ± 0.06	34.30 ± 5.86
2612022003	3.97	21.43	3.01 ± 0.20	1.13 ± 0.06	1.62 ± 0.28	4.90 ± 0.44	5.12 ± 0.31	1.66 ± 0.08	33.31 ± 6.72
2612022102	3.97	20.45	3.00 ± 0.41	1.00 ± 0.19	1.24 ± 0.35	4.23 ± 0.40	4.69 ± 0.38	1.71 ± 0.11	32.94 ± 9.37
2612022103	3.97	21.88	3.00 ± 0.21	1.04 ± 0.05	1.41 ± 0.22	4.14 ± 0.28	5.89 ± 0.29	1.54 ± 0.05	28.81 ± 5.83
2612022104	3.97	23.03	3.35 ± 0.04	1.64 ± 0.04	2.85 ± 0.07	14.23 ± 0.60	4.53 ± 0.17	2.09 ± 0.10	43.40 ± 3.50
2612022105	3.97	22.97	3.37 ± 0.03	1.71 ± 0.03	2.92 ± 0.05	15.21 ± 0.47	4.37 ± 0.12	2.12 ± 0.07	30.56 ± 2.31
2612022201	3.97	24.31	3.35 ± 0.02	1.75 ± 0.03	2.95 ± 0.05	15.29 ± 0.43	4.63 ± 0.12	2.13 ± 0.07	37.26 ± 2.35
2612022202	3.97	24.21	3.30 ± 0.04	1.64 ± 0.04	3.00 ± 0.08	14.90 ± 0.64	4.31 ± 0.18	2.38 ± 0.13	33.11 ± 3.64
2612022301	3.97	23.82	3.48 ± 0.05	1.26 ± 0.03	3.38 ± 0.12	10.59 ± 0.50	4.32 ± 0.17	2.38 ± 0.11	38.29 ± 4.29
2612022302	3.97	24.65	3.33 ± 0.06	1.57 ± 0.06	2.97 ± 0.11	13.11 ± 0.75	5.15 ± 0.27	2.06 ± 0.11	37.20 ± 5.17
2612022401	3.97	23.81	3.38 ± 0.05	1.28 ± 0.03	3.12 ± 0.13	9.82 ± 0.50	4.95 ± 0.22	2.06 ± 0.09	40.45 ± 4.64
2612022402	3.97	22.78	3.49 ± 0.05	1.44 ± 0.04	3.37 ± 0.11	14.40 ± 0.67	4.15 ± 0.19	2.41 ± 0.14	35.42 ± 3.99
2612022403	3.97	22.42	3.47 ± 0.05	1.43 ± 0.04	3.20 ± 0.12	12.74 ± 0.72	4.17 ± 0.21	2.28 ± 0.15	27.84 ± 4.35
2612022501	3.97	22.72	3.51 ± 0.05	1.39 ± 0.03	3.25 ± 0.10	13.04 ± 0.58	3.88 ± 0.16	2.59 ± 0.14	34.35 ± 3.72
2612022502	3.97	23.36	3.54 ± 0.05	1.27 ± 0.03	3.28 ± 0.13	10.78 ± 0.54	4.03 ± 0.17	2.50 ± 0.14	40.91 ± 4.37
2612022601	3.97	24.03	3.48 ± 0.03	1.14 ± 0.02	3.31 ± 0.09	9.47 ± 0.29	4.19 ± 0.11	2.52 ± 0.08	38.72 ± 2.96
2612022602	3.97	24.02	3.57 ± 0.05	1.25 ± 0.03	3.39 ± 0.12	10.93 ± 0.51	4.09 ± 0.16	2.61 ± 0.13	37.96 ± 4.22
2612022701	3.98	25.58	3.55 ± 0.05	1.21 ± 0.02	3.43 ± 0.12	9.93 ± 0.39	4.49 ± 0.14	2.52 ± 0.09	38.35 ± 3.84
2612022702	3.98	25.13	3.34 ± 0.09	1.21 ± 0.05	3.00 ± 0.22	9.34 ± 0.70	4.19 ± 0.27	2.67 ± 0.20	33.78 ± 7.49
2612022703	3.98	26.47	3.58 ± 0.11	1.59 ± 0.11	3.32 ± 0.25	18.88 ± 1.83	3.74 ± 0.38	3.64 ± 0.55	51.31 ± 11.10
2612023002	3.98	30.43	3.60 ± 0.13	1.51 ± 0.11	4.56 ± 0.39	11.89 ± 1.76	4.59 ± 0.52	2.51 ± 0.34	19.21 ± 11.73
2612023003	3.98	26.43	3.61 ± 0.06	1.44 ± 0.05	4.97 ± 0.20	13.39 ± 1.16	3.79 ± 0.28	2.50 ± 0.27	36.39 ± 6.23
2612023101	3.98	23.64	3.63 ± 0.03	1.34 ± 0.02	4.89 ± 0.09	12.77 ± 0.50	3.65 ± 0.12	2.38 ± 0.11	28.87 ± 2.55
2612023102	3.98	21.20	3.63 ± 0.02	1.33 ± 0.02	4.44 ± 0.08	12.50 ± 0.48	3.87 ± 0.13	1.97 ± 0.09	25.99 ± 2.17
2612023201	3.98	22.51	3.66 ± 0.03	1.26 ± 0.02	4.42 ± 0.10	10.22 ± 0.43	3.92 ± 0.12	2.12 ± 0.08	28.98 ± 2.53
2612023202	3.98	22.31	3.65 ± 0.04	1.34 ± 0.02	4.14 ± 0.11	12.56 ± 0.60	3.86 ± 0.16	2.25 ± 0.12	30.10 ± 3.28
2612023301	3.98	19.53	3.70 ± 0.04	1.35 ± 0.03	3.82 ± 0.10	14.45 ± 0.72	3.43 ± 0.16	2.36 ± 0.17	34.31 ± 3.21
2612023302	3.98	16.67	3.70 ± 0.03	1.13 ± 0.02	3.60 ± 0.08	12.33 ± 0.49	3.42 ± 0.12	2.19 ± 0.12	29.03 ± 2.49
2612023303	3.98	15.01	3.70 ± 0.03	1.16 ± 0.01	3.10 ± 0.06	12.29 ± 0.40	3.50 ± 0.10	1.90 ± 0.08	25.95 ± 1.84
2612023401	3.98	14.37	3.73 ± 0.03	1.14 ± 0.02	2.75 ± 0.06	12.70 ± 0.44	3.64 ± 0.12	1.85 ± 0.08	24.36 ± 1.98
2612023402	3.98	14.75	3.75 ± 0.03	1.18 ± 0.02	2.66 ± 0.06	12.38 ± 0.42	3.75 ± 0.12	1.80 ± 0.08	28.08 ± 1.97
2612023501	3.98	14.98	3.47 ± 0.09	1.07 ± 0.03	0.24 ± 0.03	3.44 ± 0.05	4.58 ± 0.12	1.22 ± 0.03	30.71 ± 2.20
2612023502	3.99	16.83	3.76 ± 0.05	1.28 ± 0.03	2.65 ± 0.08	12.26 ± 0.53	3.78 ± 0.15	2.01 ± 0.11	28.61 ± 2.77

Table 7 continued on next page

Table 7 (continued)

OBSID	Phase	Flux	NH <sub>3</sub>	kT <sub>4</sub>	EM <sub>4</sub>	NH <sub>5</sub>	kT <sub>6</sub>	EM <sub>6</sub>	Flux <sub>F<sub>e</sub>K</sub>
		10 <sup>-11</sup> ergs cm <sup>-2</sup> s <sup>-1</sup>	10 <sup>22</sup> cm <sup>-2</sup>	keV	10 <sup>58</sup> cm <sup>-3</sup>	10 <sup>22</sup> cm <sup>-2</sup>	keV	10 <sup>58</sup> cm <sup>-3</sup>	10 <sup>-5</sup> photons cm <sup>-2</sup> s <sup>-1</sup>
2612023601	3.99	21.52	3.78 ± 0.05	1.50 ± 0.04	3.03 ± 0.10	13.97 ± 0.67	4.13 ± 0.18	2.26 ± 0.13	39.93 ± 3.77
2612023602	3.99	23.72	3.91 ± 0.05	1.34 ± 0.03	3.85 ± 0.12	12.73 ± 0.59	3.64 ± 0.15	2.86 ± 0.17	45.01 ± 3.97
2612023701	3.99	22.99	3.63 ± 0.18	1.41 ± 0.13	3.27 ± 0.40	11.94 ± 2.18	3.66 ± 0.50	2.68 ± 0.54	22.52 ± 12.51
2612023702	3.99	12.97	3.85 ± 0.04	1.20 ± 0.02	2.48 ± 0.07	13.91 ± 0.60	3.47 ± 0.13	1.78 ± 0.10	24.52 ± 2.26
2612023801	3.99	19.14	4.08 ± 0.08	1.45 ± 0.06	3.09 ± 0.16	16.10 ± 1.19	3.19 ± 0.23	2.95 ± 0.35	31.45 ± 5.01
2612023902	3.99	7.06	3.72 ± 0.03	1.06 ± 0.02	1.62 ± 0.04	14.65 ± 0.56	2.84 ± 0.11	1.35 ± 0.09	15.83 ± 1.15
2612023903	3.99	7.72	3.78 ± 0.05	1.09 ± 0.03	1.42 ± 0.05	15.30 ± 0.76	3.20 ± 0.17	1.38 ± 0.12	17.03 ± 1.87
2612024001	3.99	7.36	3.82 ± 0.06	1.09 ± 0.03	1.32 ± 0.05	16.42 ± 0.81	3.24 ± 0.18	1.36 ± 0.12	17.68 ± 1.92
2612024002	3.99	8.97	3.81 ± 0.07	< 1	1.30 ± 0.06	12.82 ± 0.54	3.64 ± 0.16	1.37 ± 0.08	21.89 ± 2.16
2612024101	3.99	6.83	3.86 ± 0.07	1.06 ± 0.03	1.20 ± 0.06	14.56 ± 0.80	3.55 ± 0.20	1.06 ± 0.09	14.52 ± 1.91
2612024102	3.99	8.45	4.05 ± 0.06	1.07 ± 0.03	1.23 ± 0.05	15.16 ± 0.62	3.36 ± 0.15	1.53 ± 0.11	21.46 ± 1.96
2612024201	3.99	11.11	4.21 ± 0.07	1.07 ± 0.03	1.33 ± 0.07	17.00 ± 0.57	3.66 ± 0.15	2.02 ± 0.12	27.90 ± 2.58
2612024202	3.99	10.65	4.01 ± 0.09	< 1	1.22 ± 0.08	14.96 ± 0.62	3.58 ± 0.17	1.89 ± 0.13	25.78 ± 2.99
2612024203	3.99	4.31	3.87 ± 0.08	1.06 ± 0.04	0.87 ± 0.05	17.89 ± 1.37	2.88 ± 0.26	0.97 ± 0.16	13.07 ± 1.75
2612024301	3.99	2.21	3.45 ± 0.09	< 1	0.60 ± 0.04	18.36 ± 2.40	2.83 ± 0.46	0.48 ± 0.14	5.69 ± 1.34
2612024302	3.99	1.50	4.65 ± 0.31	< 1	6.17 ± 2.25	20.08 ± 5.46	< 2	0.65 ± 0.49	9.29 ± 2.31
2612024401	3.99	1.97	3.15 ± 0.09	1.00 ± 0.08	0.47 ± 0.04	23.71 ± 2.36	4.63 ± 0.70	0.28 ± 0.05	4.82 ± 1.47
2612024402	4.00	0.55	3.72 ± 0.43	< 1	2.99 ± 1.85	5.55 ± 4.34	< 2	0.09 ± 0.07	4.02 ± 1.23
2612024501	4.00	0.37	3.45 ± 0.19	< 1	0.82 ± 0.17	13.04 ± 12.54	< 2	0.04 ± 0.08	2.30 ± 0.66
2612024502	4.00	0.41	3.00 ± 0.26	1.21 ± 0.06	0.08 ± 0.01				0.74 ± 0.83
2612024601	4.00	0.17	3.00 ± 0.84	< 1	0.51 ± 0.22				
2612024602	4.00	0.13	3.75 ± 0.89	< 1	5.37 ± 5.86				
2612024701	4.00	0.24	3.00 ± 0.28	< 1	0.17 ± 0.02				1.22 ± 0.71
2612024702	4.00	0.46	3.13 ± 0.10	< 1	0.20 ± 0.01	32.24 ± 13.11	< 2	0.19 ± 0.32	2.40 ± 0.60
2612024801	4.00	0.29	3.21 ± 0.16	1.00 ± 0.12	0.19 ± 0.02				1.53 ± 0.80
2612024802	4.00	0.19	3.00 ± 0.53	< 1	0.14 ± 0.03				1.12 ± 1.25
2612024803	4.00	0.11	3.00 ± 2.51	< 1	0.02 ± 0.02				
2612024901	4.00	0.34	3.00 ± 5.25	1.00 ± 1.26	0.27 ± 0.44				
2612024902	4.00	0.43	3.00 ± 0.28	1.00 ± 0.11	0.21 ± 0.02	32.74 ± 27.07			1.53 ± 0.98
2612025001	4.00	1.17	3.00 ± 0.51	1.44 ± 0.15	0.17 ± 0.03	30.26 ± 5.22	6.00 ± 2.48	0.16 ± 0.03	0.87 ± 1.37
2612025002	4.00	1.00	3.00 ± 0.51	1.55 ± 0.17	0.07 ± 0.01	53.80 ± 14.90	6.00 ± 3.41	0.17 ± 0.06	
2612025101	4.00	0.43	3.00 ± 0.44	1.38 ± 0.11	0.05 ± 0.01	120.23 ± 95.89			1.75 ± 1.02
2612025102	4.00	0.41	3.51 ± 0.28	< 1	0.19 ± 0.04	30.63 ± 27.53			1.49 ± 1.21
2612025103	4.00	0.13	3.00 ± 0.70	< 1	0.10 ± 0.03				
2612025201	4.00	0.35	4.94 ± 0.47	< 1	6.33 ± 5.54	21.08 ± 16.15	< 2		0.95 ± 0.93
2612025202	4.00	0.50	4.83 ± 0.23	1.00 ± 0.08	0.02 ± 0.00	200.00 ± 182.90			0.74 ± 0.99
2612025301	4.01	0.50	3.01 ± 4.65	1.07 ± 0.32	0.00 ± 0.00	3.00 ± 0.71	< 2	0.09 ± 0.02	2.38 ± 0.98
3651010101	4.01	0.24	4.91 ± 0.60	1.03 ± 0.09	6.27 ± 3.44				
3651010301	4.01	0.45	3.44 ± 0.17	1.14 ± 0.06	0.06 ± 0.01	131.01 ± 57.99			2.96 ± 0.90
3651010501	4.01	0.75	4.55 ± 0.30	1.05 ± 0.06	6.33 ± 3.66	22.63 ± 4.00	3.14 ± 0.85	0.19 ± 0.09	2.51 ± 0.96
3651010601	4.01	1.02	3.52 ± 0.25	1.11 ± 0.08	1.94 ± 0.52	37.49 ± 5.14	3.36 ± 0.92	0.35 ± 0.16	5.11 ± 1.37
3651010701	4.01	0.70	3.00 ± 0.94	1.00 ± 0.35	0.05 ± 0.02	27.56 ± 28.47	2.53 ± 4.02		
3651011201	4.01	1.62	5.00 ± 2.31	1.03 ± 0.16	6.01 ± 5.75	43.70 ± 9.54	3.82 ± 2.22	0.64 ± 0.50	4.43 ± 4.76
3651011301	4.01	2.23	3.29 ± 0.51	1.21 ± 0.21	0.17 ± 0.06	42.35 ± 5.73	4.78 ± 1.13	0.59 ± 0.17	11.78 ± 3.99
3651011401	4.01	1.45	3.00 ± 1.01	1.29 ± 0.23	0.04 ± 0.01	77.90 ± 19.86	< 2	3.88 ± 7.42	6.09 ± 3.41
3651011501	4.01	1.84	3.22 ± 0.41	< 1	0.12 ± 0.04	45.90 ± 7.31	< 2	2.43 ± 2.16	12.81 ± 2.78
3651011601	4.01	3.11	3.00 ± 1.24	< 1	0.00 ± 0.00	28.39 ± 1.61	3.87 ± 0.47	0.81 ± 0.13	10.66 ± 2.25
3651011701	4.01	3.08	3.47 ± 0.37	1.00 ± 0.25	0.20 ± 0.05	35.96 ± 3.94	2.57 ± 0.56	1.89 ± 0.88	7.94 ± 3.15
3651011801	4.01	2.94	3.00 ± 0.91	1.37 ± 0.24	0.16 ± 0.05	40.91 ± 4.93	< 2	3.44 ± 1.99	8.30 ± 3.32
3651011901	4.02	4.04	4.61 ± 0.93	1.08 ± 0.32	0.99 ± 0.86	28.81 ± 2.69	3.83 ± 0.68	1.10 ± 0.28	10.56 ± 3.90
3651012001	4.02	4.17	3.71 ± 0.29	1.00 ± 0.20	0.20 ± 0.04	26.90 ± 1.40	3.44 ± 0.33	1.24 ± 0.19	16.12 ± 2.52
3651012101	4.02	4.52	4.14 ± 1.02	1.14 ± 0.40	0.54 ± 0.50	26.32 ± 2.56	3.17 ± 0.53	1.48 ± 0.43	17.53 ± 4.81
3651012701	4.02	5.77	4.29 ± 0.69	1.36 ± 0.34	1.09 ± 0.75	21.64 ± 1.37	3.51 ± 0.35	1.45 ± 0.22	13.50 ± 3.60

Table 7 continued on next page

Table 7 (continued)

OBSID	Phase	Flux	NH <sub>3</sub>	kT <sub>4</sub>	EM <sub>4</sub>	NH <sub>5</sub>	kT <sub>6</sub>	EM <sub>6</sub>	Flux <sub>FeK</sub>
		10 <sup>-11</sup> ergs cm <sup>-2</sup> s <sup>-1</sup>	10 <sup>22</sup> cm <sup>-2</sup>	keV	10 <sup>58</sup> cm <sup>-3</sup>	10 <sup>22</sup> cm <sup>-2</sup>	keV	10 <sup>58</sup> cm <sup>-3</sup>	10 <sup>-5</sup> photons cm <sup>-2</sup> s <sup>-1</sup>
3651012801	4.02	5.98	3.89 ± 0.45	1.82 ± 0.38	0.09 ± 0.02	28.39 ± 2.02	2.64 ± 0.27	2.68 ± 0.57	18.01 ± 3.67
3651012901	4.02	5.93	5.00 ± 0.73	1.16 ± 0.08	5.32 ± 1.76	20.64 ± 0.85	3.17 ± 0.20	1.68 ± 0.18	16.66 ± 2.37
3651013001	4.02	6.75	3.96 ± 0.45	1.25 ± 0.21	0.59 ± 0.23	18.57 ± 0.77	4.10 ± 0.27	1.27 ± 0.10	17.41 ± 2.84
3651013101	4.02	7.89	3.80 ± 0.33	2.00 ± 0.81	0.22 ± 0.04	22.02 ± 1.22	4.32 ± 0.32	1.47 ± 0.14	13.39 ± 3.91
3651013201	4.02	7.00	4.30 ± 0.35	1.00 ± 0.21	0.31 ± 0.07	20.10 ± 0.93	3.69 ± 0.26	1.57 ± 0.16	14.17 ± 3.10
3651013301	4.02	7.65	5.00 ± 0.92	2.00 ± 0.56	0.08 ± 0.01	21.99 ± 1.42	4.08 ± 0.34	1.39 ± 0.15	20.09 ± 3.36
3651013401	4.02	7.30	4.65 ± 0.35	1.08 ± 0.12	0.36 ± 0.08	18.57 ± 0.93	3.78 ± 0.26	1.49 ± 0.15	16.92 ± 3.03
3651013501	4.02	6.38	4.76 ± 0.72	1.00 ± 0.30	6.33 ± 11.73	16.25 ± 0.90	3.39 ± 0.27	1.43 ± 0.17	19.64 ± 3.30
3651013601	4.02	6.82	4.21 ± 0.41	2.00 ± 0.79	0.15 ± 0.03	20.52 ± 1.43	3.32 ± 0.30	1.62 ± 0.23	18.43 ± 3.15
3651013701	4.02	6.47	4.14 ± 0.31	2.00 ± 0.65	0.17 ± 0.03	23.90 ± 1.65	2.51 ± 0.22	2.68 ± 0.50	12.96 ± 2.80
3651013801	4.02	6.83	3.83 ± 0.67	2.00 ± 0.63	0.04 ± 0.01	17.01 ± 1.29	3.84 ± 0.36	1.20 ± 0.14	15.98 ± 3.36
3651013901	4.03	7.26	5.00 ± 2.00	1.27 ± 0.26	5.11 ± 4.63	16.99 ± 1.72	3.36 ± 0.51	1.68 ± 0.39	15.58 ± 6.32
3651014001	4.03	7.89	4.28 ± 0.37	1.86 ± 0.35	0.32 ± 0.06	18.83 ± 1.44	3.88 ± 0.34	1.48 ± 0.17	8.47 ± 4.49
3651014101	4.03	7.15	4.65 ± 0.43	1.00 ± 0.25	0.36 ± 0.09	15.83 ± 0.88	3.52 ± 0.24	1.46 ± 0.15	15.95 ± 3.08
3651014201	4.03	7.76	4.02 ± 0.34	1.29 ± 0.18	0.29 ± 0.06	15.22 ± 0.90	4.36 ± 0.31	1.20 ± 0.10	10.75 ± 3.13
3651014401	4.03	7.16	5.00 ± 0.96	1.19 ± 0.04	0.03 ± 0.01	12.83 ± 0.41	3.92 ± 0.14	1.13 ± 0.05	17.12 ± 1.52
3651014501	4.03	7.82	5.00 ± 0.45	1.21 ± 0.06	0.18 ± 0.02	15.49 ± 0.64	4.30 ± 0.21	1.20 ± 0.07	12.35 ± 2.02
3651014601	4.03	7.86	4.83 ± 0.29	1.04 ± 0.09	0.48 ± 0.08	15.16 ± 0.75	3.81 ± 0.22	1.40 ± 0.11	14.27 ± 2.59
3651014701	4.03	7.60	4.19 ± 0.35	1.88 ± 0.28	0.30 ± 0.06	16.32 ± 0.96	3.42 ± 0.23	1.54 ± 0.15	13.14 ± 2.82
3651014801	4.03	7.66	5.00 ± 0.54	1.15 ± 0.10	0.52 ± 0.08	17.28 ± 0.87	3.30 ± 0.19	1.74 ± 0.16	15.28 ± 2.59
3651014901	4.03	7.94	4.07 ± 0.34	1.90 ± 0.26	0.16 ± 0.03	15.26 ± 0.96	3.66 ± 0.24	1.35 ± 0.12	14.36 ± 2.72
3651015001	4.03	7.73	4.82 ± 0.41	2.00 ± 0.36	0.10 ± 0.02	15.53 ± 1.07	3.77 ± 0.26	1.17 ± 0.10	18.55 ± 2.56
3651015101	4.03	7.86	4.51 ± 0.29	1.25 ± 0.13	0.41 ± 0.07	14.39 ± 0.84	3.83 ± 0.24	1.33 ± 0.11	12.17 ± 2.62
3651020101	4.03	7.65	5.00 ± 0.60	1.00 ± 0.17	0.59 ± 0.11	14.48 ± 0.77	3.50 ± 0.20	1.48 ± 0.12	11.61 ± 2.52
3651020201	4.03	7.92	5.00 ± 0.44	1.21 ± 0.11	0.60 ± 0.08	14.90 ± 0.90	3.71 ± 0.22	1.39 ± 0.11	12.25 ± 2.50
3651020301	4.03	6.66	4.59 ± 0.34	1.17 ± 0.15	0.54 ± 0.11	18.07 ± 1.74	2.30 ± 0.23	2.73 ± 0.60	11.28 ± 3.89
3651020401	4.03	6.93	4.31 ± 0.41	1.41 ± 0.24	0.40 ± 0.09	15.19 ± 1.57	2.78 ± 0.28	1.75 ± 0.31	20.04 ± 4.16
3651020501	4.04	7.62	4.70 ± 0.71	1.00 ± 0.39	0.54 ± 0.23	11.82 ± 1.57	3.70 ± 0.50	1.22 ± 0.21	11.07 ± 5.49
3651020502	4.04	7.61	5.00 ± 0.62	1.39 ± 0.11	0.27 ± 0.04	15.46 ± 1.45	3.34 ± 0.31	1.40 ± 0.19	17.83 ± 3.50
3651020601	4.04	5.70	3.49 ± 0.82	1.75 ± 0.64	0.34 ± 0.17	16.44 ± 3.59	2.22 ± 0.53	2.26 ± 1.18	14.45 ± 8.08
3651020602	4.04	7.91	4.93 ± 0.58	1.00 ± 0.27	0.35 ± 0.12	13.62 ± 2.56	4.46 ± 0.86	1.06 ± 0.24	12.79 ± 8.90
3651020701	4.04	7.90	5.00 ± 1.25	1.15 ± 0.16	4.77 ± 2.71	10.51 ± 0.94	4.26 ± 0.44	1.04 ± 0.13	17.57 ± 4.48
3651020801	4.04	7.23	5.00 ± 1.02	1.00 ± 0.40	4.82 ± 2.98	11.06 ± 0.84	3.25 ± 0.24	1.34 ± 0.15	11.25 ± 3.00
3651020901	4.04	7.27	4.67 ± 0.23	1.04 ± 0.08	0.70 ± 0.10	13.62 ± 0.90	2.97 ± 0.18	1.60 ± 0.17	17.38 ± 2.71
3651021001	4.04	7.71	5.00 ± 0.86	1.10 ± 0.10	4.54 ± 1.81	9.68 ± 0.60	4.03 ± 0.26	1.05 ± 0.09	12.45 ± 2.51
3651021101	4.04	7.70	5.00 ± 0.73	1.03 ± 0.10	6.33 ± 4.65	10.13 ± 0.66	3.83 ± 0.27	1.12 ± 0.10	11.09 ± 2.80
3651021201	4.04	7.53	5.00 ± 0.87	< 1	5.99 ± 3.02	8.67 ± 0.58	3.93 ± 0.25	0.99 ± 0.08	16.06 ± 2.53
3651021301	4.04	6.19	5.00 ± 1.31	1.00 ± 0.42	6.33 ± 9.37	10.24 ± 1.14	2.68 ± 0.28	1.41 ± 0.26	16.98 ± 4.02
3651030101	4.04	7.33	5.00 ± 0.63	< 1	6.33 ± 4.44	9.47 ± 0.61	3.58 ± 0.19	1.10 ± 0.08	10.95 ± 2.11
3651030201	4.05	7.14	4.82 ± 0.36	1.04 ± 0.09	6.33 ± 4.55	8.87 ± 0.61	3.38 ± 0.21	1.11 ± 0.10	15.32 ± 2.35
3651030301	4.05	7.24	4.52 ± 0.38	< 1	2.36 ± 0.86	8.46 ± 0.80	3.59 ± 0.24	1.01 ± 0.09	7.20 ± 2.55
3651030501	4.06	6.95	4.34 ± 0.39	1.11 ± 0.12	2.07 ± 0.71	8.41 ± 1.01	3.43 ± 0.27	1.00 ± 0.11	5.29 ± 2.71
3651030601	4.06	6.42	3.88 ± 0.52	1.14 ± 0.24	0.45 ± 0.26	5.70 ± 1.27	4.84 ± 0.96	0.56 ± 0.10	14.19 ± 6.30
3651030701	4.06	6.36	4.00 ± 0.37	< 1	2.10 ± 0.79	8.04 ± 0.94	3.00 ± 0.23	1.07 ± 0.13	8.79 ± 2.98
3651030901	4.07	6.60	4.20 ± 0.23	1.28 ± 0.12	1.08 ± 0.16	12.16 ± 2.32	3.60 ± 0.58	0.85 ± 0.19	5.50 ± 3.86
3651031001	4.08	5.99	4.38 ± 0.44	1.15 ± 0.13	3.34 ± 1.20	11.92 ± 2.35	2.16 ± 0.34	1.87 ± 0.66	6.06 ± 5.21
3651031101	4.08	6.96	4.19 ± 0.17	1.16 ± 0.07	1.25 ± 0.15	9.20 ± 1.40	4.27 ± 0.41	0.69 ± 0.08	6.51 ± 2.57
3651031301	4.09	6.64	3.60 ± 0.27	1.03 ± 0.10	2.24 ± 0.64	6.57 ± 0.81	3.07 ± 0.22	0.97 ± 0.10	10.82 ± 3.08
3651031401	4.09	8.49	3.87 ± 0.12	1.19 ± 0.06	1.23 ± 0.11	9.32 ± 0.99	5.73 ± 0.40	0.68 ± 0.04	6.39 ± 2.54
3651031501	4.09	7.04	3.51 ± 0.18	1.09 ± 0.08	1.11 ± 0.16	9.16 ± 1.53	3.66 ± 0.47	0.85 ± 0.14	9.47 ± 4.28
3651031601	4.10	7.21	3.01 ± 0.60	1.00 ± 0.36	0.43 ± 0.19	3.74 ± 0.64	6.00 ± 1.83	0.50 ± 0.05	8.44 ± 5.78
3651032001	4.11	4.20	3.00 ± 1.86	1.45 ± 0.50	2.33 ± 3.23	5.12 ± 1.37	2.14 ± 0.30	0.91 ± 0.25	8.01 ± 6.29
3651032201	4.12	4.72	3.74 ± 0.16	1.15 ± 0.07	1.22 ± 0.14	10.02 ± 2.39	3.00 ± 0.51	0.59 ± 0.16	11.31 ± 3.18

Table 7 continued on next page

**Table 7** (*continued*)

OBSID	Phase	Flux	NH <sub>3</sub>	kT <sub>4</sub>	EM <sub>4</sub>	NH <sub>5</sub>	kT <sub>6</sub>	EM <sub>6</sub>	Flux <sub>FeK</sub>
		$10^{-11}$ ergs cm <sup>-2</sup> s <sup>-1</sup>	$10^{22}$ cm <sup>-2</sup>	keV	$10^{58}$ cm <sup>-3</sup>	$10^{22}$ cm <sup>-2</sup>	keV	$10^{58}$ cm <sup>-3</sup>	$10^{-5}$ photons cm <sup>-2</sup> s <sup>-1</sup>
3651032301	4.12	5.18	$3.70 \pm 0.18$	$1.17 \pm 0.09$	$1.29 \pm 0.16$	$12.28 \pm 3.30$	$3.73 \pm 0.90$	$0.54 \pm 0.16$	
3651032401	4.12	6.48	$3.49 \pm 0.14$	$1.11 \pm 0.06$	$1.25 \pm 0.14$	$8.44 \pm 1.52$	$5.13 \pm 0.63$	$0.51 \pm 0.06$	$3.39 \pm 2.74$
3651032801	4.14	5.91	$3.53 \pm 0.10$	$1.10 \pm 0.05$	$1.18 \pm 0.09$	$9.65 \pm 1.31$	$5.96 \pm 0.66$	$0.43 \pm 0.03$	$8.67 \pm 2.53$